ROBUST HYSTERESIS COMPENSATION FOR NANOPOSITIONING
CONTROL

By

Yasir Khudhair Al-Nadawi

A DISSERTATION

Submitted to
Michigan State University
in partial fulfillment of the requirements
for the degree of

Electrical Engineering - Doctor of Philosophy

2021

ABSTRACT

ROBUST HYSTERESIS COMPENSATION FOR NANOPOSITIONING CONTROL

By

Yasir Khudhair Al-Nadawi

Piezoelectric and other smart material-based actuators are widely used in micro- and nano positioning applications. However, the intrinsic hysteretic behavior of these actuators deteriorates their tracking performance. This dissertation, composed of three parts, is focused on nonlinear control methods for compensating the hysteresis and achieving high-precision control in the presence of model uncertainties. An inversion-based adaptive conditional servocompensator (ACS) is first proposed, where a nanopositioning system represented as a linear system preceded with a hysteresis nonlinearity modeled with a Modified Prandtl-Ishlinskii (MPI) operator. With an approximate inverse MPI operator as a compensator, the resulting system takes a semi-affine form. The proposed controller consists of two parts, a continuously-implemented sliding mode control (SMC) law followed by an ASC. The hysteresis inversion error is treated as a matched disturbance and its analytical bound is used to minimize the conservativeness of the SMC design. Under mild assumptions, the well-posedness and periodic stability of the closed-loop system are established.

The second part of the dissertation focuses on designing an inversion-free ACS to achieve precise tracking control of systems with hysteresis, without requiring explicit inversion of the hysteresis. To facilitate the control design, the MPI operator is rearranged into a form comprised of three parts: a linear term, a nominal hysteretic term represented by a classical Prandtl-Ishlinskii (PI) operator, and a hysteretic perturbation. The bound on the hysteretic perturbation is further derived based on the parameter uncertainty of the MPI operator. To properly "cancel" the nominal

hysteresis effect without inversion, a technique involving a low-pass filter is introduced. It is shown that, with persistent excitation, the closed-loop variables are ultimately bounded and the tracking error approaches a neighborhood of zero, where the neighborhood can be made arbitrarily small via the choice of the SMC boundary layer width parameter and the servocompensator order.

In the third part, an output feedback-based hysteresis compensation approach is used using dynamic inversion and extended high-gain observers. With mild assumptions on the properties of the hysteresis nonlinearity, the system can be represented as an uncertain, non-affine, nonlinear system containing a hysteretic perturbation. Dynamic inversion is used to deal with the non-affine input, uncertainties, and the hysteretic perturbation, where the latter two are estimated using an extended high-gain observer. Analysis of the closed-loop system under output feedback shows that the tracking error converges to a small neighborhood near the origin, which can be made arbitrarily small via proper choice of time-scale parameters of dynamic inversion and the observer, respectively.

The efficacy of the three proposed controllers is verified experimentally on a commercial nanopositioning device under different types of periodic reference inputs, via comparison with multiple inversion-based and inversion-free approaches.

To all my beloved family
My parents, my wife, and my brothers
for their endless love, sacrifices,
prayers, support, and encouragement.

ACKNOWLEDGMENTS

In the name of Allah, the most merciful and the most beneficent. All praise and thanks are due to Allah the Almighty for providing me with the opportunity to undertake and complete this task. I would like to acknowledge the invaluable help and guidance of my academic advisors, Prof. Hassan K. Khalil and Prof. Xiaobo Tan. I am extremely fortunate to have had the opportunity to work so closely with them over the past several years with such preeminent scholars as Prof. Khalil and Prof. Tan. Their wisdom and vast, seemingly boundless knowledge of our field was the most precious and useful resources of all. They often exhibited great patience with me through my learning process. For their unwavering support and encouragement, I shall be everlastingly grateful. I would also like to thank my other committee members, Prof. Guoming Zhu and Assist. Prof. Vaibhav Srivastava for their support and tremendously helpful feedback during my research activities. I am so grateful to my colleagues and friends, particularly Dhrubajit Chowdhury, for collaborating with me in one of the research projects of this dissertation and for all the valuable discussions we had through our work together. Also, I would like to thank the National Science Foundation (CMMI 1301243) for supporting my research.

I would not be at this momentous juncture of my life if not for my parents, Khudhair and Thamera, to whom I owe everything. They both unfailingly led by example when it came to teaching and encouraging me to always think for myself and others. They have always been there for me to support and encourage me no matter how hard the situation is. With all they gave to me, I will always be indebted to them for the rest of my life. And to my wife, Nawar, who since I met her have provided me a boundless love, constant support, and encouragement that have made all this possible. Finally, I am very thankful to my brothers; Ayad, Samer, Zeyad, and Ashraph for their constant encouragement, love, and advices. I will be always grateful to them.

TABLE OF CONTENTS

LIST OF TABLES

LIST OF FIGURES

xi

Chapter 1

Introduction and Literature Survey

1.1 Introduction

Smart material-based actuators such as piezoelectric or magnetostrictive actuators are significant in high-precision applications due to their ability to achieve manipulation in micro/nano meter level with relatively fast responses, their compact size, and large bandwidth of operation [1,2]. One important area where smart material-actuators are used is nanopositioning, which is of importance to applications such as atomic force microscopy, scanning probe microscopy (SPM) [3,4], ultra-high density data storage, micro/nanofabrication [5], micro-manipulators [6,7], ultra-precision grinding operation [8], mechanical nanomanufacturing system for nanomilling [9], high-precision electro-chemical etching-based micromachining [10], nanofabrication of materials [11], and investigation of biological systems over scales ranging from single-molecules to whole cells [12,13].

However, these types of actuators exhibit a severe phenomenon called hysteresis. Generally, a system is said to exhibit hysteresis when a characteristic looping behavior of the input-output graph is displayed. The relationship between the input and output cannot be represented in terms of a single-valued function [14]. The presence of this non-smooth input nonlinearity causes deterioration in system performance and oscillations, poor tracking responses [2], or even instability [15]. Therefore, the necessity to compensate the hysteretic behavior of these actuators by feedback controllers has became indispensable. There has been significant research interest for hysteresis mod-

eling and control design techniques to mitigate its effect [16].

1.2 Literature Survey

1.2.1 Hysteresis Modeling

Hysteresis models can be mainly classified into physics-based and phenomenology-based models. The physics-based models are system-dependent and focus on first principles of physics, while the phenomenology-based models mainly replicate the natural behavior of the system without giving insight into the physics of the system. Since they are not specific to a physical system, these models are generally applicable for a large class of hysteretic systems, examples of these mathematical models, also widely known as hysteresis operators. There are many models developed and studied in literature; for example: Bouc-Wen model [17], the Duhem model [18,19], the Maxwell-Based model [20], the Jiles-Atherton model [21], the Krasnosel'skii-Pokrovskii model [22,23], the Preisach model [24,25], and the Prandtl-Ishlinskii (PI) model [26,27]. The later two approaches are widely investigated in the literature, however; one disadvantage of the Preisach operator as compared to the Prandtl-Ishliskii model is that it does not admit an analytical inverse model, which poses a challenge in real-time implementation [28]. This makes the Prandtl-Ishlinskii operator more applicable in real-time control systems due to its analytic inversion feature [29].

1.2.2 Inversion-based Control

One control methodology for systems with (input) hysteresis is to use a feedforward open-loop scheme by placing an inverse compensator at the input side to mitigate the effect of the hysteresis [1, 20, 30]. Examples of published work under this approach; the work of [31–36]. One draw-

back of this approach is that it depends strongly on how accurate the hysteresis model is. Despite the reasonable tracking performance achieved using the feedforward control methodology, it has been shown that it is necessary to ensure system robustness against model uncertainties and external disturbances [37]. Moreover, operators like the Preisach operator, does not admit an analytical form of its inverse and therefore it needs to be constructed through computation-intensive techniques [25]. For operators, like the finite-dimensional classical [31], modified [38], and generalized [39] PI operators, where analytical formulas for their inverses exist, the number of hysterons needs to be sufficiently high in order to have good model accuracy, which entails more storage space and computational effort. In addition, due to the multi-valued and non-smoothness feature of hysteresis, these models show strong sensitivity of the model parameters to unknown measurement errors in the model identification [40]. Therefore, the robustness of the system against the inversion error perturbations, any external disturbance, or noise inputs can not be guaranteed.

Consequently, a more effective approach is to integrate the inverse compensator within a closed-loop system, with the latter designed to handle the residual tracking error by considering bounded disturbances resulted from the hysteresis inversion error and other perturbations. Examples of work done along this line using a popular choice of feedback controller is the PID control; see for the work explored in [1, 41, 42]. Although these types of classical controllers fail to track at high-frequency references [43]. Adaptive control can be used to deal with the inversion error which mainly arises due to uncertainty in the hysteresis parameters. Examples of adaptive control designed to adapt the hysteresis inverse operators' parameters [15, 44–47].

More advanced techniques like sliding-mode control are robust against disturbances and parameter uncertainties [48–50] have been used. An $\mathcal{H}_\infty$ robust control method was proposed by Al Janaideh et al. in [51], where the controller was designed based on the characterization of the output of the inverse PI operator, which consists of a linear reversible term and a bounded nonlinear

3

term.

Internal model-based regulators present a promising approach. The internal model is designed to model sinusoidal disturbances inputs, where the role of the internal model is to act as an external generator that rejects these sinusoidal matched disturbances [52]. Example of this approach is the work of [5], where the knowledge of the internal model frequencies was assumed in the internal model design. An important problem is that in most cases, one does not have knowledge of the frequencies of the exogenous signals generated by the exosystem. Therefore, adaptation of the internal model for estimating those frequencies becomes a necessity to compensate these exosystem uncertainties. This limitation motivates the work of Serrani et al. [53], where an adaptation mechanism was proposed to estimate a finite number of frequencies. This approach was adopted by Esbrook et al. [54] for the control of piezo-driven actuators. In their work, the hysteresis was modeled by using the classical PI operator, which was compensated with a feedforward inverse operator. The inversion error was treated as a periodic matched disturbance, and a servomechanism was designed to accommodate a finite number of frequencies, which were estimated through a direct adaptation approach. Despite the initial success reported in their paper, further experiments conducted later showed that the adapted parameters failed to converge, which motivated the authors to replace the direct adaptation servomechanism with an indirect adaptation scheme [55].

Many other methodologies have been investigated with the inversion-based framework in the literature, including, for example, iterative control [56, 57], model reference adaptive inverse control [45], and hysteretic perturbation estimation [58–61]. However, the achieved tracking precision will depend mainly on the smallness of the hysteresis inversion error, which is highly dependent on the accuracy of the hysteresis model and its identified parameters.

1.2.3 Inversion-free Control

The high computational effort required to implement the inverse hysteresis models and the inversion error resulted due to the mismatch between the hysteresis model and the actual hysteresis motivates the development of the inversion-free approaches. In this class of control methods, either the inversion is achieved implicitly rather than explicitly or the controller does not involve any inversion at all.

In [40] an inversion-free adaptive control design is proposed based on the assumption that the hysteresis nonlinearity is modeled as a Prandtl-Ishlinskii operator. The hysteretic input term is expressed as a combination of a control linear-term and a hysteretic perturbation term assumed to be bounded by a known constant. The hysteretic disturbance term is compensated by an adaptation law that estimates the density function, which is treated as a parameter in this framework. A model reference-based adaptive control approach is developed in [62] for a system that includes hysteresis nonlinearity described as a Prandtl-Ishlinskii operator. In their work, the inversion of the hysteresis operator is implemented implicitly to avoid certain difficulties in theoretical analysis.

In [63] a retrospective cost adaptive control (RCAC) is designed in discrete time for the tracking control of a shape memory alloy (SMA) actuator. The SMA actuator is assumed to be modeled by a Wiener model that has linear dynamics cascaded with a hysteresis nonlinearity modeled as a generalized Prandtl-Ishlinskii operator. Their adaptation law ensures the compensation of the hysteretic disturbance without the need to use an inverse operator. The work of [64] presents an inversion-free state-feedback controller design for a minimum-phase system proceeded by a Prandtl-Ishlinskii operator. A general controller structure with an integral term is assumed in this work. The major contribution of this work is that the boundedness of the signals of the closed-loop system is guaranteed if a specific linear matrix inequality (LMI) condition is satisfied.

A feedforward inversion-free hysteresis compensator was proposed in discrete time in [29] based on the rate-dependent Prandtle-Ishlinskii (RDPI) hysteresis model without the need to construct a rate dependent inverse PI operator. The compensator utilizes an arrangement of the (RDPI) model into a linear reversible term and a rate-dependent hysteretic perturbation. A major assumption about this work is the availability of a good (RDPI) hysteresis model, due to its open-loop nature. This work was extended in [37], in which the feedforward scheme is being integrated within a feedback control system framework that is designed based on the internal model control (IMC) theory. The proposed controller was implemented on a piezoelectric micropositioner to test the validity of the controller.

Another alternative approach towards inversion-free hysteresis compensation for linear systems is by using disturbance observers; see [65–67]. This approach mainly relies on the decomposition of the hysteresis operator into a linear part, where the control input appears linearly, and another part treated as a hysteretic perturbation (disturbance). Disturbance observer-based control methods involve estimating this hysteretic perturbation and canceling it by using its estimate in the feedback control law.

1.3 Overview of Contributions

In this dissertation, three approaches for hysteresis compensation are presented, which are the inversion-based adaptive conditional servocompensator, the inversion-free adaptive conditional servocompensator, and the dynamics inversion based on extended high-gain observer approach. The following subsections provide a detailed breakdown for each approach.

1.3.1   Inversion-based ACS Approach

In chapter 2, we focus on the design of an adaptive conditional servocompensator for precise tracking control of a class of systems with hysteresis. The hysteresis is assumed to be modeled by an MPI hysteresis operator [38], which outperforms the classical PI operator with its ability to incorporate asymmetric hysteretic behavior. The chapter has the following major contributions:

1. The hysteresis inversion error is analyzed and an analytical bound on the inversion error is derived and used in the sliding mode controller design,which results in less conservative results as compared to the case when a constant bound is used. The controller based on a constant bound results in larger and more aggressive control actions with larger tracking errors.

2. An output feedback controller is designed using adaptive conditional servocompensator by assuming that the residual disturbance due to imperfect hysteresis inversion is composed of a finite number of unknown frequencies. The unmeasured states are estimated by a high-gain observer.

3. Periodic stability analysis is conducted using contraction mapping arguments by following the stability analysis framework introduced in [68]. This approach is useful in establishing the periodic stability in a less conservative manner as compared to Lyapunov-based stability arguments under the smallness of the hysteretic inversion perturbation. However, the main challenge is that our proposed closed-loop control system does not fit exactly the system assumed in [68] due to the inclusion of non-smooth terms in our control law. We are able to establish, under mild assumptions, that the closed-loop system solution will converge exponentially to a unique periodic solution when the inversion error is sufficiently small without complicating the control law with additional terms that might be computationally heavy.

The proposed control approach is experimentally evaluated on a commercial piezoelectric nanopositioner. It shows superior precision tracking performance as compared to for other control approaches implemented on the same apparatus. The four control approaches considered for comparison are sliding mode control [48], Single Harmonic Servo-Compensator (SHSC) and Multi-Harmonic Servo-Compensator (MHSC) [5], the dynamic inversion based on extended high-gain observer [69], and a classical PI controller without hysteresis inversion.

1.3.2 Inversion-free ACS Approach

In chapter 3, an adaptive conditional servocompensator is designed without requiring the use of an analytical inverse hysteresis operator in the loop. The hysteresis nonlinearity is assumed to be modeled with Modified Prandtl-Ishlinskii (MPI) operator. The following contributions are intended;

1. A reconstruction of the (MPI) hysteresis operator that transforms the input hysteric term into a linear part in terms of the control input, a hysteretic term modeled with a classical (PI) operator parameterized with the nominal weights, and a hysteretic perturbation term. This arrangement converts the system from a non-affine form into a semi-affine one. This result is basically established in Preposition 3.1 based on an assumption of an additive form of parametric uncertainty for the hysteresis weights. In Proposition 3.2, it was shown that the hysteretic bound obeys a linear growth bound that is not all of its terms are necessarily small. This bound will be utilized in designing a less-conservative continuously-implemented sliding-mode control law.

2. One difficulty arose in the design of the equivalent portion of sliding-mode control law due to the dependence of the nominal PI operator term on the control input. This required the

solution of a very complicated nonlinear equation that has a PI operator in one of its terms in terms of the equivalent control input. The complexity lies in both the theoretical analysis and implementation, where this issue creates a logical-loop due to the dependence of the instantaneous value of the control input on that particular nominal hysteric term. To solve this issue, a low-pass filter is inserted in the loop to avoid certain complexities and to simplify the realization of the controller without the need to solve the above mentioned complicated equation.

3. The adaptive conditional servocompensator is then designed based on an assumed number of frequencies to compensate the residual hysteretic disturbances in the boundary-layer phase. One challenge on the analysis side is that the original approach of the adaptive conditional servocompensator [70] does not accommodate hysteretic perturbations. Moreover, the theoretical frame work to prove stability of [68] cannot be used here, because the a major assumption of smallness of the hysteretic perturbation term is not satisfied in this case. Therefore, the stability analysis is established by extending the theoretical frame-work in [70] to handle the hysteretic perturbation. These results are embodied in Theorem 3.1 and 3.2, where in Theorem 3.1, we show that in the reaching phase, all the closed-loop system variables are bounded and will converge to a positively-invariant set that is parameterized by certain parameters related to the filter time-constant, the boundary-layer width, and a high-gain observer parameter. Theorem 3.2 establishes the ultimate boundedness of the closed-loop system in boundary-layer stage under the hysteretic-perturbation-free case and when there exist valid perturbations.

We validate our control design with experimental implementation on a commercially available piezo-actuated nanopositioner. The obtained results show a significant reduction of the tracking

error for all the tested references as compared to the results of three other approaches implemented on the same experimental apparatus. The first is a classical proportional-integral controller applied directly without inversion in the loop. The second approach is the sliding mode control approach [48], and the third approach is the servocompensator approach [5].

1.3.3 Dynamic Inversion Based on Extended High-gain Observer Approach

In chapter 4, we consider the tracking problem for an uncertain nonlinear single-input-single-output system, preceded by an unknown hysteresis operator. The following points summarize the contributions:

1. With a mild assumptions on the general properties of the hysteresis, we apply dynamic-inversion [71], to effectively compute the hysteresis inverse without requiring an explicit model of the hysteresis. In order to implement the dynamic inversion algorithm, an extended high-gain observer [72] is used to estimate the hysteretic part, system states, and uncertainties at a time scale faster than the plant dynamics and the dynamic inversion. While an extended high-gain observer has been used with dynamic inversion in [73] for memory-less non-affine nonlinearities, the proposed approach is the first attempt to deal with a nonaffine hysteretic nonlinearity using dynamic inversion and an extended high-gain observer. For the resulting three-time-scale closed-loop system, we show that the tracking error converges to a small neighborhood near the origin, which can be made arbitrarily small via proper choice of time-scale parameters of dynamic inversion and the observer, respectively.

2. The non-affine hysteretic nonlinearity poses a theoretical challenge in the analysis. Therefore, we have developed two propositions in the chapter (Propositions 4.1 and 4.2), which prove certain properties of the hysteresis operator that are then used for the analysis of the

closed-loop system later in the chapter. The proposed algorithm presents several advantages over other inversion-free approaches in literature. Firstly, the non-hysteretic component is assumed to be general with mild assumptions, unlike the other inversion-free approaches [65, 74], which assume that the non-hysteretic component to be linear. Secondly, the plant is considered to be nonlinear satisfying the minimum-phase assumption. Thirdly, the complexity of the proposed controller is invariant with respect to the complexity of the underlying hysteresis operator. This is in contrast to adaptive hysteresis inversion-based [15] or pseudo inversion-based approaches [75], where the controller complexity is correlated directly with the number of hysteretic elements in the model. The extended high-gain observer is used to estimate the hysteretic perturbation and then cancel it. Compared to [76], we have two major differences: i) we consider an uncertain nonlinear single-input-single-output system with nonaffine hysteretic nonlinearity, which is more general; ii) we consider rate-independent hysteresis effect which can be modeled by standard operators like the PI and Preisach operators.

We compare the proposed method with the sliding mode controller (SMC) [48], single harmonic servocompensator (SHSC) [5] and the multiple harmonic servocompensator (MSHC) [5], all of which use an explicit hysteresis inversion operator. Selecting these robust control techniques for comparison is mainly because of the following reasons: (i) The aforementioned approaches are comparable to our approach in the sense that they are robust control algorithms. (ii) All these approaches are implemented with an inverse operator inserted at the input side. Therefore, obtaining comparable or better results shows the efficacy of the proposed controller, which is simpler in structure as compared to the compared approaches. (iii) The compared approaches were implemented on the same apparatus under comparable experimental conditions, which makes the comparison fair when evaluating the methods. The experiments on a nanopositioner confirm the

11

effectiveness of the proposed control scheme and demonstrate comparable tracking performance with the aforementioned algorithms. In particular, we have demonstrated tracking of a 100-Hz sinusoidal reference signal with 0.2051 % mean error and 0.6666 % max error for a travel range of 40 μm, compared with 0.83 % mean and 2.75 % peak errors, respectively, for SMC.

I would like to mention that the work in chapter 4, is the result of the collaboration with my colleague Dhrubajit Chowdhury and Prof. Xiaobo Tan. Chowdhury's main contribution is in preparing the theoretical part (in particular the Propositions 4.1 and 4.2), designing the controller, and the stability analysis (Theorem 4.1 and Theorem 4.2) with my support throughout the steps of the work. I took the lead in the simulation part and in the experimental implementation of the controller with Chowdhury's help in the controller tuning process.

Chapter 2

Inversion-based Hysteresis Compensation Using Adaptive Conditional Servocompensator

2.1 Introduction

In this chapter, we consider the problem of tracking periodic reference inputs for a class of nonlinear systems comprised of linear dynamics preceded by a hysteresis operator. Following [70], we design an adaptive conditional servocompensator for tracking a periodic reference. An MPI operator [38] is used to capture the hysteresis nonlinearity with enhanced performance over the classical PI operator. The main difference between this approach and the classical internal model work in [53], is that the internal model adaptation is active only inside a small neighborhood of a certain manifold. The controller design is done through a three-step process. First, we design a continuously-implemented sliding mode controller, where both the hysteresis and the system dynamics are assumed to be uncertain. We derive the upper bound of the hysteresis inversion error and make use of this bound to design the sliding mode control to mitigate the conservativeness of the SMC design. In the second step, we design a conditional servocompensator with adaptive tuning of its coefficients. Finally, a high-gain observer is introduced for estimating the unavailable

states.

Stability analysis is conducted for the closed-loop system to demonstrate semi-global error regulation. First, the well-posedness of the closed-loop system in the presence of small hysteresis inversion error is established using the contraction mapping principle. We then show that under the inherited exponential stability properties from the hysteresis-free closed-loop system, the stability of the closed-loop system with hysteretic perturbations can be established. In particular, we show that, under proper conditions, the tracking error converges exponentially to a periodic solution in the neighborhood of the origin. The proposed controller design is experimentally validated on a commercial nanopositioner, where a series of experiments are conducted by applying sinusoidal reference inputs.

The remaining sections are organized as follows. In Section 2.2, the problem formulation, the system model with hysteresis, and the derivation of the analytical bound of the inversion error are presented. Section 2.3 explains the adaptive conditional compensator design. In Section 2.4, the periodic stability analysis for the closed-loop system with hysteresis perturbation is discussed. Finally, experimental results are given in Section 2.5.

2.2 Problem Formulation

2.2.1 System Model with Hystersis Nonlinearity

Consider the following non-affine system (depicted in Fig. 2.1) modeled with linear dynamics preceded by hysteresis input nonlinearity,

$$
\begin{aligned}
\dot{x}(t) &= F_p(x(t)) + B_p u_o(t) \\
y(t) &= x_1(t),
\end{aligned}
\tag{2.1}
$$

14

where $x \in \mathcal{R}^n$ is the state vector, y is the measured output, and $u_o \in \mathcal{R}$ is the output of the hysteresis operator,

$$u_o(t) = F_h[u_{in}(\cdot); v_o](t) \tag{2.2}$$

where F_h denotes the hysteresis operator, $u_{in} \in \mathcal{R}$ is the system input, and v_o represents the initial memory of the hysteresis (we will elaborate more on the hysteresis model in the next section). The function F_p and the vector B_p are defined as follows:

$$F_p = \begin{bmatrix} x_2 \\ x_3 \\ \vdots \\ x_n \\ f_n(x) \end{bmatrix}_{n \times 1}, \quad B_p = \begin{bmatrix} 0 \\ 0 \\ \vdots \\ \vdots \\ b \end{bmatrix}_{n \times 1} \tag{2.3}$$

where $f_n(x) = -a_1 x_1 - a_2 x_2 - \cdots - a_n x_n$, a_i's and $b > 0$ are the system parameters. The objective is to make the system output $y(t)$ track a desired reference input $y_d(t)$, which is assumed to obey the following assumption.

Assumption 2.1. *The desired reference y_d and its time-derivatives up to order n are piecewise continuous in t, bounded for all $t \geq 0$, and T-periodic (i.e., $y_d(t) = y_d(t+T)$) for some $T \geq 0$.*

The tracking error is defined as

$$e_1(t) = y(t) - y_d(t)$$

Using the above equation, we can obtain the error dynamics as follows:

$$\dot{e}(t) = F_p(e(t)) + B_p u_o(t) + B_d \delta_d(t), \tag{2.4}$$

15

where F_p is defined as in (2.3) with argument e instead of x, $e = [e_1, e_2, \cdots, e_n]^T$, $e_i = \frac{d^{i-1}e}{dt^{i-1}}$ for $i = 2, \cdots, n$, $(\cdot)^T$ denotes the transpose, $B_d = [0, \cdots, 0, 1]^T$, and δ_d is defined as:

$$\delta_d(t) = -a_1 y_d - a_2 \dot{y}_d - \cdots - a_{n-1} y_d^{n-1} - a_n y_d^n$$
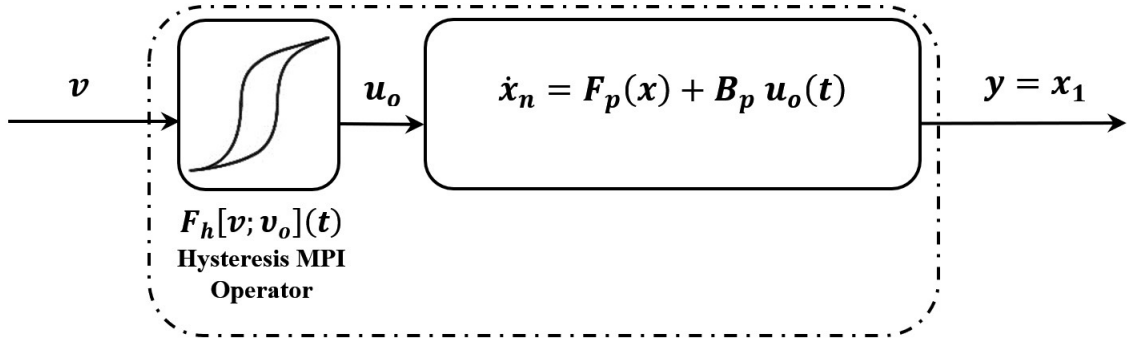
Figure 2.1: Schematic of the class of systems considered, with linear dynamics proceeded by a hysteresis operator.

2.2.2 MPI Hysteresis Operator

To model the hysteresis operator F_h in Eq. (2.2), we use the Modified Prandtl-Ishlinskii (MPI) operator (illustrated in Fig. 2.2 below). This model was originally proposed by Kuhnen [38] in 2003 by combining the classical Prandtl-Ishlinskii (PI) hysteresis operator with another operator, which is represented by a weighted superposition of one-sided deadzone nonlinearities. This modification makes the MPI operator capable of modeling asymmetric hysteretic characteristics as compared to the classical PI operator. The PI operator is a weighted superposition of basic hysteresis units, each of which is modeled with a backlash operator with a threshold r_{th}. The backlash operator for a continuous and monotone input $v(t)$ for $t \in [0, T]$ is given as:

$$u_{bk}(t) = \max\{\min\{v(t) + r_{th}, u_{bk}(0)\}, u_{in}(t) - r_{th}\} \tag{2.5}$$

where $u_{bk}(0)$ is the initial state. In essence, the PI operator consists of weighted integral of a continuum of backlash operators, which makes it an infinite-dimensional operator [22]. Due to practical consideration, a finite-dimensional PI operator is often considered, which is represented by a weighted sum of a finite number of backlash operators. Accordingly, the following assumption is made for the MPI operator.

Assumption 2.2. *The hysteresis nonlinearity F_h is modeled with a finite-dimensional MPI operator, which consists of $(q+1)$ backlash operators and $(2l+1)$ one-sided deadzone operators, where q and $l \in \mathcal{N}^+$.*
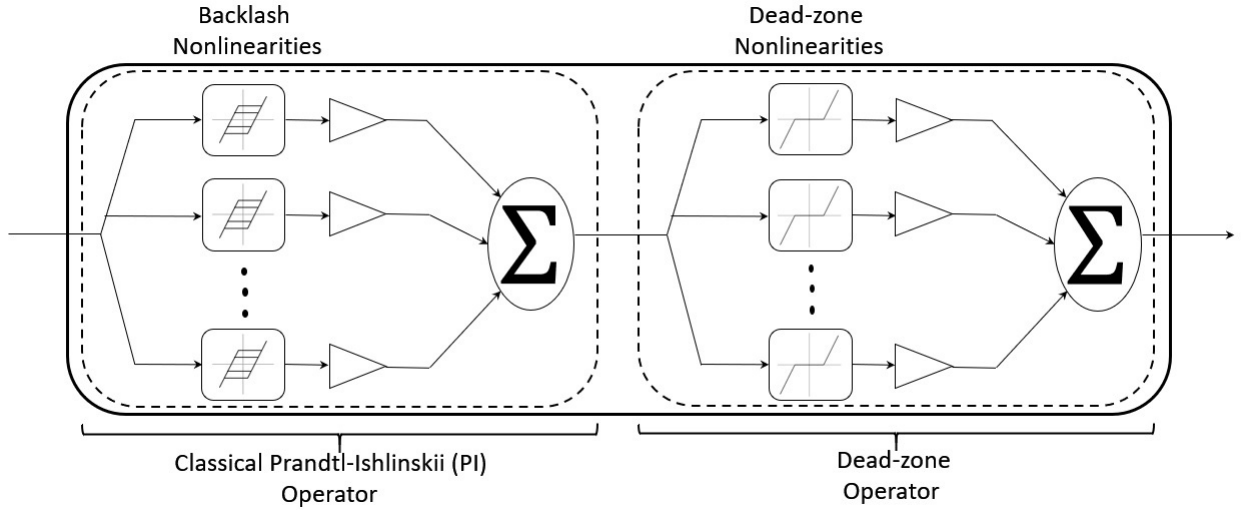
Figure 2.2: Block diagram of the finite-dimensional MPI hysteresis operator. Triangular blocks represent the weight gains of the PI and the dead-zone operators, respectively.

Based on Assumption 2.2, the output u_b of the PI operator F_b under the input v is given by

$$u_b(t) = F_b[v; x_b(0)](t) = \sum_{i=0}^{q} \theta_{bi} x_{bi}(t) \tag{2.6}$$

where $x_{bi}(t)$ represents the output of the ith backlash operator such that

$$x_{bi}(t) = \mathcal{P}_{bi}[v; x_{bi}(0)](t) \tag{2.7}$$

17

in which $x_{bi}(0)$ is the initial state, and $\theta_{bi} \geq 0$, is the weight of the ith backlash operator. Let $\theta_b = [\theta_{b0}, \theta_{b1}, \cdots, \theta_{bq}]$ be the weight vector and $r = [r_0, r_1, \cdots, r_q]$ be the backlash radii vector, where $r_0 = 0$ and $r_i \geq 0$ for $i = 1, 2, \cdots, q$. Define the following vectors:

$$\mathcal{P}_b := [\mathcal{P}_{b0}, \mathcal{P}_{b1}, \cdots, \mathcal{P}_{bq}]^T \tag{2.8}$$

$$x_b := [x_{b0}, x_{b1}, \cdots, x_{bq}]^T \tag{2.9}$$

$$x_b(0) := [x_{b0}(0), x_{b1}(0), \cdots, x_{bq}(0)]^T \tag{2.10}$$

By using equations (2.8)-(2.10), we rewrite equation (2.6) in a compact form as follows:

$$u_b(t) = \theta_b^T x_b = \theta_b^T \mathcal{P}_b[v; x_b(0)]$$

As mentioned above, the deadzone operator contains a weighted superposition of one-sided deadzone functions. For each one-sided deadzone function $\mathcal{P}_{di}$ with input $u_b(t)$ and a threshold d_z, the output is given as

$$\mathcal{P}_{di}(u_b(t)) = \begin{cases} \max\{u_b(t) - d_z, 0\} & \text{if } d_i > 0 \\ u_b(t) & \text{if } d_i = 0 \\ \min\{u_b(t) - d_z, 0\} & \text{if } d_i < 0 \end{cases} \tag{2.11}$$

Let $d := [d_{-l}, \cdots, d_0, d_1, \cdots, d_l]^T$ and $\theta_d := [\theta_{d-l}, \cdots, \theta_{d0}, \theta_{d1}, \cdots, \theta_{dl}]^T$ be the deadzone operator thresholds and weights vectors, respectively. Define the deadzone operator vector $\mathcal{P}_d := [\mathcal{P}_{d-l}, \cdots, \mathcal{P}_{d0}, \mathcal{P}_{d1}, \cdots, \mathcal{P}_{dl}]^T$. The output $u_o(t)$ of the MPI operator F_h under the input $v(t)$ with

18

an initial condition state $x_b(0)$ will be

$$u_o(t) = F_h[v; x_b(0)](t) := \sum_{i=l}^{l} \theta_{di} \mathcal{P}_{di} \left(\sum_{j=0}^{q} \theta_{bj} \mathcal{P}_{bj}[v; x_b(0)](t) \right)$$

$$= \theta_d^T \mathcal{P}_d \left(\theta_b^T x_b(t) \right)$$

(2.12)

Let $\mathbb{W}_t^{1,1}$ be the Banach space of the absolutely continuous function $u : [0,t] \to \mathcal{R}$ equipped with a standard norm $\| \cdot \|_{\mathbb{W}_t^{1,1}}$, which is a combination of the 1-norm of the function u and the 1-norm of the first order time-derivative of u such that;

$$\|u\|_{\mathbb{W}_t^{1,1}} = \|u\|_1 + \int_0^t \|u'(\tau)\|_1 d\tau$$

(2.13)

where $u'(\tau))$ is the derivative of u with respect to τ. In Proposition 2.1 below, we establish the local Lipschitz property for the MPI operator F_h for any input $u \in \mathbb{W}_L^{1,1} \subset \mathbb{W}_t^{1,1}$ where

$$\mathbb{W}_L^{1,1} = \{u | u : \mathcal{R}_+ \to \mathcal{R}, u|_{[0,t]} \in \mathbb{W}_t^{1,1}, \forall t \geq 0\}$$

(2.14)

Proposition 2.1. *The MPI operator F_h in equation (2.12) is locally Lipschitz continuous with constant $L_h = \sum_{-l}^{l} |\theta_{di}| \sum_{j=0}^{q} |\theta_{bj}|$ with the following condition:*

$$\sup_{\tau \in \mathcal{R}_+} \|F_h[u_1; x_b(0)](\tau) - F_h[u_2; x_b(0)](\tau)\|_{\mathbb{W}_\tau^{1,1}} \leq L_h \sup_{\tau \in \mathcal{R}_+} \|u_1(\tau) - u_2(\tau)\|_{\mathbb{W}_\tau^{1,1}}$$

(2.15)

where u_1, u_2 are two different inputs in the set $\mathbb{W}_L^{1,1}$.

Proof. Consider the PI operator F_b in Eq. (2.6), under inputs u_1, u_2, and the initial condition $x_b(0)$. By utilizing the Lipschitz continuity property of the PI operator F_b inside $\mathbb{W}_L^{1,1}$ [45, 77], one can

19

derive the following inequality:

$$\sup_{\tau \in \mathcal{R}_+} \| F_b[u_1; x_b(0)](\tau) - F_b[u_2; x_b(0)](\tau) \|_{\mathbb{W}_\tau^{1,1}} \le \sum_{i=0}^{q} |\theta_{b_i}| \sup_{\tau \in \mathcal{R}_+} \| u_1(\tau) - u_2(\tau) \|_{\mathbb{W}_\tau^{1,1}} \quad (2.16)$$

Similarly, utilizing the the Lipschitz continuity property of the dead-zone operator P_d (2.11), we can show

$$\sup_{\tau \in \mathcal{R}_+} \| F_h(F_b[u_1; x_b(0)](\tau)) - F_h(F_b[u_2; x_b(0)](\tau)) \|_{\mathbb{W}_\tau^{1,1}}$$

$$\le \sum_{i=-l}^{l} |\theta_{di}| \sup_{\tau \in \mathcal{R}_+} \| F_b[u_1; x_b(0)](\tau) - F_b[u_2; x_b(0)](\tau) \|_{\mathbb{W}_\tau^{1,1}} \quad (2.17)$$

By combining the two inequalities (2.16) and (2.17), we get (2.15). □

2.2.3   Inversion of the MPI Operator
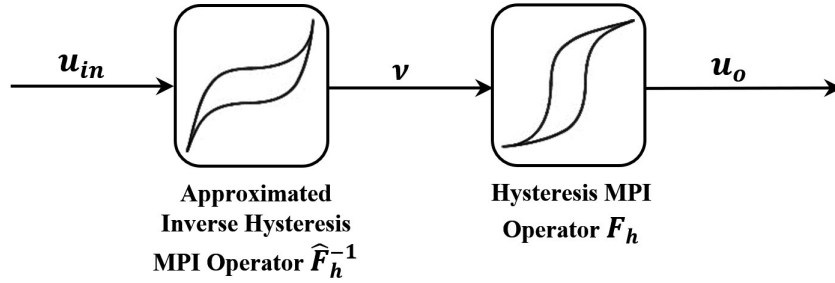
Figure 2.3: The feedforward hysteresis inversion.

As shown in Fig. 2.3, the hysteresis inversion is achieved by cascading an inverse MPI operator with the MPI hysteresis operator F_h. Let $\hat{F}_h$ denotes the approximated forward MPI operator resulted from the model identification.

Assumption 2.3. *For the MPI operator (2.12), only the values of the radii vector r and the thresholds vector d are known.*

20

The above assumption implies that exact values of both the PI operator's weight vector θ_b and the deadzone operator's weight vector θ_d are unknown. This assumption is common and it has been used frequently in the literature (for example see references [38], [78], and [79]).

Based on Assumption 2.3, let $\hat{\theta}_b$ and $\hat{\theta}_d$ be the estimated values of the weight vectors θ_b and θ_d, respectively. We denote the errors of these weight vectors as follows:

$$\Delta_b = \theta_b - \hat{\theta}_b,$$
$$\Delta_d = \theta_d - \hat{\theta}_d \tag{2.18}$$

where $\Delta_b \in \mathcal{R}^{q+1}$ and $\Delta_d \in \mathcal{R}^{2l+1}$ are the weight error vectors of the weight vectors θ_b and θ_d, respectively. Consider Fig. 2.3, and let F_h^{-1} denotes the inverse hysteresis operator and $v(t)$ represents the generated output of the operator F_h^{-1}. The inverse operator F_h^{-1} is also an MPI operator and it is defined as:

$$
\begin{aligned}
v(t) &= F_h^{-1}[u_{in}; \bar{x}_b(0)](t) \\
&:= \sum_{i=0}^{q} \bar{\theta}_{bi} \bar{\mathcal{P}}_{bi} \left[\sum_{j=l}^{l} \bar{\theta}_{dji} \bar{\mathcal{P}}_{dj}(u_{in}(t)); \bar{x}_{bi}(0) \right](t) \\
&= \bar{\theta}_b^T \bar{\mathcal{P}}_b \left[\bar{\theta}_d^T \bar{\mathcal{P}}_d(u_{in}(t)); \bar{x}_b(0) \right](t)
\end{aligned}
\tag{2.19}
$$

where $\bar{\mathcal{P}}_{bi}$ and $\bar{\mathcal{P}}_{di}$ are the individual inverse PI and deadzone operators, respectively, the vectors $\bar{\mathcal{P}}_b = [\bar{\mathcal{P}}_{b0}, \cdots, \bar{\mathcal{P}}_{bq}]^T$ and $\bar{\mathcal{P}}_d = [\bar{\mathcal{P}}_{d-l}, \cdots, \bar{\mathcal{P}}_{d-1}, \bar{\mathcal{P}}_{d0}, \cdots, \bar{\mathcal{P}}_{d1}, \cdots, \bar{\mathcal{P}}_{dl}]^T$ are the vector of the inverse PI and deadzone operator vectors, respectively. The vectors $\bar{x}_b = [\bar{x}_{b0}, \bar{x}_{b1}, \cdots, \bar{x}_{bq}]^T$ and $\bar{x}_b(0) = [\bar{x}_{b0}(0), \bar{x}_{b1}(0), \cdots, \bar{x}_{bq}(0)]^T$ are the inverse PI operator state and its initial state, respectively. The weights $\bar{\theta}_{bi}$ and $\bar{\theta}_{dj}$ are for the individual inverse backlash and deadzone operators, respectively, where $\bar{\theta}_b = [\bar{\theta}_{b0}, \bar{\theta}_{b1}, \cdots, \bar{\theta}_{bq}]^T$ and $\bar{\theta}_d = [\bar{\theta}_{d-l}, \cdots, \bar{\theta}_{d1}, \bar{\theta}_{d0}, \bar{\theta}_{d1}, \cdots, \bar{\theta}_{dl}]^T$. Let $\bar{r} = [\bar{r}_0, \bar{r}_1, \cdots, \bar{r}_q]^T$ and $\bar{d} = [\bar{d}_{-l}, \cdots, \bar{d}_{-1}, \bar{d}_0, \bar{d}_1, \cdots, \bar{d}_l]^T$ be the thresholds' vectors of the in-

21

verse PI and deadzone operators, respectively.

Remark 2.1. *Due to space limitation, the procedure of how to calculate the inverse MPI operators parameters' vectors $\bar{\theta}_b$, $\bar{\theta}_d$, $\bar{r}$, and $\bar{d}$ has been omitted. For more details about these calculations, the readers may consult the reference [38].*

In the subsequent steps, we show under sufficiently accurate estimation of the MPI operator weights (θ_b and θ_d), we can make the inversion error arbitrarily small. Moreover, we drive an analytical bound on the hysteresis inversion error, which will be used later to design the controller. Let δ_{inv} denotes the hysteresis perturbation due to imperfect inversion, which can be expressed as:

$$\delta_{inv}(t) = u_o(t) - u_{in}(t) \tag{2.20}$$

The approximated MPI hysteresis operator can be expressed as;

$$\hat{F}_h = \hat{\theta}_d^T \mathcal{P}_d \left(\hat{\theta}_b^T \mathcal{P}_b \left[v; x_b(0) \right] \right) \tag{2.21}$$

Using (2.21) and by rewriting $u_{in} = \hat{F}_h \left[\hat{F}_h^{-1} \left[u_{in}; \bar{x}_b(0) \right]; x_b(0) \right]$, one can rewrite equation (2.20) as:

$$
\begin{aligned}
\delta_{inv} &= \mathcal{I}_{inv} \left[u_{in}; x_b(0) \right](t) \\
&= \theta_d^T \mathcal{P}_d \left(\theta_b^T x_b(t) \right) - \hat{\theta}_d^T \mathcal{P}_d \left(\hat{\theta}_b^T x_b(t) \right)
\end{aligned}
\tag{2.22}
$$

where $\mathcal{I}_{inv}$ denotes the operator resulted due to the inversion process. In the following proposition, we will show that the output δ_{inv} of the operator $\mathcal{I}_{inv}$ obeys a growth condition, whose upper bound is a linear function of the input u_{in} and it can be used later to design a less conservative controller as compared to the case when the inversion error is bounded by a constant such that $|\delta_{inv}| \leq k_\delta$, where k_δ is some positive constant.
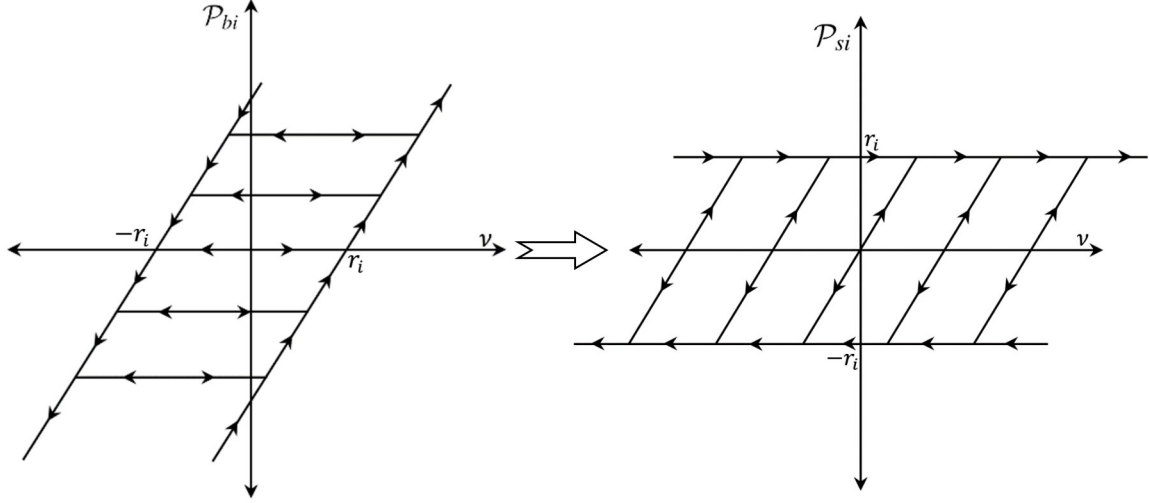
Figure 2.4: Characteristics of the backlash operator $\mathcal{P}_{bi}$ as compared to the stop operator $\mathcal{P}_{si}$.

Proposition 2.2. *Under Assumption 2.3, and if the operator $\mathcal{I}_{inv}$ is modeled as in equation (2.22), then its output $\delta_{inv}(t)$ will satisfy the following condition:*

$$|\delta_{inv}| \leq \Delta_0 |u_{in}(t)| + \Delta_1 \tag{2.23}$$

where the constants Δ_0 and Δ_1 can be calculated from the following formulas:

$$\Delta_0 = \varepsilon_{hmax} \left(\|\hat{\theta}_b\|_\infty + \|\hat{\theta}_d\|_\infty \right) \left([\sum_{i=0}^{q} |\bar{\theta}_{bi}|] \ [\sum_{j=-l}^{l} |\bar{\theta}_{dj}|] \right) \tag{2.24}$$

$$\Delta_1 = \varepsilon_{hmax} \left(\|\hat{\theta}_b\|_\infty + \|\hat{\theta}_d\|_\infty \right) \left([\sum_{i=0}^{q} |\bar{\theta}_{bi}|] \ \|\bar{r}\|_\infty + \|r\|_\infty \right) \tag{2.25}$$

where $\varepsilon_{hmax} = (q+1)(2l+1) \max \left(\|\Delta_b\|_\infty, \|\Delta_d\|_\infty \right)$ is the maximum perturbation of the weight vectors and $\|\cdot\|_\infty$ is the infinity norm.

Proof: The backlash operator $\mathcal{P}_{bi}$ with threshold r_i can be represented using the stop operator by the following formula [80]:

$$\mathcal{P}_{si}[v(t); x_{bi}(0)](t) = v(t) - \mathcal{P}_{bi}[v(t); x_{bi}(0)](t) \tag{2.26}$$

where $\mathcal{P}_{si}$ is the stop operator with threshold r_i. As shown in Fig. 2.4, the stop operator is bounded from above by its threshold r_i such that

$$|\mathcal{P}_{si}\left[\, v\left(t\right);x_{bi}\left(0\right)\right]\left(t\right)| \leq r_i \tag{2.27}$$

Therefore, using (2.27), we can show that

$$|\mathcal{P}_{bi}\left[v\left(t\right);x_{bi}\left(0\right)\right]\left(t\right) - v\left(t\right)| \leq r_i \tag{2.28}$$

From the Lipschitz property of the deadzone nonlinearity, we can show that $\mathcal{P}_{di}$ satisfies the following inequality:

$$|\mathcal{P}_{di}\left(v_1\left(t\right)\right) - \mathcal{P}_{di}\left(v_2\left(t\right)\right)| \leq |v_1\left(t\right) - v_2\left(t\right)| \tag{2.29}$$

Considering equation (2.22), by adding and subtracting the term $\left(\hat{\theta}_d^T \mathcal{P}_d \left(\theta_b^T \mathcal{P}_b \left[v\left(t\right);x_b\left(0\right)\right]\left(t\right)\right)\right)$ and by using (2.18), we can rewrite (2.22) as follows:

$$\begin{aligned}
\delta_{inv} = \Delta_d^T \mathcal{P}_d \left(\theta_b^T \mathcal{P}_b \left[v;x_b\left(0\right)\right]\left(t\right)\right) &+ \hat{\theta}_d^T \left[\mathcal{P}_d \left(\theta_b^T \mathcal{P}_b \left[v;x_b\left(0\right)\right]\left(t\right)\right)\right. \\
&\left. - \mathcal{P}_d \left(\hat{\theta}_b^T \mathcal{P}_b \left[v;x_b\left(0\right)\right]\left(t\right)\right)\right]
\end{aligned} \tag{2.30}$$

By taking the absolute value of both sides of the above equation, using inequalities (2.28) and (2.29), and applying the *Hölder's* inequality, one can get;

$$|\delta_{inv}| \leq \varepsilon_{h_{max}}\left(v\left(t\right) + \|r\|_\infty\right)\left(\|\hat{\theta}_b\|_\infty + \|\hat{\theta}_d\|_\infty\right) \tag{2.31}$$

By taking the absolute value of (2.19), we get

$$v(t) \le \left[\sum_{i=0}^{q} |\bar{\theta}_{bi}| \right] \left(\left[\sum_{j=-l}^{l} |\bar{\theta}_{di}| \right] |u_{in}(t)| + \|\bar{r}\|_{\infty} \right) \tag{2.32}$$

Finally, by inserting (2.32) back into (2.31) and arranging the terms, we can obtain (2.23). ∎

The smallness of the inversion error bound depends directly on the maximum perturbation ε_{hmax}, which depends on how accurate the MPI hysteresis model is. Therefore, the following assumption is made to characterize the smallness of the inversion error in the closed-loop system.

Assumption 2.4. *There exists a small positive constant $\varepsilon_h \le \varepsilon_{hmax}$ such that the inversion error (2.22) can be rewritten in the following form:*

$$\delta_{inv} = \mathcal{I}_b \left[u_{in}; x_b(0) \right](t) = \varepsilon_h W_{in}(t) \tag{2.33}$$

where $W_{in}(t) = \mathcal{W}_{inv}[u_{in}; W_{in}(0)](t)$ and the hysteresis operator $\mathcal{W}_{inv}$ is the composite MPI operator due to the inversion.

2.3 Adaptive Output Feedback Controller Design

2.3.1 Continuously-Implemented SMC Law Design

By using (2.20), we can convert the nonaffine hysteretic error system (2.4) into the following semi-affine system:

$$\dot{e}(t) = F_p(e(t)) + B_p(u_{in}(t) + \delta_{inv}(t)) + B_d \delta_d(t), \tag{2.34}$$

The system is called semi-affine because it has input u_{in} appearing linearly and the perturbation (inversion error δ_{inv}) is modeled with a nonlinear function of the input u_{in} as in equation (2.22).

The first step in designing the controller is to design a continuously-implemented sliding mode control law. The following surface function is considered;

$$\xi_c = k_1 e_1 + k_2 e_2 + \cdots + k_{n-1} e_{n-1} + e_n \tag{2.35}$$

where the coefficients $k_1, k_2, \cdots, k_{n-1}$ are positive and chosen to make the following polynomial

$$\lambda^n + k_{n-1}\lambda^{n-1} + \cdots + k_1$$

Hurwitz. For design purposes, the control input u_{in} is partitioned into two parts; the first part is the equivalent control u_q and the second part is the switching control u_w:

$$u_{in} = u_q + u_w \tag{2.36}$$

Let $V_c = \frac{1}{2}\xi^2$ be used as a Lyapunov function candidate. By using the control law (2.36) and calculating the time-derivative of the Lyapunov function V_c, the equivalent control u_q is designed as:

$$u_q(t,e) = \frac{1}{b}\left[-f_n(e) - \delta_e(e) - \delta_d(t)\right] \tag{2.37}$$

where $f_n(e) = -a_1 e_1 - a_2 e_2 - \cdots - a_n e_n$ and $\delta_e(e) = k_1 e_2 + \cdots + k_{n-1} e_n$.

Let the switching control law u_w be

$$u_w = -\beta_w(t,e)\,\text{sat}\left(\frac{\xi_c}{\mu}\right) \tag{2.38}$$

where β_w is the switching gain function, which will be designed shortly, $\text{sat}(\cdot)$ is a standard satu-

ration function, which is defined as follows [81]:

$$\text{sat}(v) = \begin{cases} v, & \text{if } |v| \leq 1 \\ \text{sign}(v), & \text{if } |v| > 1 \end{cases} \tag{2.39}$$

The parameter $\mu > 0$ is chosen small. To design the switching function β_w, consider the error bound inequality (2.23). By substituting the desired control law (2.36) back into the inequality (2.23), we get

$$|\delta_{inv}| \leq \Delta_1 + \Delta_0 |u_w(t,e) + u_q(t,e)| \leq \Delta_1 + \Delta_0 |u_w(t,e)| + \Delta_0 |u_q(t,e)| \tag{2.40}$$

Assuming $\Delta_0 < 1$, the switching function is designed as

$$\beta_w(t,e) = \Gamma_1 \left[\frac{\Delta_1 + \Delta_0 |u_q(t,e)|}{1 - \Delta_0} + \Gamma_0 \right] \tag{2.41}$$

where $\Gamma_0 > 0$ and $\Gamma_1 > 1$ are controller parameters. Inserting the control laws (2.36) and (2.37), and utilizing the error bound inequality (2.40), we get

$$\dot{V}_c < -b\left[\left(\Delta_1 + \Delta_0 |u_q(t,e)| \right) (\Gamma_1 - 1) + \Gamma_0 \Gamma_1 \right] |\xi_c|$$

which implies that the control law (2.36) achieves a non-zero steady-state error. In other words, if μ is chosen small enough, the closed-loop system trajectory will reach the boundary layer $\{|\xi_c| \leq \mu\}$, and will stay in there for all future time. The purpose of using the saturation function instead of the signum function in the switching control law (2.38) is to avoid the chattering of the control action; however, the drawback is that the error e will be $\mathcal{O}(\mu)$ instead of zero. To mitigate the residual error, we use the adaptive conditional servomechanism [70], [82], which will be discussed in the

27

next section.

For the output feedback case, we assume that only e_1 is available for measurement. Therefore, to reconstruct the unmeasured states, we design a high-gain observer with the following structure:

$$\dot{\hat{e}}(t) = \hat{f}_o(e) + \hat{g}_o(e_1 - \hat{e}_1) \tag{2.42}$$

where

$$\hat{f}_o = \begin{bmatrix} \hat{e}_2 \\ \hat{e}_3 \\ \vdots \\ \hat{e}_n \\ 0 \end{bmatrix}_{n \times 1}, \quad \hat{g}_o = \begin{bmatrix} \frac{h_1}{\varepsilon} \\ \frac{h_2}{\varepsilon^2} \\ \vdots \\ \frac{h_n}{\varepsilon^n} \end{bmatrix}_{n \times 1}$$

where $\hat{e}_i$ is the estimated state of e_i, ε is a small positive design parameter, and h_i is the estimation gain for i^{th} state, where the gains are chosen such that the polynomial $\lambda^n + h_1 \lambda^{n-1} + \cdots + h_{n-1} \lambda + h_n$ is Hurwitz. Accordingly, The desired control law u_{in} (2.36) and the surface function ξ_c (2.35) are modified by replacing e by $\hat{e}$.

In order to avoid the effect of observer peaking, the observer states are saturated before before being plugged into the control law. This remedy, suggested in [83], will make the control law globally bounded in its arguments in the domain of interest.

2.3.2 Adaptive Conditional Servocompensator Design

In the boundary-layer phase, due to the hysteresis inversion error, there is a non-vanishing matched perturbation δ_{inv}. In theory, the disturbance $\delta_{inv}(t)$ could contain an infinite number of harmonics of the reference signal frequency y_d. However, for practical reasons and based on the adaptive conditional servomechanism theory [70] and [82], we will assume a finite number of frequencies

to be estimated by the conditional servocompensator.

Assumption 2.5. *The hysteresis inversion error* $\delta_{inv}(t)$ *is generated by an exogenous neutrally stable linear dynamical system:*

$$\dot{\omega} = S\omega,$$

$$\delta_{inv}(t) = \Gamma\omega$$

(2.43)

where $\omega \in \varkappa \subset \mathcal{R}^m$ *is the state vector of the exosystem,* $\varkappa$ *is a compact set, and the matrices S and* Γ *are given by*

$$S = \begin{bmatrix} 0 & 1 & 0 & \ldots & 0 \\ 0 & 0 & 1 & \ldots & 0 \\ \vdots & & & & \vdots \\ 0 & \ldots & \ldots & 0 & 1 \\ c_0 & c_1 & \ldots & \ldots & c_{m-1} \end{bmatrix}_{m \times m},$$

$$\Gamma = \begin{bmatrix} 1 & 0 & \ldots & \ldots & 0 \end{bmatrix}_{1 \times m}$$

The above assumption means that the disturbance δ_{inv} is a linear combination of constant and sinusoidal components. The word "conditional" means that the servocompensator is designed to be active only when the sliding surface variable ξ_c enters the boundary layer $\{|\xi_c| \leq \mu\}$. Let ξ be the new sliding surface variable, which has the servocompensator part, such that

$$\hat{\xi} = K_{\vartheta}^T \vartheta + \hat{\xi}_c$$

(2.44)

where $\vartheta \in \mathcal{R}^m$ is the conditional servocompensator state vector. The conditional servocompensator dynamics are described as:

$$\dot{\vartheta} = A_{\vartheta}\vartheta + \mu B_{\vartheta} \mathrm{sat}\left(\hat{\xi}/\mu\right)$$

(2.45)

K_ϑ is a unique servomechanism gain vector, which will make the eigenvalues of matrix $\left(A_\vartheta + B_\vartheta K_\vartheta^T\right)$ equal to the eigenvalues of S, and the pair $(A_\vartheta, B_\vartheta)$ is chosen such that they are in the controllable canonical form

$$A_\vartheta = \begin{bmatrix} 0 & 1 & 0 & \cdots & 0 \\ 0 & 0 & 1 & \cdots & 0 \\ \vdots & & & & \vdots \\ 0 & \cdots & \cdots & 0 & 1 \\ * & * & * & * & * \end{bmatrix}_{m \times m} \qquad B_\vartheta = \begin{bmatrix} 0 \\ 0 \\ \vdots \\ 0 \\ * \end{bmatrix}_{m \times 1}$$

where the matrix A_ϑ is Hurwitz, therefore if $\vartheta(0)$ is $\mathcal{O}(\mu)$, $\vartheta(t)$ will be $\mathcal{O}(\mu)$ also.

To include the servomechanism in the control law, the switching control law u_w (2.38) is modified to

$$u_w = -\beta_w(t,e)\,\text{sat}\left(\frac{\hat{\xi}}{\mu}\right) \tag{2.46}$$

Let N be the solution of the following Sylvester equation

$$NS - SN = -P^{-1}B_\vartheta\left(\Gamma + K_\vartheta^T PN\right)$$

It has been established in [84] that the existence and uniqueness of the solution N is ensured if A_ϑ and S have no common eigenvalues. In addition to that, if the pair $(A_\vartheta, B_\vartheta)$ is controllable and the pair (S, Γ) is observable, the matrix N is non-singular [84]. The matrix P is a unique non-singular similarity transformation matrix such that

$$P^{-1}\left(A_\vartheta + B_\vartheta K_\vartheta^T\right)P = S, \quad P^{-1}B_\vartheta = [0\ 0\ \cdots\ 0\ 1]^T$$

If the eigenvalues of the exosystem (2.43) are unknown, which is due to the frequencies of the

30

inversion error $\delta_{inv}(t)$ being unknown, it is needed to manipulate K_ϑ in (2.44) online with an adaptation law. Let $\hat{K}_\vartheta$ be the manipulated servomechanism gain vector. The adaptation law is designed to change the eigenvalues of the matrix $\left(A_\vartheta + B_\vartheta \hat{K}_\vartheta^T\right)$ online to become equal to the eigenvalues of S. To lower the number of adapted variables, we use the partial adaptation as suggested in [70], by defining the following vectors

$$\lambda_\vartheta = \mathcal{I}_\vartheta K_\vartheta \quad \text{and} \quad v_\vartheta = \mathcal{I}_\vartheta \vartheta$$

where $\lambda_\vartheta \in \mathcal{R}^\iota$, $v_\vartheta \in \mathcal{R}_\iota$, and $\iota \leq m$ is the number of the adapted variables, $\mathcal{I}_\vartheta$ is $(\iota \times m)$ matrix with its rows are unit vectors, and v_ϑ represents the adaptive regressor vector. As we mentioned above, the pair $(A_\vartheta, B_\vartheta)$ is in the controllable canonical form, implying that the number of adaptation variables are

$$\iota = \begin{cases} \frac{m}{2}, & \text{if the number of frequencies is even} \\ \frac{m-1}{2}, & \text{if the number of frequencies is odd} \end{cases}$$

With the assumption that λ_ϑ belongs to the convex hypercube $\varkappa_\vartheta = \{\lambda_\vartheta | a_i \leq \lambda_{\vartheta_i} \leq b_i, 1 \leq i \leq \iota\}$, the adaptation law can be designed as

$$\dot{\hat{\lambda}}_\vartheta = \beta_\vartheta \left(\hat{\xi}, \mu\right) \mathcal{P}r \left(\gamma_\vartheta \left(\hat{\xi}_c, v_\vartheta, \beta_w\right)\right)$$

$$\& \ \gamma_\vartheta \left(\hat{\xi}_c, v_\vartheta, \beta_w\right) = \gamma_\vartheta \beta_w v_\vartheta \left(\mu_\vartheta \mathrm{sat}\left(\hat{\xi}_c/\mu_\vartheta\right)\right)/\mu^2$$

(2.47)

where the function $\mathcal{P}r(\cdot)$ is a parameter projection operator that retains $\hat{\lambda}_\vartheta$ in $\varkappa_\delta \supset \varkappa_\vartheta \ \forall t \geq 0$, where $\varkappa_\delta = \{\lambda_\vartheta | a_i - \delta \leq \lambda_{\vartheta_i} \leq b_i + \delta, 1 \leq i \leq \iota\}$, and $\delta > 0$. γ_ϑ is the adaptation gain. The function $\left(\mu_\vartheta \mathrm{sat}\left(\hat{\xi}_c/\mu_\vartheta\right)\right)$ and $0 < \mu_\vartheta < \mu$ is the componentwise smooth projection $\mathcal{P}r\left(\gamma_\vartheta \left(\hat{\xi}_c, v_\vartheta, \beta_w\right)\right)$

is defined by

$$
\left[\mathcal{P}_r \left(\gamma_{\vartheta} \left(\cdot \right) \right) \right]_i =
\begin{cases}
\left(1 + \dfrac{b_i - \hat{\lambda}_{\vartheta_i}}{\delta} \right) \gamma_{\vartheta_i} & \text{if } \hat{\lambda}_{\vartheta_i} > b_i \text{ and } \gamma_{\vartheta_i} > 0 \\[2ex]
\left(1 + \dfrac{\hat{\lambda}_{\vartheta_i} - a_i}{\delta} \right) \gamma_{\vartheta_i} & \text{if } \hat{\lambda}_{\vartheta_i} < a_i \text{ and } \gamma_{\vartheta_i} < 0 \\[2ex]
\gamma_{\vartheta_i} & \text{Otherwise}
\end{cases}
$$

The function $\beta_{\vartheta} \left(\hat{\xi}, \mu \right)$ is defined as:

$$
\beta_{\vartheta} \left(\hat{\xi}, \mu \right) =
\begin{cases}
0 & \text{if } |\hat{\xi}| \geq 2\mu \\[2ex]
1 & \text{if } |\hat{\xi}| \leq \mu \\[2ex]
1 - \dfrac{|\hat{\xi}| - \mu}{\mu} & \text{if } \mu < |\hat{\xi}| < 2\mu
\end{cases}
$$

The purpose of the function $\beta_{\vartheta} \left(\hat{\xi}, \mu \right)$ is to keep $\hat{\lambda}_{\vartheta}$ constant outside the boundary set $\{ |\hat{\xi}| \leq 2\mu \}$.

2.3.3   Output-feedback Closed-loop System Dynamics

The closed-loop dynamics under output feedback are composed of the exosystem dynamics (2.43), the conditional servomechanism (2.45), the semi-affine error dynamics (2.34), the adaptation law (2.47), the time-derivative of the modified sliding mode surface function (2.44) and the high-gain observer dynamics (2.42). By inserting the output feedback control law (2.36) into equations (2.44) and (2.42) and then doing algebraic manipulation, we can derive the closed-loop system in compact form as follows;

$$
\dot{\mathcal{X}}(t) = \mathcal{F}_{cl}(t, \mathcal{X}, W_{in}) = \bar{\mathcal{F}}_{cl}(t, \mathcal{X}) + \varepsilon_h \mathcal{D}_{inv}(\mathcal{X}, W_{in}) \tag{2.48}
$$

where $\mathcal{F}_{cl}$ is the closed-loop system under hysteresis inversion, $\bar{\mathcal{F}}_{cl}$ is hysteresis-free closed-loop system ($\delta_{inv}(t) = 0$), $\mathcal{D}_{inv}(\mathcal{X}, W_{in}) = \mathcal{B}_{inv} W_{in}(t)$, and these functions are defined as:

$$\bar{\mathcal{F}}_{cl}(t,\mathcal{X}) = \begin{bmatrix} S\omega \\ A_\vartheta \vartheta + \mu B_\vartheta \operatorname{sat}\left(\frac{\xi - L(\varepsilon)\phi}{\mu}\right) \\ A_\zeta \zeta + B_\zeta \left(\xi - \hat{K}_\vartheta^T \vartheta\right) \\ \Delta_{d_1}(\cdot) + \Delta_{d_2}(\cdot) - b\beta_w(t,\hat{e})\operatorname{sat}\left(\frac{\xi - L(\varepsilon)\phi}{\mu}\right) \\ \varepsilon^{-1} A_\phi \phi + B_\phi \left[-\delta_e(e) - b\beta_w(t,\hat{e})\operatorname{sat}\left(\frac{\xi - L(\varepsilon)\phi}{\mu}\right)\right] \\ \beta_\vartheta\left(\hat{\xi},\mu\right) \; \mathcal{P}_r\left(\gamma_\vartheta\left(\hat{\xi}_c, v_\vartheta, \beta_w\right)\right) \end{bmatrix},$$

$$\mathcal{B}_{inv} = [0,0,0,b,b,0]^T,$$

where $\mathcal{X} = [\omega, \vartheta, \zeta, \xi, \phi, \lambda_\vartheta]^T$, the pairs $\left(A_\zeta, B_\zeta\right)$ and $\left(A_\varphi, B_\varphi\right)$ are in controllable and observable canonical forms, respectively, and the matrices A_ζ and A_φ are Hurwitz. The state vector ϕ is the scaled estimation variable, which is defined as:

$$\varphi_i = \frac{1}{\varepsilon^{n-i}}(e_i - \hat{e}_i)$$

The other terms and variables are defined as follows:

$$\Delta_{d_1}(\cdot) = \hat{K}_\vartheta^T A_\vartheta \vartheta + \mu \hat{K}_\vartheta B_\vartheta \operatorname{sat}((\xi - L(\varepsilon)\varphi)/\mu) + \dot{\hat{\lambda}}_\vartheta v_\vartheta,$$

$$\Delta_{d_2}(\cdot) = \sum_{n-1}^{i=1} k_i e_{i+1} - \delta_e(e),$$

$$\zeta^T = [e_1 \; e_2 \; \dots \; e_{n-1}],$$

$$\phi^T = [\phi_1 \; \phi_2 \; \dots \; \phi_n],$$

$$L(\varepsilon) = \begin{bmatrix} k_1\varepsilon^{n-1} & k_2\varepsilon^{n-2} & k_3\varepsilon^{n-3} & \cdots & k_{n-1}\varepsilon & 1 \end{bmatrix},$$

Notice that the closed-loop system dynamics (2.48) include some nonlinearities, for example, the saturation function in the control law (2.38) and the projection function in the adaptation control law (2.47). For the purpose of conducting the analysis in the next section, the following assumption is needed. Moreover, Lemma 2.1 is needed to establish the exponential stability of the hysteresis-free closed-loop system.

Assumption 2.6. *If the desired reference input y_d is T-periodic, then there exists a unique T-periodic solution $\mathcal{X}_T(t)$ for the hysteresis-free closed-loop system $\bar{\mathcal{F}}_{cl}(t, \mathcal{X})$ in (2.48).*

Lemma 2.1. *(Exponential Stability of the Hysteresis-Free Closed-loop System) Suppose Assumptions 2.1-2.5 are satisfied. Consider the hysteresis-free closed-loop system*

$$\dot{\mathcal{X}}(t) = \bar{\mathcal{F}}_{cl}(t, \mathcal{X}) \tag{2.49}$$

under ideal hysteresis inversion ($\delta_{inv}(t) = 0$). Let $\Omega_1 \subset \mathcal{R}$, $\Omega_2 \subset \mathcal{R}^n$, $\Omega_3 \subset \mathcal{R}^n$, and $\Omega_4 \subset \mathcal{R}^m$ be compact sets. Let $\vartheta(0) = \mathcal{O}(\mu)$ and v_0 and $\hat{\zeta}(0)$ be bounded. Let the switching control under the hysteresis-free case are chosen as:

$$u_w = -\beta_{wmax}sat\left(\frac{\xi}{\mu}\right)$$

where $\beta_{wmax} = \max_{e \in \Omega_1, \, t \geq 0}\{\beta_w(t,e)\}$. Then, there is $\mu^* > 0$, such that for every $\mu \in (0, \mu^*]$, there is $\varepsilon^* = \varepsilon^*(\mu) > 0$ such that for every $\mu \in (0, \mu^*]$ and $\varepsilon \in (0, \varepsilon^*]$ and for all initial conditions $\xi(0), e(0) \in \Omega_1 \times \Omega_2$, $\hat{e}(0) \in \Omega_3$, $\vartheta(0) \in \Omega^m$, $\hat{\lambda}_\vartheta \in \varkappa_\vartheta$, if $\bar{v}_\vartheta$ is persistently exciting, then the closed-loop variables vector $\mathcal{X}$ is bounded $\forall t \geq 0$ and the hysteresis-free closed-loop system

$\bar{\mathcal{F}}_{cl}(t, \mathcal{X})$ *has an exponentially stable equilibrium point at* $\left(e = 0, \tilde{\vartheta} = 0, \hat{e} = 0, \tilde{\lambda}_{\vartheta} = 0\right)$, *where* $\tilde{\vartheta} = \vartheta - \bar{\vartheta}$, $\tilde{\lambda}_{\vartheta} = \hat{\lambda}_{\vartheta} - \lambda_{\vartheta}$, $\bar{v}_{\vartheta}$ *is the regression vector, and* $\bar{\vartheta}$ *is the servocompensator state vector in the boundary-layer stage.*

The proof of this lemma is carried out by repeating the steps of the proof of Theorem 1 in [70] for the hysteresis-free closed-loop system $\bar{\mathcal{F}}_{cl}(t, \mathcal{X})$.

2.4   Well-Posedness and Periodic Stability of the Closed-Loop System With Hysteresis Inversion Perturbations

Before proving the existence of an exponentially stable, periodic solution of the closed-loop system dynamics under hysteresis inversion (2.48), we need to establish that the system (2.48) is well-posed. By establishing well-posedness, we mean establishing the existence and uniqueness of the solution of the closed-loop system (2.48).

Theorem 2.1. *(Well-Posedness of the Hysteretic Closed-loop System) Consider the closed-loop system under hysteretic inversion perturbation (2.48). Let* $\Omega_{\mathcal{X}} \subset \mathcal{R}^{rc}$ *and* $\Omega_{\mathcal{H}} \subset \mathbb{W}_t^{1,1}$ *be compact sets and are defined as:*

$$\Omega_{\mathcal{X}} := \{\mathcal{X} \in \mathcal{R}^{rc} : \|\mathcal{X}(t) - \mathcal{X}(0)\|_1 \leq r_{\mathcal{X}}\}$$

$$\Omega_{\mathcal{H}} := \{W_{in} \in \mathbb{W}_t^{1,1} : \|W_{in}(t) - W_{in}(0)\|_{\mathbb{W}_t^{1,1}} \leq r_{\mathcal{H}}\}$$

where $r_c = 2n + 2m + \iota$ *and* $r_{\mathcal{X}}$, $r_{\mathcal{H}} > 0$. *Under the piecewise continuity of the function* $\mathcal{F}_{cl}(t, \mathcal{X}, W_{in})$

in t and from its local Lipschitz property in arguments $\mathcal{X}$ and W_{in}, such that the condition

$$\|\mathcal{F}_{cl}\left(t,\mathcal{X}_1,W_{in_1}\right) - \mathcal{F}_{cl}\left(t,\mathcal{X}_2,W_{in_2}\right)\|_1$$

$$\leq L_{\mathcal{X}}\|\mathcal{X}_1(t) - \mathcal{X}_2(t)\|_1 + L_W\|W_{in_1}(t) - W_{in_2}(t)\|_1 \quad (2.50)$$

is satisfied for any $\mathcal{X}_1$, $\mathcal{X}_1 \in \Omega_{\mathcal{X}}$ and W_{in_1}, $W_{in_2} \in \Omega_{\mathcal{H}}$ $\forall t \in [0,t_u]$, where $t_u > 0$, then there exists $0 < t_c < t_u$, such that the system (2.48) has a unique solution $\mathcal{X}_T(t)$ for all $\mathcal{X}(0) \in \Omega_{\mathcal{X}}$ and $W_{in}(0) \in \Omega_{\mathcal{H}}$ over the time interval $[0,t_c]$.

The proof of this theorem can be found in Appendix A.1. By establishing the well-posedness of the hysteretic closed-loop system (2.48), we are now prepared to prove its periodic stability. Define $u_{in}^T = \alpha_{in}(\mathcal{X}_T)$ and $v^T = F_h^{-1}\left[u_{in}^T;\bar{x}_b(0)\right](t)$. Under Assumptions 2.1 - 2.6, u_{in}^T will be T-periodic and v^T will also be T-periodic, but after some transient period of time. To prove the existence of an exponentially stable periodic solution of the hysteretic closed-loop system (2.48), we need to establish the existence of a contraction property for the composite hysteresis operator $\mathcal{W}_{in}$ resulted due to the inversion. This property can be established for a T-periodic reference input $y_d(t)$ if $u_{in}(t)$ and $v(t)$ satisfy the following condition.

Assumption 2.7. *For any absolute continuous function v_c, define its oscillation within the time interval $[t_1,t_2]$ as*

$$osc_{[t_1,t_2]}[v_c] = \sup_{t_1 \leq \tau_1,\tau_2 \leq t_2} |v_c(\tau_1) - v_c(\tau_2)|$$

Assume

$$osc_{[0,T]}\left[\Sigma_{-l}^l \theta_{d_i}\mathcal{P}_{d_i}\left(u_{in}^T\right)\right] > 2\bar{r}_{max}$$

$$\& \qquad osc_{[T,2T]}[v_T] > 2r_{max}$$

where $r_{max} = \|r\|_\infty$ and $\bar{r}_{max} = \|\bar{r}\|_\infty$.

Theorem 2.2. *(Periodic Stability of the Hysteretic Closed-loop System) Consider the hysteretic closed-loop system (2.48). Let Assumptions 2.1 - 2.7 be satisfied and let $\bar{\Omega}_\mathcal{X} \subset \mathcal{R}^{rc}$ and $\bar{\Omega}_\mathcal{H} \subset \mathbb{W}_t^{1,1}$ be compact sets. Assume $\Delta_0 < 1$, under the exponential stability of the hysteretic-free closed-loop system (2.49), then there exists $\varepsilon_h^* \leq \varepsilon_{h_{max}}$, such that for all the initial conditions $\mathcal{X}(0) \in \bar{\Omega}_\mathcal{X}$ and $W_{in}(0) \in \bar{\Omega}_\mathcal{H}$, the solution $\mathcal{X}(t)$ of the hysteretic closed-loop system (2.48) will converge exponentially to a unique periodic solution $\mathcal{X}_T(t)$.*

Proof: Consider the ith backlash operator $\mathcal{P}_{b_i}$ with radius r_i in Eq. (2.7), for the input $u_{in}(t)$ with $osc_{[0,T]} > 2r_i$ and two different initial conditions $\mathcal{X}_{b_i}^a(0)$ and $\mathcal{X}_{b_i}^b(0)$. It can be seen that the backlash operator $\mathcal{P}_{b_i}$ has the following property

$$|\mathcal{P}_{b_i}\left[u_{in}; \mathcal{X}_{b_i}^a(0)\right](t) - \mathcal{P}_{b_i}[u_{in}; \mathcal{X}_{b_i}^b(0)](t)| = 0, \ \ \forall t > T \tag{2.51}$$

This mainly follows the essential properties of the backlash operator (2.7), where its output oscillation becomes independent of the initial condition once its input oscillation amplitude exceeds $2r_i$. Refer to the composite MPI operator $\mathcal{W}_{in}$ in (2.33) resulting from the inversion process. This operator is a composition of the inverse MPI operator F_h^{-1} (whose largest radius is $\bar{r}_{max}$) and the MPI operator F_h (whose largest radius is r_{max}). Using the property (2.51) and Assumption 2.7, we can show that the operator $\mathcal{W}_{in}$ obeys the following contraction property:

$$|\mathcal{W}_{in}[u_{in}; x_{inv}^a(0)](t) - \mathcal{W}_{in}[u_{in}; x_{inv}^b(0)](t)| = 0 \ \ \forall t > 2T \tag{2.52}$$

where $x_{inv}^a(0)$ and $x_{inv}^b(0)$ are two different applicable initial inputs. Notice that even if $\mathcal{W}_{in}$ operator includes deadzone nonlinearities, we still can establish the contraction property (2.52). This is because the deadzone nonlinearity is memory-less and preserves the local Lipschitz property. Similarly, by using the property (2.52) along with Assumption 2.7, we can show that the shift operator

Sh^{ε_h} defined as:

$$Sh^{\varepsilon_h} : (\mathcal{X}(0), W_{in}(0)) \rightarrow (\mathcal{X}(2T), W_{in}(2T)) \tag{2.53}$$

has a contraction property for $\varepsilon_h > 0$. Since the MPI operator $\mathcal{W}_{in}$ satisfies both the Volterra and semi-group properties [14], also from Proposition 2.1, we can show that

$$|W_{in}(t)| \leq \bar{\Delta}_0 |\mathcal{X}(t)| + \bar{\Delta}_1$$

where $\bar{\Delta}_0$ and $\bar{\Delta}_1$ are positive constants and are function of the constants Δ_0 and Δ_1 of inequality (2.23). From Lemma 2.1, under the persistency of excitation of the regressor vector $\bar{v}_{\vartheta}$, we can show that the hysteresis-free closed-loop system (2.49) is T-convergent about $\mathcal{X}_T$ [68]. From Theorem 2.1, we have established the existence and uniqueness (well-posedness) of the solution of the hysteretic closed-loop system (2.48). Therefore, by following similar steps to those of Theorem (2.1) of [68], we can establish that the solution of the hysteretic closed-loop system (2.48) will converge exponentially to a unique periodic solution when ε_h is sufficiently small. ■

In Theorem 2.2, we have established that the solution of the closed-loop system converges exponentially to a periodic solution provided the inversion error is sufficiently small. Furthermore, it can be shown that an ultimate bound on the tracking error can be reduced by reducing the controller parameters μ and ε. The ultimate boundedness can be established by following similar steps in the proofs of Theorems 1 and 2 of [85]. The first step is to show that the closed-loop systems variables in the reaching phase will converge exponentially to a positively-invariant set that is parameterized by the parameters (μ and ε), which can shrink to zero set if these two parameters are pushed to zero. The second step is to establish that the closed-loop system variables in the boundary layer phase are ultimately bounded by a bound that depends on the controller parameters (μ and ε) and the inversion error perturbation $\varepsilon_h \mathcal{D}_{inv}(\mathcal{X}, W_{in})$.

2.5 Experimental Results

In this section, we examine the performance of the proposed control scheme by implementing tracking experiments on a commercial piezo-actuated nanopositioner stage (Nano OP-56) shown in Fig. 2.5. Experiments on this platform, manufactured by Mad City Labs Inc., provides a practical importance to benchmark our controller in handling hysteretic disturbances. Position measurement is provided by a built-in capacitive sensor. The travel range of the nanopositioner is $\pm 65\ \mu$m. The power amplifier unit (Nano Drive, Mad City Labs, Inc.) drives the piezo actuator and has a gain of 15. In the system setup, the manipulated control input is the one to the power amplifier instead of the actual voltage input to the piezo actuator. For real-time implementation, the controller is deployed in a dSPACE (DS1104) platform using Matlab/simulink real-time coder tools.

The nanopositioner system is modeled with a second order nonlinear system in the form of equation (2.1). The hysteresis part is modeled with an MPI operator with 8 play operators and 9 dead-zone units, and the weights and thresholds are identified as:

$$
\begin{aligned}
\hat{\theta}_b^T &= [0.719, 0.183, 0.035, 0.055, 0.034, 0.033, 0.023, 0.061], \\
r^T &= [0, 0.33, 0.66, 1.00, 1.33, 1.66, 2.00, 2.33],
\end{aligned}
$$

$$
\begin{aligned}
\hat{\theta}_d^T &= [1.062, 0.473, 0.641, 0.311, 8.426, -0.636, -0.501, -0.614, -0.415], \\
d^T &= [-2.68, -1.97, -1.22, -0.42, 0, 0.32, 1.02, 1.76, 2.57],
\end{aligned}
$$

The linear part of the model is identified using frequency-based identification methods and its parameters are found to be $a_1 = 1.795 \times 10^8$, $a_2 = 5696.88$, and $b = 1.063 \times 10^9$. Notice that due to the system high resonant frequency, the identified parameters are very large.

The high-gain observer (2.42) is implemented with the gains h_1 and h_2 being 3 and 20, respectively. The parameter ε is taken as 0.0001. For the parameters of the switching function $\beta_w(\cdot)$ in
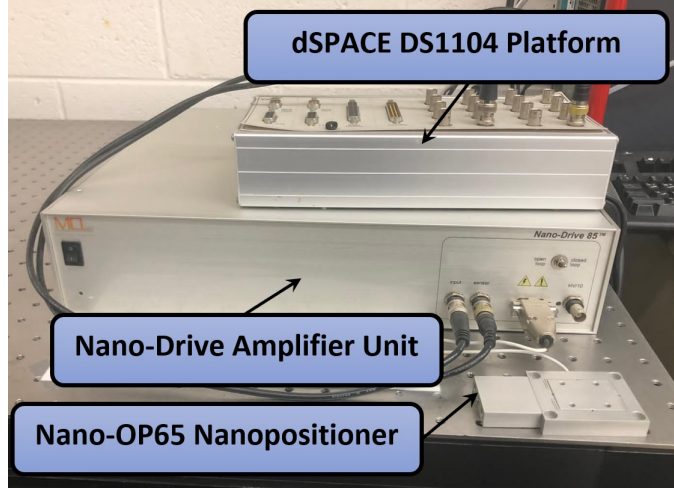
(a)

(b)

Figure 2.5: Experimental setup of the the nanopositioner system. (a) The complete setup including the nanopositioner stage Nano-OP65, Nano-Drive power amplifier unit, and the dSPACE DS1104 data acquisition interface unit; (b) Magnified picture of the nanopositioner stage Nano-OP65.

(2.46), we calculate first the constants Δ_0 and Δ_1 of the bound (2.23) by using the formulas (2.24) and (2.25). From the identified weights and thresholds of the MPI hysteresis model mentioned above, we calculate the following:

$$\|\hat{\theta}_b\|_\infty = 0.719, \quad \|\hat{\theta}_d\|_\infty = 8.426, \quad \text{and } \|r\|_\infty = 2.33,$$

Then we use the procedure provided in [38] to calculate the inverse MPI operator parameters, and accordingly we find;

$$\sum_{i=0}^{7} |\bar{\theta}_{bi}| = 1.9082, \quad \sum_{j=-4}^{4} |\bar{\theta}_{dj}| = 0.187, \quad \text{and} \quad \|\bar{r}\|_{\infty} = 2.2379,$$

To ensure periodic stability, one major assumption of Theorem 2.2 is $\Delta_0 < 1$. To comply with this assumption, let $\varepsilon_{hmax} = 0.015$, and then with formulas (2.24) and (2.25), the error bound (2.23) constants can be computed as $\Delta_0 = 0.9058$ and $\Delta_1 = 0.049$. The rest of the switching function (2.41) parameters are chosen as; $\Gamma_1 = \Gamma_2 = 10$. We choose the sliding function (2.35) constant $k_1 = 5000$ and the boundary layer width constant $\mu = 1000$.

For the adaptive servocompensator, we assume that the residual disturbance in the boundary-layer phase (due to hysteresis inversion) has only in its frequency spectrum the fundamental frequency of the desired reference input. Moreover, we assume that there is an additional bias disturbance term alongside the periodic disturbance terms. As a result, the internal model will be a third order model (namely a second order model augumented with an integrator state).

To ensure the robustness of the adaptation law (2.47) against noise inputs and the observer peaking effect, the adaptation parameter λ_{ϑ} is assumed to be retained in the following convex set;

$$\varkappa_{\delta} = \{\lambda_{\vartheta} | -8.1 \leq \lambda_{\vartheta} \leq 8.1\}$$

The remaining adaptation law parameters are chosen as; $\gamma_{\vartheta} = 2.68 \times 10^5$, and $\mu_{\vartheta} = 1$. In our experiments, we test the proposed controller using three types of desired reference signals. The first one is a sinusoidal input defined as

$$y_d(t) = 10 \sin(2\pi f t) + 10 \ \mu\text{m}$$
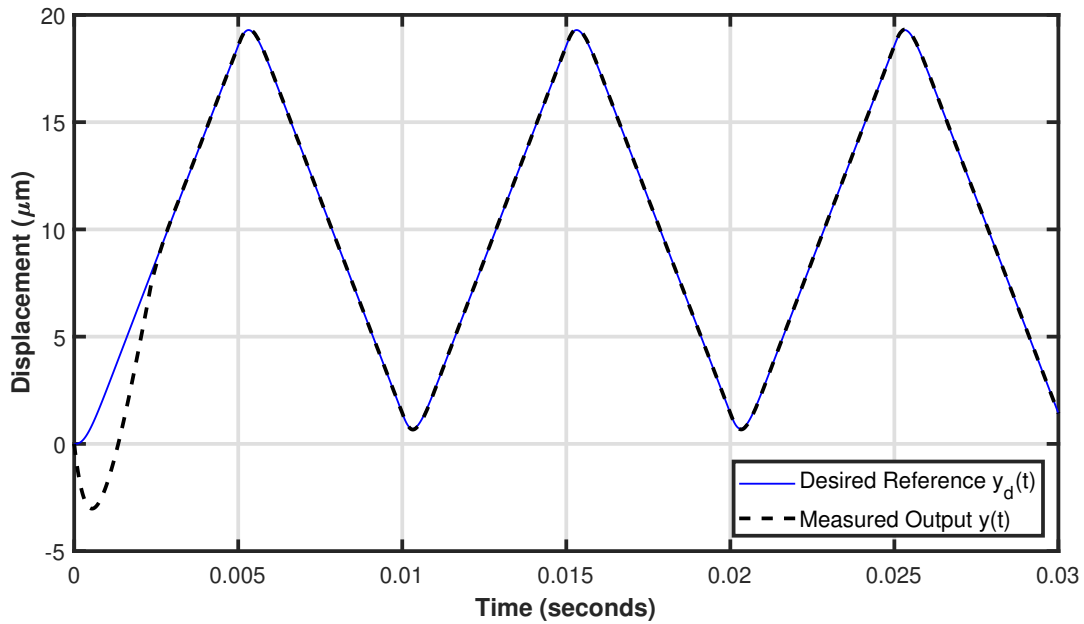
Figure 2.6: Measured displacement versus sawtooth desired reference with 100 Hz frequency using the inversion-based ACS.
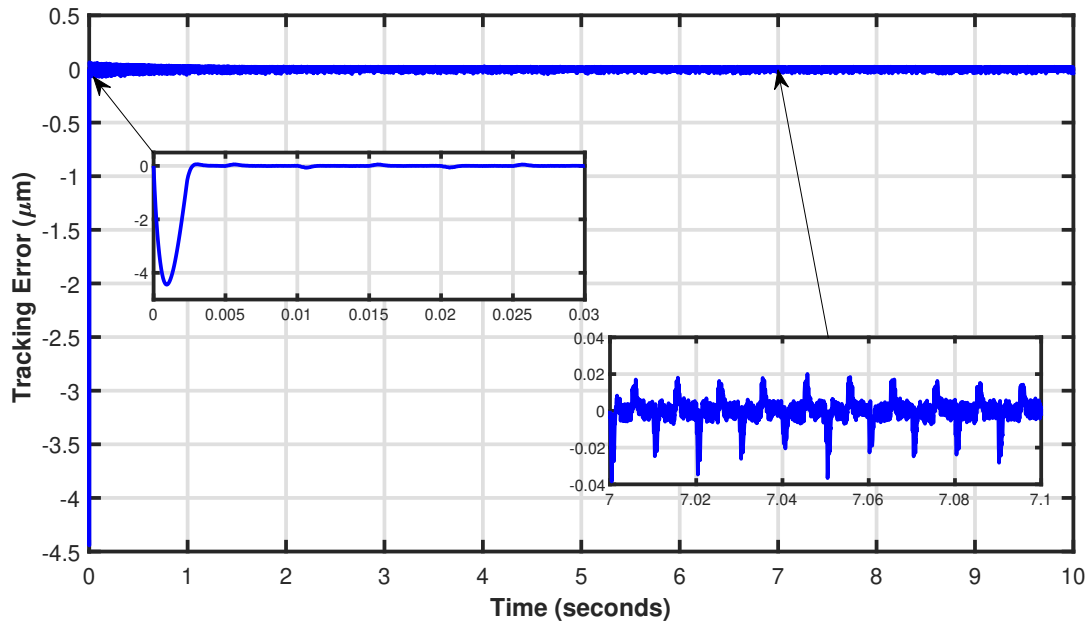
Figure 2.7: Tracking error with a sawtooth reference with 100 Hz frequency.

with frequency $f = 5$, 25, 50, and 100 Hz. It is worth mentioning that we published part of our evaluation results using sinusoidal reference in [86]. Therefore, we are not going to repeat these re-
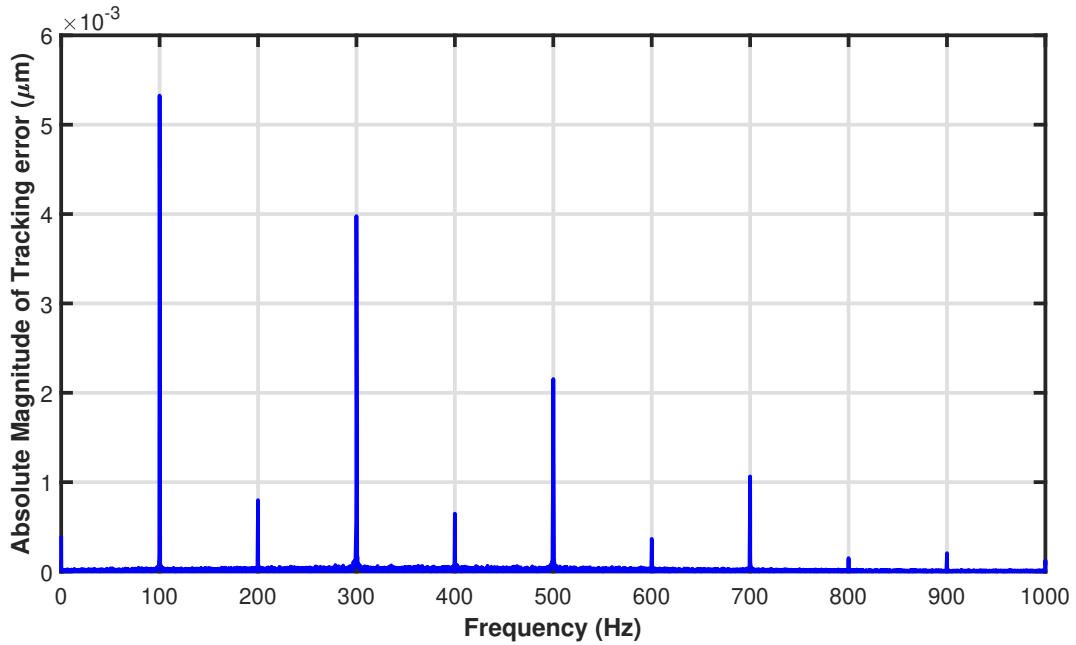
Figure 2.8: Frequency spectrum of the tracking error with a 100 Hz sawtooth reference in the boundary-layer phase.
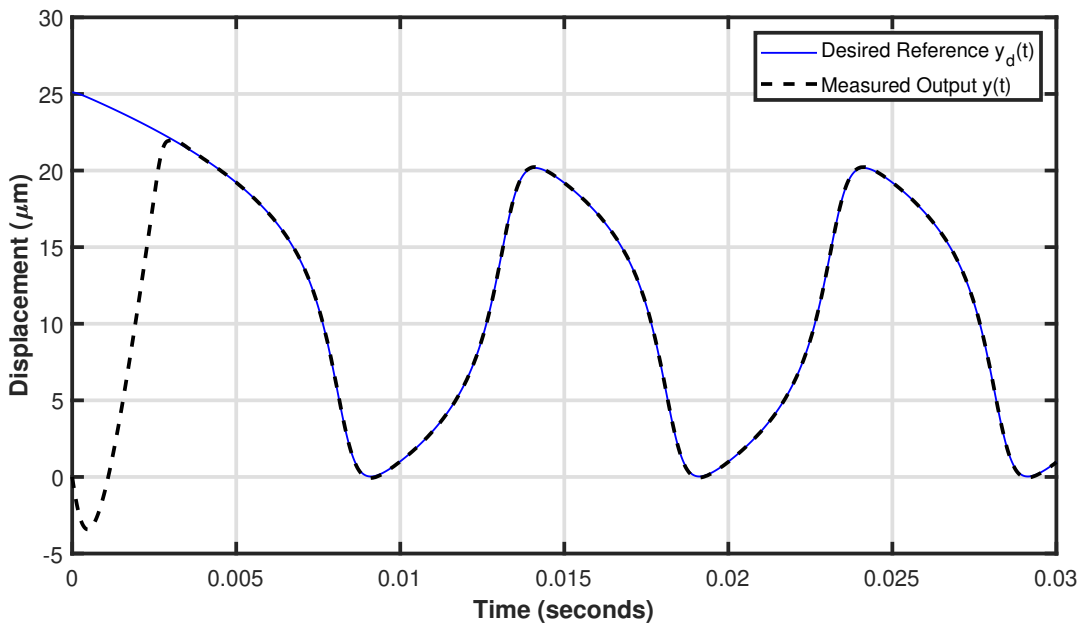
Figure 2.9: Measured displacement versus van der Pol desired reference with 100 Hz frequency using the inversion-based ACS.

sults in this chapter. In Tables 2.1 and 2.2, we conduct a comparison between the achieved tracking

error accuracy of our proposed approach in the boundary-layer phase as compared to other control

43
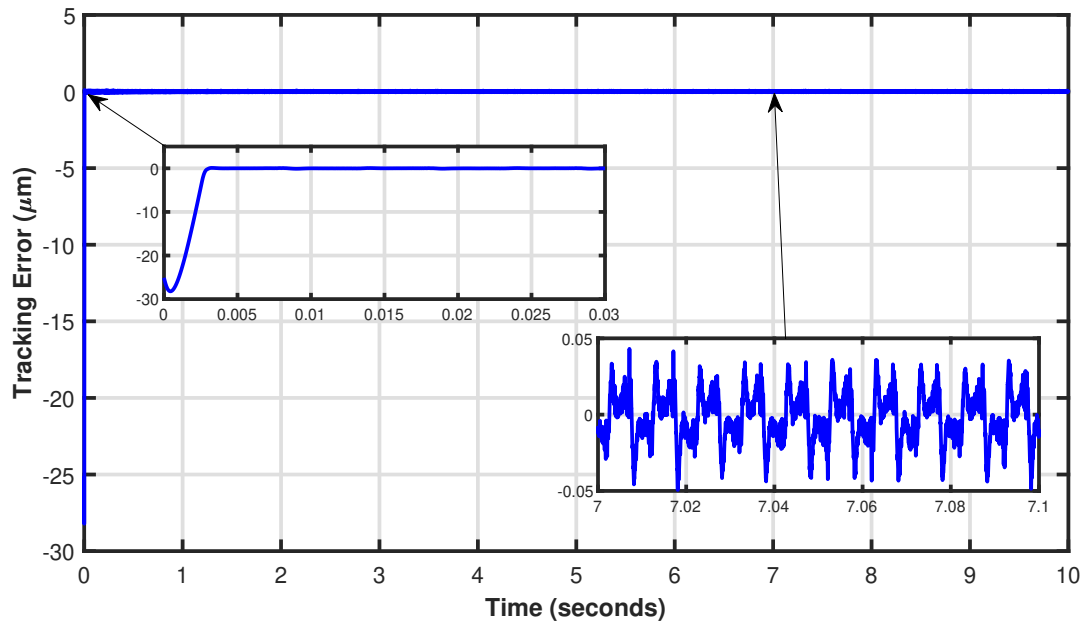
Figure 2.10: Tracking error with a van der Pol reference with 100 Hz frequency.
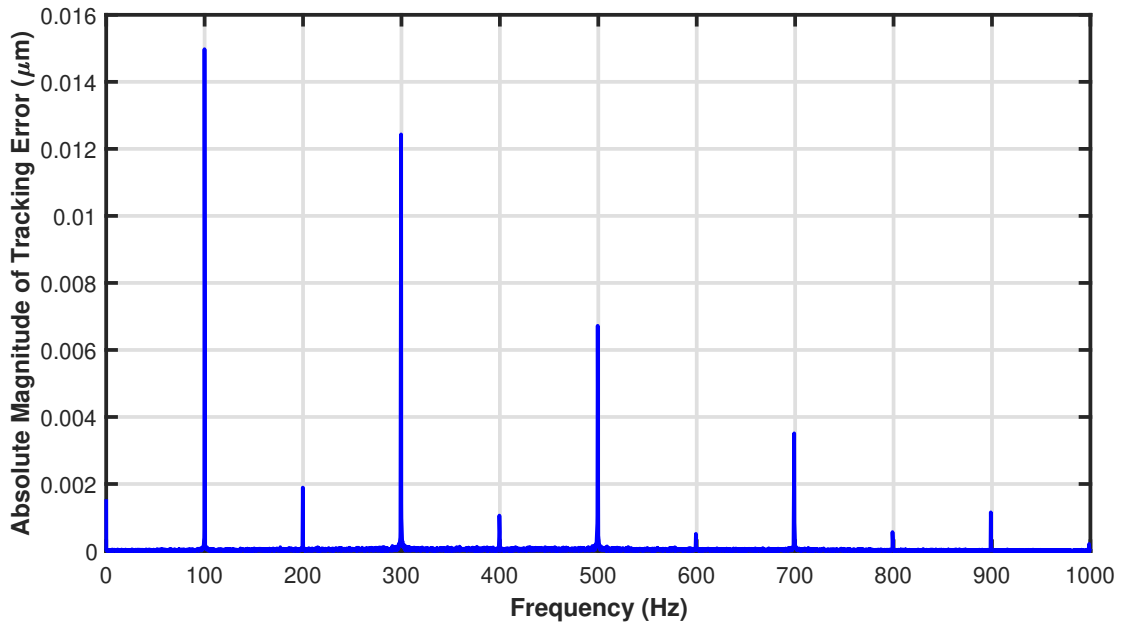
Figure 2.11: Frequency spectrum of the tracking error with a 100 Hz van der Pol reference in the boundary-layer phase.

approaches proposed in previous projects implemented on the same experimental setup, including

a) the inversion-based sliding mode controller proposed in [48], which will be abbreviated as SMC,

b) the results of [5], in which both of Single Harmonic Servo-Compensator (SHSC) and Multi-Harmonic Servo-Compensator (MHSC) are designed and implemented, c) the results obtained from combining extended high-gain observer and the dynamic inversion approaches (EHGO-DI), which appears in [69], and d) a classical PI controller without hysteresis inversion implemented experimentally by the authors and its gains are chosen to yield the best possible performance.

In Table 2.1 and 2.2, we show the percentage of the maximum absolute tracking error and the percentage of the mean absolute tracking error with respect to the maximum peak. It can be noticed in both tables that the inversion-based adaptive conditional servocompensator approach (Inv-B ACS) results have greatly outperformed the other five approaches in reducing the tracking errors for all frequencies. The trend in both tables shows that the next best tracking results is the extended high-gain observer combined with dynamics inversion (EHGO-DI) approach. Notice that the mean percentage absolute error for the EHGO-DI approach is higher than the Inv-B ACS one by almost 7 folds for the 100 Hz frequency.

The second round of experiments are done using a sawtooth desired reference with the same frequencies used with the sinusoidal reference (frequencies 5, 25, 50, and 100 Hz). A second order pre-filter is inserted to smooth out the reference signal to avoid spiking impulses at the signal edges. The measured output displacement $y(t)$ under the inversion-bases ACS control method for the 100 Hz frequency reference case is shown in Figure 2.6. In Figure 2.7, the tracking error $e_1(t)$ is presented. The magnified sub-figure to the left side shows the tracking error response for the first 0.03 seconds. Notice that the tracking error is converging quickly in around 0.003 seconds. Another magnified sub-figure added to the right to show an instant of the tracking error in the boundary-layer phase (7.0-7.1 seconds). Notice that the error is not increasing in the period (0.03-10 seconds).

In Figure 2.8, we show the frequency spectral content of the tracking error in the boundary

layer phase (0.03-10 seconds) for the 100 Hz reference. It is noticed that we have 9 harmonics shown in the spectrum with odd harmonics being relatively stronger than the even harmonics, which are barely noticeable. This is mainly attributed to the hysteresis nonlinearity exciting the odd harmonics more than the even ones. It can be seen that the first harmonic (the fundamental) has magnitude of less than 5.5 nm and the rest of harmonics have smaller magnitudes.

Another set of experiments are conducted using van der Pol oscillator output used as the desired reference input to the system. In Figure 2.9, the measured output displacement $y(t)$ is shown for the case with the frequency of 100 Hz. In Figure 2.10, we demonstrate the tracking error $e(t)$. Similar to the sawtooth reference case, it can be noticed that the tracking error converges within around 0.003 seconds. However, the tracking error magnitudes are a little bit more compared to the sawtooth reference case. This can be seen clearly in Figure 2.11, in which we demonstrate the spectrum content of the tracking error frequency. It can be seen that the fundamental harmonic has magnitude of 14 nm as compared to less than 5.5 nm in the sawtooth reference case. We can see in Figure 2.11 that we have 9 harmonics in the signal spectrum similar to the sawtooth reference, but with higher amplitudes.

Table 2.1: Percentage mean tracking error (mean $|e(t)|\%$) with respect to the reference maximum peak under sinusoidal reference input for the proposed controller versus comparable methods.

freq. (Hz)	SMC	SHSC	MHSC	EHGO-DI	PI	Inv-B ACS
5	0.0595	0.3245	0.1355	0.0672	0.0736	0.0016
25	0.3100	0.3535	0.1340	0.0665	0.0939	0.0041
50	0.3300	0.3850	0.1420	0.0686	0.1498	0.0101
100	0.4150	0.4075	0.1760	0.1026	0.2897	0.0148

Finally, in Table 2.3, we offer a comparison in absolute percentage tracking errors for the cases of the sawtooth and van der Pol references'. It can be observed from the table that for all the tested frequencies, the van der Pol reference case has higher tracking errors as compared to the sawtooth case. For instance, in the 100 Hz frequency case, we can see that absolute percentage

Table 2.2: Peak mean tracking error (max $|e(t)|\%$) with respect to the reference maximum peak under sinusoidal reference input for the proposed controller versus comparable methods.

freq. (Hz)	SMC	SHSC	MHSC	EHGO-DI	PI	Inv-B ACS
5	0.4750	0.8600	0.4495	0.1153	0.7894	0.0083
25	0.8500	0.9250	0.4405	0.1383	0.8422	0.0212
50	1.1250	0.9650	0.5050	0.1821	1.0058	0.0465
100	1.3750	1.1900	0.7850	0.3333	1.5185	0.0610

Table 2.3: Percentage Tracking errors for the proposed controller with respect to the reference maximum peak under sawtooth and van der Pol desired references.

freq. (Hz)	Sawtooth		van der Pol	
	Mean $|e(t)|\%$	Max $|e(t)|\%$	Mean $|e(t)|\%$	Max $|e(t)|\%$
5	0.0016	0.0133	0.0017	0.0210
25	0.0054	0.0481	0.0075	0.0560
50	0.0104	0.1027	0.0202	0.1291
100	0.0226	0.2584	0.0707	0.3695

mean error of the van der Pol reference case is larger by more than three times compared to the sawtooth reference case. This is an indication that the van der Pol reference excites strongly the odd harmonics as compared to the previous two references.

It is worth mentioning that we tried replacing the switching function designed based on the analytical error bound by a constant gain taken as the maximum of the switching function $\beta_w(\cdot)$ for $t \geq 0$. However, the results obtained from the fixed switching gain have shown that the tracking errors have increased with more aggressive control actions for all the considered references.

Remark 2.2.

- *In the implementation of the adaptive servocompensator (2.45), to avoid the case when the matrix S has very large eigenvalues, we utilized the technique suggested in [53] to scale down the internal model matrices such that $A_{\vartheta} = g_{\vartheta}\bar{A}_{\vartheta}$ and $B_{\vartheta} = g_{\vartheta}\bar{B}_{\vartheta}$, where $\bar{A}_{\vartheta}$ is chosen as a Hurwitz matrix with eigenvalues (-1,-1.5,-2) and the pair $(\bar{A}_{\vartheta}, \bar{B}_{\vartheta})$ is in controllable canonical form, g_{ϑ} is the scaling factor and is chosen to be $2\pi \times 600$. This technique helps in making the adaptation parameters in K_{ϑ} reasonably small.*

- *In the adaptation law (2.47), We added the function $\left(\mu_{\vartheta} sat \left(\hat{\xi}_c / \mu_{\vartheta} \right) \right)$ due to the benefit seen in the experimental implementation of the controller for enhancing the adaptation performance; however, in the original approach of [70], it is not mandatory. It's worth mentioning that this modification has not changed the final theoretical outcomes.*

- *In the controller evaluation, we have limited the desired reference frequency to maximum of 100 Hz. This is mainly to avoid causing excessive vibration, which could lead to potential damage of the device, especially, when the highest harmonic frequency is very close to the first resonant frequency of the system.*

Chapter 3

Inversion-free Hysteresis Compensation Via Adaptive Conditional Servomechanism

3.1   Introduction

In this chapter, we propose an inversion-free approach to the control of systems with hysteresis, removing the computational complexity in constructing an inverse compensator. The hysteresis nonlinearity is modeled as a Modified Prandtl-Ishlinskii (MPI) operator. We utilize the properties of the MPI hysteresis model to transform the system into a semi-affine form, where one term has the control input appearing linearly and the other term represents the hysteretic perturbation. The proposed controller is designed based on an adaptive conditional servocompensator approach, which is a continuously-implemented sliding mode control law powered with an adaptive servocompensator. An analytical bound on the hysteretic perturbation is derived and used in the design of the sliding mode control law. A low-pass filter is augmented with the control law, to avoid solving a complicated equation involved. Our stability analysis shows that, under reasonable assumptions, the boundedness of the closed-loop system trajectories is ensured.

The rest of the chapter is organized as follows. In Section 3.2, the system dynamics with MPI operator is described, the transformation into a semi-affine form is presented, and the derivation of hysteretic bound is explained. Section 3.3 details the design of the adaptive conditional compen-

sator. Analysis of the output-feedback closed-loop system is carried out in Section 3.4. Finally, in Section 3.5, we present the experimental validation of the proposed controller.

3.2   System Model

Consider the following dynamics, which are represented as a linear system preceded with a hysteresis nonlinearity modeled by an MPI operator:

$$
\begin{cases}
\dot{x}_i & = \; x_{i+1} \quad 1 \leq i \leq n-1 \\
\dot{x}_n & = \; f(x) + b\upsilon(t) \\
y & = \; x_1
\end{cases}
\tag{3.1}
$$

where $x \in \mathcal{R}^n$ is the state vector, y is the output, the function $f(x) = -a_1 x_1 - \cdots - a_{n-1} x_{n-1} - a_n x_n$, a_i and b are model parameters, $b > 0$, and $\upsilon \in \mathcal{R}$ is the output of the hysteresis nonlinearity modeled as follows:

$$
\upsilon(t) = \Gamma_{hd}[u; \upsilon_0](t) = \theta_d^T \Pi_d \left[\theta_h^T \Pi_h[u; \upsilon_0](t) \right](t)
\tag{3.2}
$$

where u is the system input, Γ_{hd}, Π_d, and Π_h represent the MPI, the asymmetric dead-zone operator, and the classical PI operator, respectively, $\theta_d^T = [\theta_{d_1}, \theta_{d_2}, \dots, \theta_{d_p}]^T$ is the dead-zone operator's weight vector, $\theta_h^T = [\theta_{h_0}, \theta_{h_1}, \dots, \theta_{h_q}]^T$ represents the PI operator's weights vector, υ_0 represents the initial state of the hysteresis, and $(\cdot)^T$ represents the transpose. As shown in Eq. (3.2) above, the MPI operator consists of the PI operator and the dead-zone operator [32]. The PI operator is modeled as a sum of weighted backlash operators (also known as play operators), each of which is

represented as:

$$v_{h_i}(t) = \pi_{h_i}\left[u, v_{h0_i}\right](t)$$
$$= \max\left(\min\left(u + r_i, v_{h0_i}\right), u - r_i\right) \tag{3.3}$$

for $i \in [0, q]$, where v_{h_i} is the output of the ith backlash operator and r_i is the corresponding threshold. Let $r = [r_0, r_1, \ldots, r_q]^T$, with $0 = r_0 \leq r_1 \leq \cdots \leq r_q$. The PI operator is defined as

$$v_h(t) = \theta_h^T \Pi_h[u; v_{h0}](t) = \sum_{i=0}^{q} \theta_{h_i} \pi_{h_i}[u; v_{h0}](t) \tag{3.4}$$

The asymmetric dead-zone operator is a weighted sum of asymmetric dead-zone functions. The output of each asymmetric dead-zone function under the input $v_h(t)$ can be represented as

$$v_{d_i}(t) = \pi_{d_i}(v_h) = \begin{cases} v_h(t) - \overline{d}_i, & v_h(t) \geq \overline{d}_i \\ 0, & \underline{d}_i < v_h(t) < \overline{d}_i \\ v_h(t) - \underline{d}_i, & v_h(t) \leq \underline{d}_i \end{cases} \tag{3.5}$$

where $\overline{d}_i$ and $\underline{d}_i$ are respectively the corresponding positive and negative thresholds for $i \in [1, p]$ and π_{d_i} is the ith asymmetric dead-zone nonlinearity. Notice that the use of asymmetric dead-zone functions is a modification from the original model of [32], where one-sided dead-zone functions are used. We had to do this modification, which will reduce the ability of the MPI operator to represent the asymmetric hysteresis behavior, because of some difficulty in establishing the stability of the closed-loop system later. Accordingly, the dead-zone operator is defined as

$$v_d(t) = \theta_d^T \Pi_d[v_h(t)] = \sum_{i=1}^{p} \theta_{d_i} \pi_{d_i}(v_h)$$

where $\Pi_d^T = [\pi_{d_1}, \dots, \pi_{d_p}]^T$. Let $\underline{d}^T = [-\underline{d}_1, \dots, -\underline{d}_p]^T$ and $\overline{d}^T = [\overline{d}_1, \dots, \overline{d}_p]^T$.

The tracking error is defined as

$$e_1 = y - y_r \tag{3.6}$$

where y_r is the desired reference, which is assumed to satisfy the following condition.

Assumption 3.1. *The reference signal $y_r(t)$ and its derivatives up to $y_r^{(n)}(t)$ are piecewise continuous in t and are bounded for all $t \geq 0$.*

Shifting the system dynamics using (3.6), the error dynamics are found to be

$$\begin{aligned} \dot{e}_i &= e_{i+1} & 1 \leq i \leq n-1 \\ \dot{e}_n &= f(e) + \Delta_{ref}(t) + b\upsilon(t) \end{aligned} \tag{3.7}$$

where $e \in \mathcal{R}^n$ is the vector of error states, $e = (e_1, \cdots, e_n)^T$, $f(e) = -a_1 e_1 - \cdots - a_{n-1} e_{n-1} - a_n e_n$, and $\Delta_{ref}(t) = -a_1 y_r - a_2 \dot{y}_r - \cdots - a_{n-1} y_r^{(n-1)} - a_n y_r^{(n)}$.

3.2.1 Transformation into The Semi-Affine form

Both the system model (3.1) and the error model (3.7) are non-affine due to the hysteresis non-linearity at the input. In the subsequent steps, we will utilize the properties of the MPI hysteresis model to transform the error model into a semi-affine form, where the input nonlinearity is partitioned into two parts; the first part is linear, while the second part consists of a nominal hysteretic nonlinearity modeled as a classical PI operator and a hysteretic perturbation.

Assumption 3.2. *The uncertainties of the MPI operator (3.2) are limited only to the PI operator's vector θ_h, and the dead-zone operator's weight vector θ_d, which are represented as*

$$\theta_h = \theta_h^N + \Delta_h \tag{3.8}$$

$$\theta_d = \theta_d^N + \Delta_d \tag{3.9}$$

where θ_h^N and θ_d^N are the nominal weight vectors for the PI operator and the dead-zone operator, respectively, while Δ_h and Δ_d represent the respective uncertainties of the two operators.

Proposition 3.1. *Under Assumption 3.2, the MPI operator (3.2) can be rewritten in the following semi-affine form*

$$\upsilon(t) = \Theta_d^N \theta_{h_0}^N u + \Theta_d^N Q_{h-0}(t) + \varphi_\Delta(t) \tag{3.10}$$

where $\theta_{h_0}^N$ is the corresponding weight of the backlash operator π_{h_0}, $\Theta_d^N = \theta_d^{N\,T} 1 = \sum_{i=1}^p \theta_{d_i}^N$, 1 is a column vector with all of its entries are equal to 1, and $Q_{h-0}(t)$ is the output of the nominal hysteresis nonlinearity modeled the the classical PI operator with the term π_{h_0} excluded, and φ_Δ is a hysteretic perturbation term.

Proof: Based on Assumption 3.2, by substituting (3.8) and (3.9) into Eq. (3.2), one obtains

$$\upsilon(t) = (\theta_d^{N\,T} + \Delta_d^T) \Pi_d \left[(\theta_h^{N\,T} + \Delta_h^T) \Pi_h [u; \upsilon_o](t) \right](t) \tag{3.11}$$

Using the fact that the asymmetric dead-zone nonlinearity can be represented by an asymmetric saturation nonlinearity [87], we write

$$\pi_{d_i}[Q] = Q - \sigma_{d_i}(Q) \tag{3.12}$$

where

$$\sigma_{d_i}(Q) = \begin{cases} \overline{d}_i & \text{if } Q > \overline{d}_i \\ Q & \overline{d}_i \le Q \le \underline{d}_i \\ \underline{d}_i & Q < \underline{d}_i \end{cases}$$

Let

$$Q_h(t) \overset{def}{=} \theta_h^{N\ T} \Pi_h [u; v_0](t) \tag{3.13}$$

$$Q_\Delta(t) \overset{def}{=} \Delta_h^T \Pi_h [u; v_0](t) \tag{3.14}$$

With Eqs. (3.13) and (3.14), Eq. (3.11) can be rewritten as

$$v(t) = (\theta_d^{N\ T} + \Delta_d^T)\Pi_d [Q_h + Q_\Delta](t) \tag{3.15}$$

which, based on (3.12), can be expressed as

$$v(t) = (\theta_d^{N\ T} + \Delta_d^T)[1(Q_h + Q_\Delta) - \sigma_d(Q_h + Q_\Delta)] \tag{3.16}$$

where $\sigma_d = [\sigma_{d_1}, \ldots, \sigma_{d_p}]^T$. Accordingly, we can rewrite (3.16) as

$$v(t) = \varphi_N(t) + \varphi_\Delta(t) \tag{3.17}$$

where

$$\varphi_N(t) = \Theta_d^N Q_h(t) \tag{3.18}$$

is the nominal part of the input hysteresis nonlinearity and $\Theta_d^N = \sum_{i=1}^p \theta_{d_i}^N$. Notice here that the nominal input nonlinearity is modeled with a classical PI operator. Other hysteretic perturbation components are lumped in the term $\varphi_\Delta(t)$ as follows:

$$\varphi_\Delta(t) = \theta_d^{N\ T} 1\ Q_\Delta(t) + \Delta_d^T 1\ Q_h(t) + \Delta_d^T 1\ Q_\Delta(t) - (\theta_d^{N\ T} + \Delta_d^T)\ \sigma_d(Q_h(t) + Q_\Delta(t))$$

where the term $\varphi_\Delta(t)$ will be treated as a matched disturbance input. By separating the backlash

operator with $r_0 = 0$ (namely, the non-hysteretic term) from the rest of backlashes in the nominal

term φ_N in (3.18), one gets

$$Q_h(t) = \theta_{h_o}^N u + Q_{h-0}(t)$$

where

$$Q_{h-0}(t) = \theta_{h-0}^{N\ T} \Pi_{h-0}[u; v_0](t)$$

and $\theta_{h-0}^N = \left[\theta_{h_1}^N, \theta_{h_2}^N, \ldots, \theta_{h_q}^N\right]^T$ is the vector of nominal weights for the PI operator excluding the

(trivial) backlash with zero threshold term. Consequently, the nominal term of the input nonlinear-

ity is expressed as

$$\varphi_N(t) = \Theta_d^N \theta_{h_o}^N u(t) + \Theta_d^N Q_{h-0}(t) \tag{3.19}$$

Using (3.17) and (3.19), we get (3.10). $\qquad\qquad\square$

Accordingly, the error dynamics (3.7) can be transformed from a non-affine form to a semi-

affine form as follows

$$\begin{cases} \dot{e}_i = e_{i+1} & 1 \leq i \leq n-1 \\ \\ \dot{e}_n = f(e) + \Delta_{ref}(t) + b_h u(t) + b_d\, Q_{h-0}(t) \\ \\ \qquad + b\, \varphi_\Delta(t) \end{cases} \tag{3.20}$$

where $b_h = b\, \Theta_d^N \theta_{h_o}^N$ is assumed to have a nonzero value and $b_d = b\, \Theta_d^N$.

The error dynamics (3.20) will be used in the subsequent sections for the controller design,

observer design, and closed-loop analysis purposes. We can further derive a bound on the hysteretic

perturbation term ϕ_Δ.

Proposition 3.2. *If Assumption 3.2 holds, then the hysteretic perturbation term $\varphi_\Delta(t)$ in Proposi-*

tion 3.1 is bounded by

$$|\varphi_\Delta(t)| \le K_o|u| + K_1 \tag{3.21}$$

where

$$K_o = \Delta_{max}\left[\|\theta_d^N\|_\infty + \|\theta_h^N\|_\infty + \Delta_{max}\right] \tag{3.22}$$

$$K_1 = K_o\|r\|_\infty + p\left[\|\theta_d^N\|_\infty + \|\Delta_d\|_\infty\right]\sigma_{dmax} \tag{3.23}$$

$$\Delta_{max} = p(q+1)\max\left(\|\Delta_h\|_\infty, \|\Delta_d\|_\infty\right) \tag{3.24}$$

where $\|\cdot\|_\infty$ is the infinity norm, which is the maximum of the absolute values of the vector entries and $\sigma_{dmax} = \max\left(\|\underline{d}\|_\infty, \|\overline{d}\|_\infty\right)$.

Proof: The backlash operator (3.3) can be represented using a stop operator in the following way [80]:

$$\pi_{s_i}[u; \upsilon_0](t) = u(t) - \pi_{h_i}\left[u; \upsilon_{h_{0i}}\right](t)$$

Since the stop operator $\pi_{s_i}\left[u; \upsilon_{h_{0i}}\right](t)$ satisfies the inequality

$$\left|\pi_{s_i}\left[u; \upsilon_{h_{0i}}\right](t)\right| \le r_i \tag{3.25}$$

each play operator $\pi_{h_i}\left[u; \upsilon_{h_{0i}}\right](t)$ is bounded by

$$\left|\pi_{h_i}\left[u; \upsilon_{h_{0i}}\right](t)\right| \le |u(t)| + r_i \tag{3.26}$$

As a result, it can be easily seen that

$$|Q_h(t)| \le (q+1)\|\theta_h^N\|_\infty\left(|u| + \|r\|_\infty\right) \tag{3.27}$$

$$|Q_\Delta(t)| \le (q+1)\|\Delta_h\|_\infty (|u| + \|r\|_\infty) \tag{3.28}$$

By using Hölder's inequality, one can see that

$$|(\theta_d^{N\ T} + \Delta_d^T)\sigma_d (Q_h + Q_\Delta)| \le p \left[\|\theta_d^N\|_\infty + \|\Delta_d\|_\infty \right] \sigma_{dmax} \tag{3.29}$$

Utilizing the bounds (3.27), (3.28), and (3.29), we can derive (3.21). □

3.3 Adaptive Conditional Servocompensator Design

3.3.1 Continuously-Implemented SMC Design

The design of adaptive conditional servocompensator involves first designing a continuously-implemented SMC law [70]. The continuously-implemented SMC is designed by replacing the discontinuous switching function with a saturation or sigmoidal function [88]. Consider the sliding function

$$s_c = k_1 e_1 + k_2 e_2 + \cdots + k_{n-1} e_{n-1} + e_n$$

Its time-derivative is found to be;

$$\dot{s}_c = f(e) + \Delta_{ref}(t) + \Delta_e(e) + b_h\, u + b_d\, Q_{h-0}(t) + b\, \varphi_\Delta(t)$$

where $\Delta_e(e) = k_1 e_2 + \cdots + k_{n-1} e_n$. Let the control input be

$$u = u_{eq} + u_s \tag{3.30}$$

57

where u_{eq} denotes the equivalent control term, while u_s denotes the switching control term. For the control law design purposes, we use the following Lyapunov function candidate:

$$V_s = \frac{1}{2}s_c^2$$

Using the control law (3.30), the time-derivative of V_s will be

$$\dot{V}_s = s_c \dot{s}_c = s_c \left[f(e) + \Delta_{ref}(t) + \Delta_e(e) + b_h u_{eq} + b_h u_s + b_d Q_{h-0}(t) + b\ \varphi_\Delta(t) \right]$$

Note that, to design u_{eq}, we need the existence of a feasible solution to the following equation:

$$f(e) + \Delta_{ref}(t) + \Delta_e(e) + b_h u_{eq} + b_d Q_{h-0}(t) = 0 \qquad (3.31)$$

with respect to u_{eq}. Since the hysteresis operator corresponding to Q_{h-0} does not contain the non-hysteretic backlash and is thus not strictly increasing, it does not admit a unique inverse. Furthermore, due to the implicit nature of (3.31), one cannot obtain a closed-form solution to (3.31) even if the analytical inverse of Q_{h-0} were available. To address this challenge, we propose the use of a low-pass filter which can be expressed as

$$\tau \dot{z}_h + z_h = Q_{h-0}(t) \qquad (3.32)$$

where τ is a design parameter chosen small enough. Now, the equivalent control u_{eq} is designed by using the output of the filter z_h to mitigate the effect of the signal $Q_{h-0}(t)$

$$u_{eq} = \frac{1}{b_h} \left[-f(e) - \Delta_{ref}(t) - \Delta_e(e) - b_d z_h \right] \qquad (3.33)$$

The switching control law is taken as

$$u_s = -\beta_s(t, e, z_h) \operatorname{sat}(s_c/\mu) \qquad (3.34)$$

where $\operatorname{sat}(\cdot)$ represents the saturation function, and $\beta_s(, \cdot, \cdot)$ is the switching-gain function and it will be defined in Theorem 3.1 later. Here $\mu > 0$ is a design parameter that represents the slope of the saturation function, such that $\lim_{\mu \to 0} \operatorname{sat}(s_c/\mu) = \operatorname{sgn}(s_c)$. If μ is chosen small enough (smaller than τ as our analysis will show later), we can guarantee that the trajectory will be attracted in finite time to a small neighborhood around the the surface $s_c = 0$, namely, the boundary layer $\{|s_c| \leq \mu\}$, and will stay confined therein for all the future time. This choice of the switching control law is to avoid the chatter of the control; however, the error e will be $O(\mu)$. To deal with this error we use the adaptive conditional servomechanism [70], which is discussed next.

3.3.2 Adaptive Conditional Servocompensator Design

The control law (3.34) does not achieve zero tracking error because in the boundary-layer layer phase, there is a non-vanishing matched disturbance

$$\chi = \mu b \, \varphi_\Delta(t)$$

which (in theory) generates an infinite number of harmonics of the reference signal frequency. To accommodate the adaptive conditional servomechanism theory [70] and [82], we will consider a finite number of frequencies (the frequencies themselves need not to be known; only their number should be known).

Assumption 3.3. *The approximate disturbance $\bar{\chi}(t)$ is generated by an exogenous neutrally stable*

linear dynamical system:

$$\dot{\omega} = S\omega, \quad \bar{\chi} = \Gamma\omega \tag{3.35}$$

where $\omega \in \varpi$ is the state vector of the approximated exosystem, and $\varpi \subset \mathcal{R}^m$ is a compact set,

$$S = \begin{bmatrix} 0 & 1 & 0 & \dots & 0 \\ 0 & 0 & 1 & \dots & 0 \\ \vdots & & & & \vdots \\ 0 & \dots & \dots & 0 & 1 \\ c_0 & c_1 & \dots & \dots & c_{m-1} \end{bmatrix}_{m \times m}, \Gamma = \begin{bmatrix} 1 & 0 & \dots & \dots & 0 \end{bmatrix}_{1 \times m}$$

The internal model (i.e., the servocompensator) is designed to be active only when the sliding surface trajectory enters the boundary layer in the following way;

$$\dot{\eta} = A_\eta \eta + \mu B_\eta \mathrm{sat}\left(s/\mu\right) \tag{3.36}$$

where $\eta \in \mathcal{R}^m$ is the conditional servocompensator state vector. The matrix A_η is chosen to be Hurwitz, and the pair (A_η, B_η) is in the controllable canonical form. Let s be the new surface variable, which includes the servomechanism,

$$s = K_\eta^T \eta + s_c$$

where K_η is a unique vector that assigns the eigenvalues of $\left(A_\eta + B_\eta K_\eta^T\right)$ at the eigenvalues of S. Because A_η is Hurwitz, if $\eta(0)$ is $O(\mu)$, $\eta(t)$ will be $O(\mu)$. The switching control law (3.34) is modified to

$$u_s = -\beta_s\left(t, e, z_h\right) \mathrm{sat}\left(s/\mu\right) \tag{3.37}$$

In this work, we consider the output feedback case, where only e_1 is available for measurement. Therefore, we utilize a high-gain observer to reconstruct the remaining error states. Similar to [86], we design a high-gain observer with a linear structure:

$$\dot{\hat{e}}_i = \hat{e}_{i+1} + \frac{g_i}{\varepsilon^i} (e_1 - \hat{e}_1) \quad 1 \le i \le n-1$$
$$\dot{\hat{e}}_n = \frac{g_n}{\varepsilon^n} (e_1 - \hat{e}_1)$$

(3.38)

where $\hat{e}_i$ is the estimate of e_i, $\varepsilon \ll 1$ is a positive design parameter, and g_i is the corresponding estimation gain, where all the gains are chosen such that the polynomial $\lambda^n + g_1 \lambda^{n-1} + \cdots + g_{n-1}\lambda + g_n$ is Hurwitz. The control laws (3.33), (3.37), and the conditional compensator dynamics (3.36) are modified by replacing e and s by $\hat{e}$ and $\hat{s}$, respectively, where

$$\hat{s} = K_\eta^T \eta + \hat{s}_c$$

(3.39)

It is worth mentioning that in order to prevent the observer peaking, the estimated observer states are saturated before being fed into the control law, which makes the control law globally bounded in its arguments in the domain of interest. The work of [84] ensures the existence and uniqueness of the solution M of the following Sylvester equation $MS - SM = -P^{-1}B_\eta \left(\Gamma + K_\eta^T PM \right)$, if A_η and S have no common eigenvalues. Moreover, the matrix M is non-singular because the pair (A_η, B_η) is controllable and the pair (S, Γ) is observable [84]. Note that here P is a unique non-singular similarity transformation matrix such that

$$P^{-1} \left(A_\eta + B_\eta K_\eta^T \right) P = S, \quad P^{-1}B_\eta = [0\ 0\ \ldots\ 0\ 1]^T$$

(3.40)

Now, suppose that the frequencies of the approximated disturbance signal $\bar{\chi}$ are unknown, which

means that the eigenvalues of the exosystem (3.35) are unknown. An adaptation mechanism is implemented by replacing K_η in (3.39) by $\hat{K}_\eta$, and then an adaptive law is designed to adjust the eigenvalues of the matrix $\left(A_\eta + B_\eta \hat{K}_\eta^T\right)$ online to become equal to the eigenvalues of the exosystem matrix S. In case of having a partial adaptation, we define the following ι-dimensional vectors

$$\lambda_\eta = Z_\eta K_\eta \quad \text{and} \quad v = Z_\eta \eta$$

where $\iota \leq m$ is the number of the adapted variables, Z_η is $(\iota \times m)$ matrix with its rows are unit vectors, and v represents the regressor vector. Since the pair (A_η, B_η) is chosen to be in the controllable canonical form, it can be seen that the number of adaptation variables ι will be $m/2$ if the number of frequencies is even, or $(m-1)/2$ if the number of frequencies is odd. Suppose that λ_η belongs to the convex hypercube $\varpi_\eta = \{\lambda_\eta | a_i \leq \lambda_{\eta_i} \leq b_i, 1 \leq i \leq \iota\}$. As we will show later in Section 3.4.2, the adaptation law can be designed as

$$\dot{\hat{\lambda}}_\eta = \mathcal{B}(\hat{s}, \mu) \ \mathcal{P}(\gamma(\hat{s}_c, v, \beta_s)) \tag{3.41}$$

where the function $\mathcal{P}(\cdot)$ is a parameter projection operator that retains $\hat{\lambda}_\eta$ in ϖ_δ for all $t \geq 0$. Moreover, define the set $\varpi_\delta = \{\lambda_\eta | a_i - \delta \leq \lambda_{\eta_i} \leq b_i + \delta, 1 \leq i \leq \iota\}$, and $\delta > 0$. The function γ is defined as

$$\gamma(\hat{s}_c, v, \beta_s) = g_a \beta_s v \ Pr(\hat{s}_c) / \mu^2$$

where g_a is the adaptation gain. The componentwise smooth projection $\mathcal{P}(\gamma(\hat{s}_c, v, \beta_s))$ is defined

by

$$
\left[\mathcal{P}\left(\gamma\left(\hat{s}_c, v, \beta_s\right)\right)\right]_i = \begin{cases} \left(1 + \frac{b_i - \hat{\lambda}_{\eta_i}}{\delta}\right)\gamma_i & \text{if } \hat{\lambda}_{\eta_i} > b_i \text{ and } \gamma_i > 0 \\ \left(1 + \frac{\hat{\lambda}_{\eta_i} - a_i}{\delta}\right)\gamma_i & \text{if } \hat{\lambda}_{\eta_i} < a_i \text{ and } \gamma_i < 0 \\ \gamma_i & \text{Otherwise} \end{cases}
$$

The function $Pr(\hat{s}_c) = \mu_\eta \operatorname{sat}\left(\hat{s}_c / \mu_\eta\right)$ is added as an additional optional step that we find later beneficial in the controller implementation, where $0 < \mu_\eta < \mu$. The above projection ensures that $\hat{\lambda}_\eta \in \varpi_\eta$. The function $\mathcal{B}(s, \mu)$ is defined as

$$
\mathcal{B}(s, \mu) = \begin{cases} 0 & \text{if } |s| \geq 2\mu \\ 1 & \text{if } |s| \leq \mu \\ 1 - \frac{|s| - \mu}{\mu} & \text{if } \mu < |s| < 2\mu \end{cases}
$$

The purpose of the function $\mathcal{B}(\hat{s}, \mu)$ is to keep $\hat{\lambda}_\eta$ constant outside the boundary set $\{|s| \leq 2\mu\}$.

3.4 Analysis of Output-Feedback Closed-loop System

3.4.1 Reaching Phase

In this phase, the closed-loop system under output feedback consists of the exosystem dynamics (3.35), the conditional servomechanism (3.36), the semi-affine error dynamics (3.20), and the high-gain observer dynamics (3.38). By introducing the change of variables $\tilde{z}_h = z_h - Q_{h-o}(t)$, the shifted filter dynamics equation is obtained, and by considering the sliding surface function (3.39) under output feedback, we can obtain the following three time-scale singularly perturbed closed-

loop system;

$$
\begin{cases}
\dot{\omega} = S\omega \\[1em]
\dot{\eta} = A_\eta \eta + \mu B_\eta \operatorname{sat}\left((s - N(\varepsilon)\,\varphi)/\mu\right) \\[1em]
\dot{\zeta} = A_\zeta \zeta + B_\zeta \left(s - \hat{K}_\eta^T \eta\right) \\[1em]
\dot{s} = -b_d \tilde{z}_h + \Delta_1(\cdot) + \Delta_2(\cdot) - b_h . \psi(\eta, \hat{e}, z_h, \mu) + \psi_z(\cdot) \\[1em]
\tau \dot{\tilde{z}}_h = -\tilde{z}_h - \tau \Delta_q(\cdot) + \psi_q(\cdot) \\[1em]
\varepsilon\,\dot{\varphi} = A_\varphi \varphi + \varepsilon\,B_\varphi \left[-b_d \tilde{z}_h - \Delta_e(e) + \Delta_2(\cdot)\right. \\[0.6em]
\qquad\qquad \left. -b_h . \psi(\eta, \hat{e}, z_h, \mu) + \psi_z(\cdot)\right] \\[1em]
\dot{\hat{\lambda}}_\eta = \mathcal{B}(\hat{s}, \mu) . \mathcal{P}(\gamma(\hat{s}_c, v, \beta_s))
\end{cases}
\tag{3.42}
$$

where the matrices A_ζ and A_φ are Hurwitz. Furthermore, the pairs $\left(A_\zeta, B_\zeta\right)$ and $\left(A_\varphi, B_\varphi\right)$ are in controllable and observable canonical forms, respectively. The scaled estimation dynamics are given by

$$
\varphi_i = \frac{1}{\varepsilon^{n-i}}(e_i - \hat{e}_i)
$$

Notice here if $\varphi = 0$, the closed-loop equations will coincide with the corresponding equations under state-feedback. The terms

$$
\Delta_1(\cdot) = \hat{K}_\eta^T A_\eta \eta + \mu \hat{K}_\eta B_\eta \operatorname{sat}\left((s - N(\varepsilon)\varphi)/\mu\right) + \dot{\hat{\lambda}}_\eta v
$$

$$
\Delta_2(\cdot) = b\varphi_\Delta(t)
$$

$$
\psi_z(\cdot) = b_d \psi_q(\cdot) + b\left(\hat{\varphi}_\Delta(t) - \varphi_\Delta(t)\right)
$$

$$
\psi_q(\cdot) = \hat{Q}_{h-o}(t) - Q_{h-o}(t)
$$

$$\Delta_q(\cdot) = \frac{\partial Q_{h-o}}{\partial u}\left(\dot{u}_{eq} + \dot{u}_s\right)$$

$$\zeta^T = [e_1 \ e_2 \ \dots \ e_{n-1}]$$

$$\varphi^T = [\varphi_1 \ \varphi_2 \ \dots \ \varphi_n]$$

$$N(\varepsilon) = \left[k_1\varepsilon^{n-1} \ k_2\varepsilon^{n-2} \ k_3\varepsilon^{n-3} \ \dots \ k_{n-1}\varepsilon \ 1\right]$$

where $\hat{\varphi}_\Delta$ and $\hat{Q}_{h-o}$ are the corresponding terms under the output-feedback case. Finally,

$$\psi(\eta, e, z_h, \mu) = \beta_s(t, e, z_h)\operatorname{sat}(s/\mu)$$

Since the matrices A_η, A_ζ, and A_φ are Hurwitz, we define the following Lyapunov functions;

$$V_\eta \overset{def}{=} \eta^T P_\eta \eta, \quad V_\zeta \overset{def}{=} \zeta^T P_\zeta \zeta, \quad V_\varphi \overset{def}{=} \varphi^T P_\varphi \varphi,$$

$$V_s \overset{def}{=} \frac{1}{2}s^2, \quad \text{and} \quad V_q \overset{def}{=} \frac{1}{2}\tilde{z}_h^2$$

where the symmetric positive definite matrices P_η, P_ζ, and P_φ are the solutions of the following Lyapunov equations: $P_\eta A_\eta + A_\eta^T P_\eta = -I$, and $P_\zeta A_\zeta + A_\zeta^T P_\zeta = -I$, $P_\varphi A_\varphi + A_\varphi^T P_\varphi = -I$. respectively. Given any positive constants $c > \mu$ and $r > \tau$, we define the following compact sets:

$\Omega_c \overset{def}{=} \{(\zeta, s) : V_\zeta \leq \rho_\zeta c^2, |s| \leq c\}, \Omega_\mu \overset{def}{=} \{(\zeta, s) : V_\zeta \leq \rho_\zeta \mu^2, |s| \leq \mu\}, \Omega_\eta \overset{def}{=} \{\eta : V_\eta \leq \rho_\eta \mu^2\},$

$\Sigma_r \overset{def}{=} \{\tilde{z}_h : V_q \leq \rho_q r^2\}, \Psi_\tau \overset{def}{=} \{\tilde{z}_h : V_q \leq \rho_q \tau^2\}$, and $\Psi_\varepsilon \overset{def}{=} \{\varphi : V_\varphi \leq \rho_\varphi \varepsilon^2\}$, where the param-

eters ρ_ζ, ρ_η, ρ_q, and ρ_φ will be defined in the proof of Theorem 3.1.

Theorem 3.1. *Suppose that Assumptions (3.1)-(3.3) hold and consider the closed-loop system (3.42). Let Ω_1, Ω_2 be compact sets and be in the interior of Ω_c and Σ_r, respectively, $\eta(0) \in \Omega_\eta$,*

65

and let υ_o and $\hat{\zeta}(0)$ be bounded. Let the switching-gain function $\beta_s(t,e,z_h)$ be chosen as

$$\beta_s(t,e,z_h) = \frac{K_1 + K_o|u_{eq}|}{\Theta_d^N \theta_{ho}^N (1 - \bar{K}_o)} + \gamma_o \tag{3.43}$$

with $\bar{K}_o = \left(K_o / \left(\Theta_d^N \theta_{ho}^N\right)\right)$ and $\gamma_o > 0$. Assume $\bar{K}_o < 1$. Then there is $\tau^* > 0$, such that for each $\tau \in (0, \tau^*]$, there is $\mu^* = \mu^*(\tau) > 0$, such that for each $\mu \in (0, \mu^*]$, there is $\varepsilon^* = \varepsilon^*(\tau, \mu) > 0$, such that for every $\tau \in (0, \tau^*]$, $\mu \in (0, \mu^*]$, and $\varepsilon \in (0, \varepsilon^*]$ and for all initial conditions $(\zeta(0), s(0)) \in \Omega_1$, $\tilde{z}_h(0) \in \Omega_2$, $\eta(0) = O(\mu)$, and $\hat{\lambda}_\eta \in \varpi_\eta$, all the state variables are bounded and converge to a positively-invariant set $\Upsilon_{\tau,\mu,\varepsilon} = \Psi_\tau \times \Omega_\mu \times \Psi_\varepsilon$ in finite time.

The proof of this theorem is deferred to Appendix A.2.

3.4.2   Boundary Layer Phase

In this section, we will analyze the closed-loop system stability after the trajectory enters the set $\Upsilon_{\tau,\mu,\varepsilon}$. Inside this set, the function $\text{sat}\left((s - N(\varepsilon)\varphi)/\mu\right) = s - N(\varepsilon)\varphi/\mu$. We introduce the following change of variables;

$$\vartheta = \frac{(\eta - \bar{\eta})}{\mu} + B_\eta \varsigma \tag{3.44}$$

where

$$\varsigma = \int_0^{e_n} \frac{dy}{b_h \beta_s(t, e_1, \ldots, e_{n-1}, y, z_h)}$$

and $\bar{\eta}$ is the conditional servocompensator state in the boundary-layer phase under the case when the internal model is not perturbed (Eq. (3.35) of Assumption 3.3). Under the internal-model-perturbation-free case, the switching control law u_s uses a fixed-gain $\bar{\beta}_{smax}$ instead of the variable

gain function $\beta_s(t,\hat{e},z_h)$, where $\bar{\beta}_{smax}$ is a positive constant such that inside the set $\Upsilon_{\tau,\mu,\varepsilon}$, the switching-gain satisfies $|\beta_s(t,\hat{e},z_h)| \leq \bar{\beta}_{smax}$, and consequently, $\bar{\chi} = -\bar{\beta}_{smax}\dfrac{K_\eta^T\bar{\eta}}{\mu}$. The main reason of this modification is because the switching function $\beta_s(t,\hat{e},z_h)$ is not smooth. Therefore, the change of variables (3.44) cannot be used to obtain the dynamics $\dot{\vartheta}$. In the forthcoming equations, we rewrite the term

$$\hat{K}_\eta^T\eta = K_\eta^T\eta + \tilde{\lambda}_\eta^T v \tag{3.45}$$

where $\tilde{\lambda}_\eta = \hat{\lambda}_\eta - \lambda_\eta$. Accordingly, using the equations (3.44)-(3.45), the closed-loop dynamics can be written in four time-scales as follows;

$$\begin{cases}
\dot{\omega} = S_o\omega \\[2mm]
\dot{\vartheta} = A_\eta\vartheta + F_\vartheta(\zeta,\tilde{z}_h,s_c) + b_\vartheta(\varphi)/\mu + \Delta_\vartheta(\bar{\eta},\zeta,z_h,\bar{\chi},\tilde{\chi},\mu) \\[2mm]
\dot{\zeta} = A_\zeta\zeta + B_\zeta s_c \\[2mm]
\tau\dot{\tilde{z}}_h = -\tilde{z}_h - \tau\Delta_q(\cdot) + \psi_q(\cdot) \\[2mm]
\mu\,\dot{s}_c = -b_h\beta_s(t,\hat{e},z_h)s_c - b_h\beta_s(t,\hat{e},z_h)\tilde{\lambda}_\eta^T v + \mu F_{sc}(\vartheta,\zeta,\tilde{z}_h,s_c) \\[2mm]
\qquad\quad + b_{sc}(\varphi) + \mu\Delta_{sc}(\bar{\eta},\zeta,z_h,\bar{\chi},\tilde{\chi},\mu) + \mu\psi_z(\cdot) \\[2mm]
\varepsilon\,\dot{\varphi} = A_\varphi\varphi + \varepsilon B_\varphi\big[-b_h\beta_s(t,\hat{e},z_h)s_c/\mu - b_h\beta_s(t,\hat{e},z_h)\tilde{\lambda}_\eta^T v/\mu \\[2mm]
\qquad\quad + F_{sc}(\vartheta,\zeta,\tilde{z}_h,s_c) + b_{sc}(\varphi)/\mu + \Delta_{sc}(\bar{\eta},\zeta,z_h,\bar{\chi},\tilde{\chi},\mu) + \psi_z(\cdot)\big] \\[2mm]
\dot{\tilde{\lambda}}_\eta = \gamma\beta_s(t,\hat{e},z_h)H.v.s_c/\mu^2 + F_\lambda(\vartheta,\varphi)/\mu^2
\end{cases} \tag{3.46}$$

where the functions b_ϑ, b_{sc}, F_ϑ, F_{sc}, and F_λ are locally Lipschitz functions and satisfy

$$b_\vartheta(0) = b_{sc}(0) = F_\vartheta(0,0,0) = F_{sc}(0,0,0,0) = F_\lambda(0,0) = 0$$

The internal model perturbation term

$$\tilde{\chi}\left(\bar{\eta}, e, \mu\right) = b\ \left(\varphi_\Delta\left(u\right) - \bar{\chi}\right)$$

is generated due to the effect of the approximation of the internal model. The $\imath \times \imath$ matrix H is a diagonal matrix, whose entries could be 1, $1 + \dfrac{b_i - \hat{\lambda}\eta_i}{\delta}$, or $1 + \dfrac{\hat{\lambda}\eta_i - a_i}{\delta}$.

Remark 3.1. *Inside the set $\Upsilon_{\mu,\tau}$, the following arguments are applied:*

1. *From the analysis of Section 3.4.1, the control law (3.30) is bounded due to the boundedness of its arguments and because of the smooth projection of the adaptation law (3.41), which implies the boundedness of the term $\varphi_\Delta\left(u\right)$. Moreover, $\bar{\eta}$ is of order of μ, therefore it can be easily shown that*

$$\left|\tilde{\chi}\left(\bar{\eta}, e, \mu\right)\right| \leq \delta_h$$

where δ_h is a positive constant dependent on μ. Consequently, we can show that

$$\left|\Delta_\vartheta\left(\cdot\right)\right| \leq \delta_{\vartheta_o}, \quad and \quad \left|\Delta_{sc}\left(\cdot\right)\right| \leq \delta_{sc_o} \tag{3.47}$$

Moreover, the following terms are found to satisfy the following inequalities;

$$\left|\dot{u}_{eq}\right| \leq \bar{k}_{eq}, \quad \left|\dfrac{\partial Q_{h-o}}{\partial u}\right| \leq \bar{k}_q, \quad and \quad \left|\dot{\beta}_s\left(t, \hat{e}, z_h\right)\right| \leq \bar{k}_s$$

where $\bar{k}_s = \dfrac{K_o.\bar{k}_{eq}}{\Theta_d^N \theta_{h_0}^N \left(1 - \bar{K}_o\right)}$. Therefore, we can show that

$$\left|\dot{u}_s\right| \leq \dfrac{\bar{k}_s}{\mu}$$

Consequently, the term

$$|\Delta_q(\cdot)| \leq \delta_z$$

where $\delta_z = \bar{k}_q \left(\bar{k}_{eq} + \frac{\bar{k}_s}{\mu} \right)$.

2. *By the local Lipschitz properties, the following inequalities are satisfied*

$$|\frac{1}{b_h} \psi_z(\cdot)| \leq \bar{l}_z|\varphi\|, \quad and \quad |\psi_q(\cdot)| \leq \bar{l}_q|\varphi\| \tag{3.48}$$

where $\bar{l}_z$ and $\bar{l}_q$ are positive constants.

Let $\bar{v} = Z_\eta \bar{\eta}$ be the regressor vector inside the set $\Upsilon_{\mu,\tau}$. if $\bar{v}$ is not persistently excited (i.e. Z_η is not of full rank), the next lemma, which is adapted from [70], is needed.

Lemma 3.1. *For every initial condition $\omega(0)$, there exists a non-singular matrix E_η, which is dependent on $\omega(0)$, such that*

$$E_\eta \bar{v} = \begin{bmatrix} \bar{v}_a \\ 0 \end{bmatrix}, \tag{3.49}$$

where $\bar{v}_a \in \mathcal{R}^{\iota_a}$ is the persistently exciting vector with $\iota_a \leq \iota$. Under the fully persistently exciting case ($\iota = \iota_a$), E_η will be equal to the identity matrix and $\bar{v} = \bar{v}_a$. If $\bar{v} = 0$, equation (3.49) holds with $\bar{v}_a = 0$.

Theorem 3.2. *Consider the closed-loop dynamics (3.46). Under the assumptions of Theorem 3.1, and inside the set $\Upsilon_{\tau,\mu,\varepsilon}$, if the regressor vector of the conditional servocompensator state $\bar{v}$ is persistently exciting, then there exists $\tau^\star > 0$, such that for each $\tau \in (0, \tau^\star]$, there is $\mu^\star = \mu^\star(\tau) > 0$, such that for each $\mu \in (0, \mu^\star]$, there is $\varepsilon^\star = \varepsilon^\star(\tau, \mu) > 0$, such that, for every $\tau \in (0, \tau^\star]$, $\mu \in (0, \mu^\star]$, and $\varepsilon \in (0, \varepsilon^\star]$,*

- *For the internal-model-perturbation-free case ($\tilde{\chi} = 0$): if τ is chosen arbitrarily small, then for $\bar{\lambda} = max\left(\tau, \frac{\tau}{\mu}\right)$, the tracking error $e(t) = O(\bar{\lambda})$.*

- *For the internal-model-perturbation case ($|\tilde{\chi}| \leq \delta_h$): there exists $\delta_h^\star$ such that for every $\delta_h \in (0, \delta_h^\star]$, the tracking error will be $O(\delta_h)$.*

The proof of the theorem is provided in Appendix A.3.

3.5   Application to Nanopositioning Control

In this section, the proposed control approach and the theoretical results are confirmed by conducting a series of tracking experiments with different types of reference inputs. For that purpose, we use the experimental setup shown in Figure 2.5. The nanopositioner dynamics are modeled in the form of equation (3.1) with $n = 2$. The parameters of the fast dynamics part of the model are identified using a sinusoidal input with a small amplitude with frequency range from 1 Hz to 5 KHz. Accordingly, the parameters of the fast dynamics are identified as $a_1 = 1.838 \times 10^8$, $a_2 = 4622$, and $b = 1.0688 \times 10^9$. The measured Bode plot of the nanopositioner system output is shown in Figure 3.1 along with that of the identified system dynamics. The slow dynamics part, which is represented by the MPI hysteresis operator, is identified by injecting a sinusoidal input with gradually decreased amplitude to exhibit the inner loops. The identified MPI model is constructed with 8 play operators and 9 deadzone elements, and the identified weights and thresholds vectors are found to be

$$\begin{aligned}
\theta_h^T &= [0.001, 0.7301, 0.1293, 0.0969, 0.0695, 0.0324, 0.0329, 0.0871], \\
r^T &= [0, 0.0460, 0.4654, 1.1071, 1.8248, 2.5574, 5.0429, 3.4279],
\end{aligned}$$

$$\theta_d^T = \left[-14.775, -8.287, -1.1174, -0.9753, -0.9403, 0.3892, 0.4419, \right.$$
$$\left. 14.2164, 19.1489 \right],$$
$$\underline{d}^T = [-7.4049, 0, -8, -5, -7, -10, -9, -2, -1],$$
$$\overline{d}^T = [1.4344, 0, 5.3450, 4.0961, 2.6166, 9.3856, 7.4485, 1.4278, 0.4928],$$

To validate the overall model, we cascade the MPI hysteresis model with the fast dynamics transfer function. Notice that the fast dynamics transfer function has a non-unity dc gain. Since we model the slow dynamics using the MPI operator model, the fast dynamics transfer function dc gain is changed to unity when the model is implemented. In Figures 3.2, we show the system output versus the overall identified system output using the same input reference used for identification. While in Figure 3.3, we plot the measured hysteresis loops as compared to the predicted ones. As it can be seen in both figures, the identified system can capture the system output with small prediction error. Moreover, we repeat the same experiment by changing the frequency of the input signal with a range up to 100 Hz, and as expected the prediction error increased as we increased the frequency of the input; however, the identified model is still able to capture the output of the system reasonably well.

To reconstruct the unmeasured states, the high-gain observer (3.38) is implemented with the parameters ε, the gains g_1 and g_2 being 0.0001, 3 and 20, respectively. The low-pass filter (3.32) is implemented with $\tau = 2000$. The parameters of the switching function β_s (Eq. (3.43)) are calculated after calculating the bound (3.21). We calculate $\sigma_{dmax} = 10$ and, with $\bar{K}_o = 0.97$, then the parameter K_1 is found to be 217.5. For the switching control part, the following parameters are used: $\mu = 1000$ and $k_1 = 5000$. The parameter γ_o is chosen as 10.

The conditional servocompensator dynamics (3.36) is designed as a third-order system. This is based on the assumption that the frequency spectrum of the boundary-layer disturbance (χ)

includes only the fundamental frequency of the reference input. In Addition to that, an integral state is augmented with the second-order internal model dynamics to compensate for any disturbance bias.

To robustify the adaptation law against noisy inputs, the adaptation parameter λ_η is assumed to be confined to the following convex set;

$$\varpi_\eta = \{\lambda_\eta | -8 \leq \lambda_\eta \leq 8\}$$

The adaptation gain γ, the parameters δ, and μ_η are chosen as 2.7×10^4, 0.1, and 1, respectively.

The experiments are focused on three types of reference signals. The first signal is a sinusoidal input defined as $y_r = 10 \sin(2\pi f t) + 10$ μm with frequency $f = 5$, 25, 50, and 100 Hz. Notice that the controller evaluation is limited to reference frequencies with range up to 100 Hz, to avoid excessive vibration and potential damage to the nanopostioner when the highest harmonic frequency is getting close to the first resonant frequency of the system. In Table 3.1 and 3.2, we show a comparative analysis for the tracking error of our proposed approach with experimental results of different control approaches taken from previous projects on the same device. The considered approaches for comparison are: 1) the work of [48] in which a sliding mode controller (SMC) was designed, 2) the results of the Single Harmonic Servo-Compensator (SHSC) and Multi-Harmonic Servo-Compensator (MHSC) demonstrated in [5], 3) a classical PI controller implemented and tuned to best possible performance without utilizing any feedforward inversion. The percentage of the maximum tracking error with respect to the maximum peak is shown in Table 3.1, while in Table 3.2 the percentage of the mean tracking error with respect to the maximum peak is presented. In both tables, it can be seen that the inversion-free adaptive conditional servocompensator based approach (Inv-F ACS) results are superior to the other four approaches in reducing the tracking

72

error very significantly.

We further test the controller by using a sawtooth reference input with frequencies 5, 25, 50, and 100 Hz. To avoid spiking responses of the closed-loop system, we insert a second order pre-filter to smooth out the signal edges. In Figure 3.4, the measured displacement of the inversion-free control schema under the 100 Hz frequency reference case is shown. The tracking error is shown in Figure 3.5 for the period 0-0.03 second. It can be noticed in both Figure 3.4 and 3.5 that the tracking error undershoots to around -3.5 μm and then overshoot to less than 1 μm before converging quickly in less than 0.005 seconds. The tracking error of the inversion-free controller in the boundary-layer phase (0.01-10 seconds) are shown in Figure 3.6. Notice that the tracking error are not increasing in this period.

Another set of experiments are conducted with a periodic reference generated by the van der Pol oscillator with the same frequency ranges used with the previous two reference inputs. See Figures 3.7, 3.8, and 3.9 for the tracking performance for the 100 Hz case.

Table 3.1: Percentage Peak tracking error (max $|e(t)|\%$) for the proposed controller versus other controllers in percent of the reference maximum peak under sinusoidal reference input.

Hz	SMC	SHSC	MHSC	PI	Inv-F ACS
5	0.4750	0.8600	0.4495	0.7894	0.0105
25	0.8500	0.9250	0.4405	0.8422	0.0165
50	1.1250	0.9650	0.5050	1.0058	0.0272
100	1.3750	1.1900	0.7850	1.5185	0.0414

Table 3.2: Percentage Mean tracking error (mean $|e(t)|\%$) for the proposed controller versus competing methods in percent of the reference maximum peak under sinusoidal reference input.

Hz	SMC	SHSC	MHSC	PI	Inv-F ACS
5	0.0595	0.3245	0.1355	0.0736	0.0007
25	0.3100	0.3535	0.1340	0.0939	0.0021
50	0.3300	0.3850	0.1420	0.1498	0.0039
100	0.4150	0.4075	0.1760	0.2897	0.0082

To give a further insight, the frequency content spectrum of the tracking error for both cases

Table 3.3: Percentage Tracking errors for the proposed controller in percent of the reference maximum peak under sawtooth and van der Pol reference inputs.

Hz	Sawtooth		van der Pol	
	Max $|e(t)|\%$	**Mean $|e(t)|\%$**	**Max $|e(t)|\%$**	**Mean $|e(t)|\%$**
5	0.0070	0.0007	0.0071	0.0005
25	0.0292	0.0030	0.0195	0.0024
50	0.0414	0.0053	0.0281	0.0045
100	0.1529	0.0111	0.1157	0.0100

of the sawtooth and the van der Pole reference inputs with 100 Hz frequency are given in Figures 3.10 and 3.11, respectively. Two observations can be drawn. Firstly, the harmonics excited for the sawtooth case include 4 odd harmonics, while in the van der Pol case we have 5 odd harmonics. Secondly, it is noted in the sawtooth case that most of the residual error comes from the first and third harmonic, while in the van der Pol case, most of the residual error comes from the third harmonic as compared to the first harmonic amplitude, which is reduced to less than 1 nm. In Table 3.3, the percentage tracking errors are presented for both the sawtooth and the van der Pol cases for the considered frequency range. The results show that the van der Pol case shows slightly better performance than the sawtooth case for all frequencies.

Remark 3.2. *It can be noticed that the controller parameters μ, τ, and k_1 are chosen relatively large. This is mainly attributed to the large parameters of the nanopositioner system's model. This can be explained by appropriately scaling the state and time variables of the semi-affine error dynamics (3.20). Let $a_1 = \omega_n^2$ and $a_2 = 2\xi\omega_n$, where ω_n is the nanpositioner's natural frequency and ξ is the damping coefficient. To scale the system, we apply the following change of variables:*

$$z_1(t_s) = e_1(t), \qquad z_2(t_s) = \frac{e_2(t)}{\omega_n}, \qquad t_s = \omega_n t$$

74

which transforms the error system (3.20) into

$$\begin{cases} \dot{z}_1 = z_2 \\ \dot{z}_2 = -z_1 - 2\xi z_2 + \dfrac{b_h}{\omega_n^2}u + \dfrac{1}{\omega_n^2}\left[\Delta_{ref} + b_d + Q_{h-0} + b\ \varphi_\Delta\right] \end{cases}$$

where $\dot{z}_i$ denotes the derivative of z_i with respect to t_s. The switching component of the continuously-implemented sliding mode control law (3.34) for the transformed system is given by

$$sat\left(\frac{\bar{k}_1 z_1 + z_2}{\bar{\mu}}\right) = sat\left(\frac{\bar{k}_1 e_1 + e_2/\omega_n}{\bar{\mu}}\right) \tag{3.50}$$

where $\bar{\mu}$ is a small parameter. Comparing the switching component of (3.50) with

$$sat\left(\frac{k_1 e_1 + e_2}{\mu}\right)$$

in our controller, we can see that

$$k_1 = \bar{k}_1 \omega_n, \qquad \mu = \bar{\mu}\,\omega_n$$

In other words, the non-scaled surface function s_c will be of order of $\omega_n = 1.3557 \times 10^4$, which was observed in the experiments. Inside the boundary layer, we have

$$\dot{e}_1 = -k_1 e_1 + s_c$$

and $|s_c| \le \mu$. Let $V_{e_1} = \frac{1}{2}e_1^2$. Then the time-derivative of V_{e_1} satisfies

$$\dot{V}_{e_1} = -k_1 e_1^2 + e_1 s_c \le -k_1 e_1^2 + |e_1|\mu \le -\frac{k_1}{2}e_1^2, \quad \forall\,|e_1| \ge \frac{2\mu}{k_1}$$

Therefore, the trajectory reaches the set $\{|e_1| \le \frac{2\mu}{k_1}, |s_c| \le \mu\}$ in finite time. Hence $e_1 = O(\mu/k_1) =$ $O(0.2)$. Adding the conditional adaptation will make the error much smaller. Our theory requires choosing $\tau > \mu$, so we picked $\tau = 2000$.
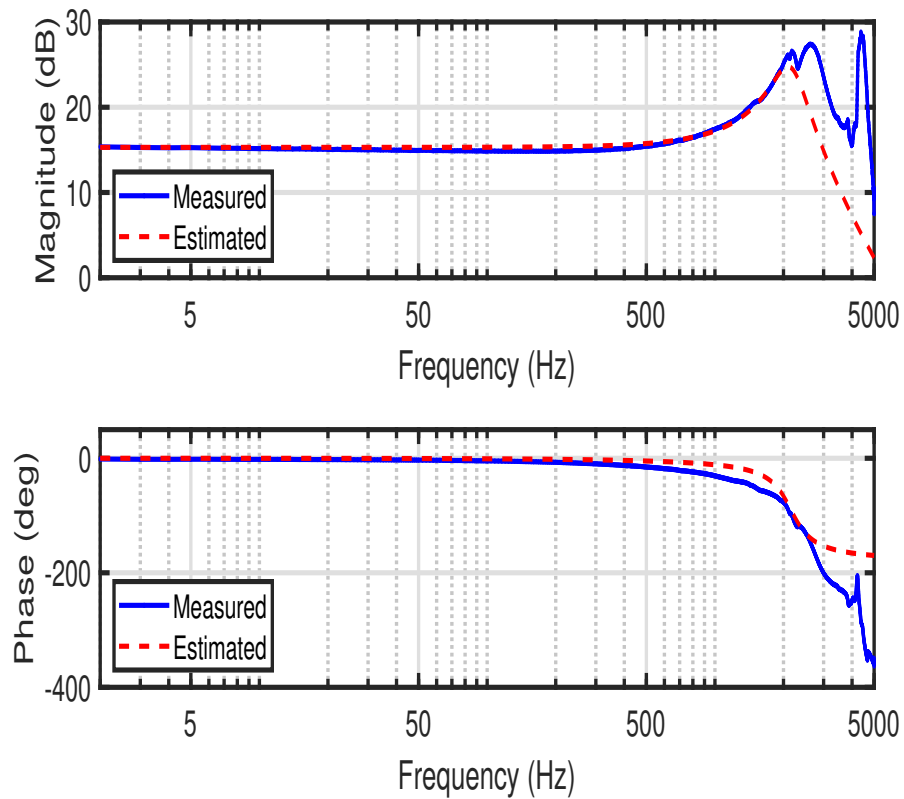
Figure 3.1: Measured Bode plot of the nanopositioner system (in blue) and the output of the identified high-frequency dynamics (in red).
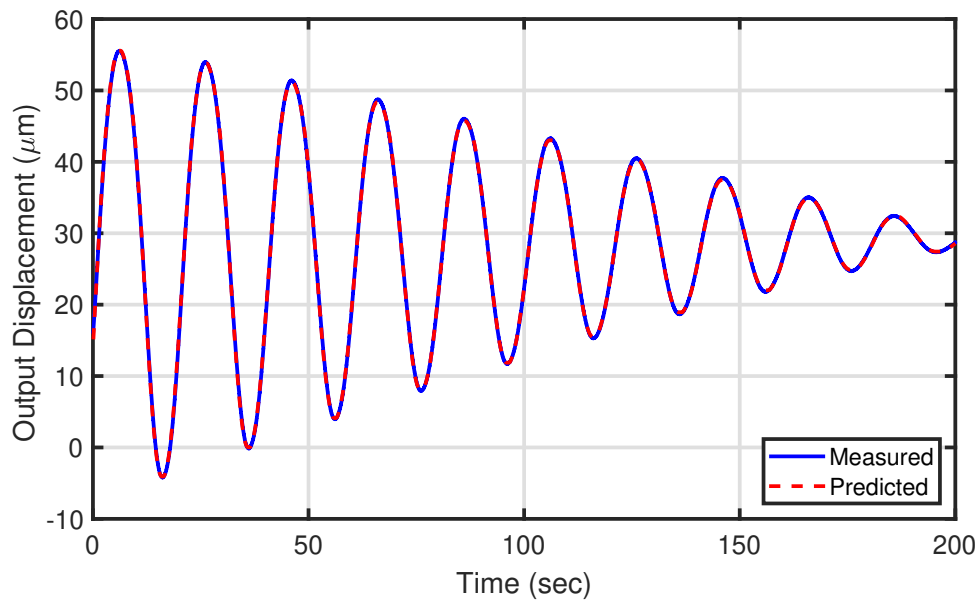
Figure 3.2: Nanopositioner system output used in the identification and the resulting model output.
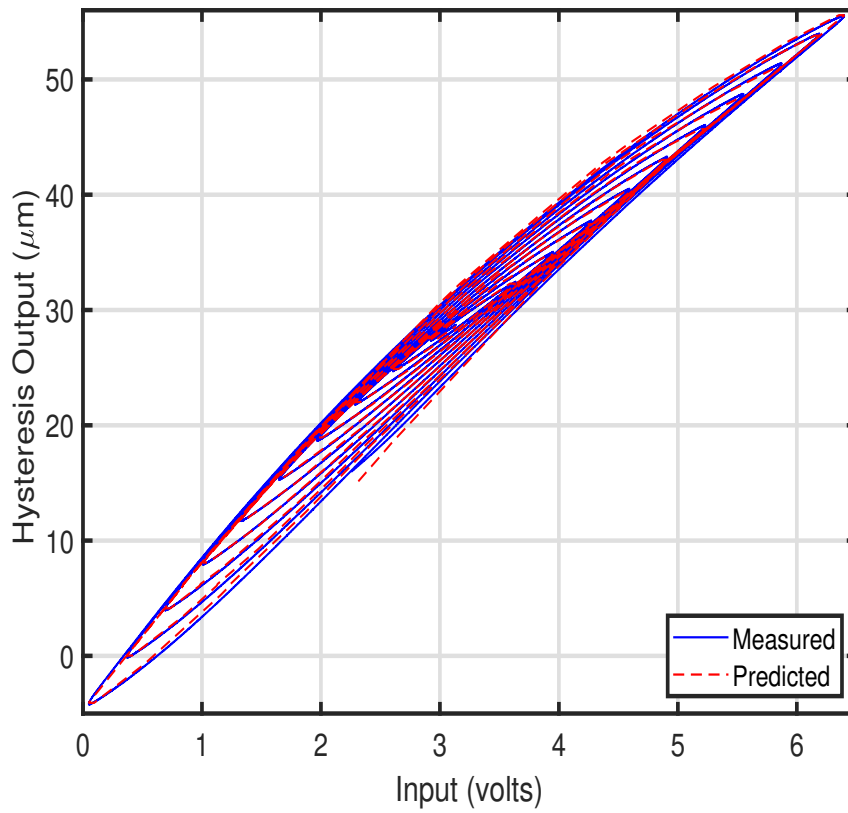
Figure 3.3: Measured hysteresis loops (in blue) compared to predicted hysteresis loops (in red).

77
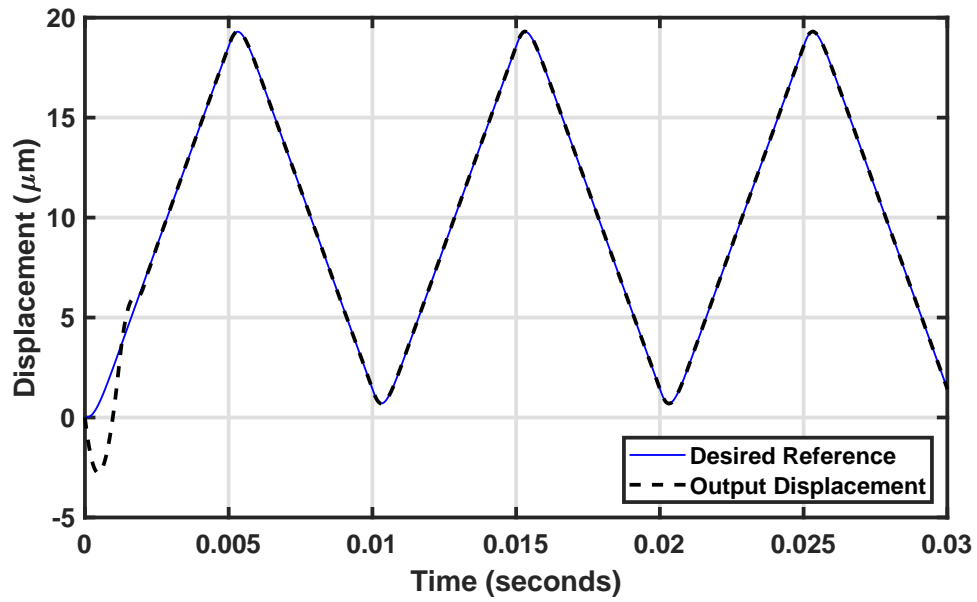
Figure 3.4: Experimental results of measured displacement on tracking a sawtooth reference with 100 Hz frequency using the inversion-free ACS.
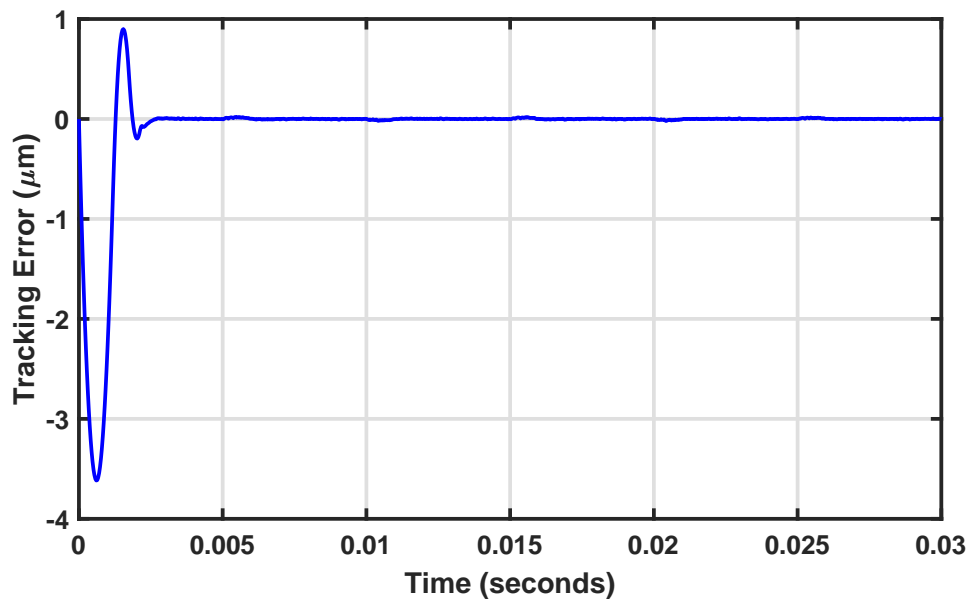
Figure 3.5: Experimental results of the tracking error with a sawtooth reference with 100 Hz frequency.
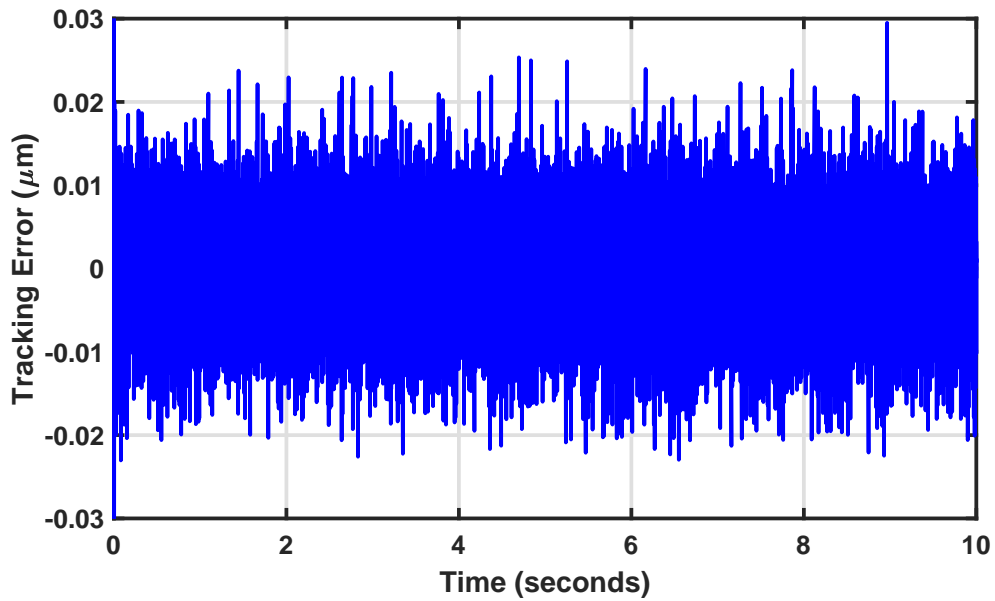
Figure 3.6: Experimental results of the tracking error with a 100 Hz sawtooth reference in the boundary-layer phase.
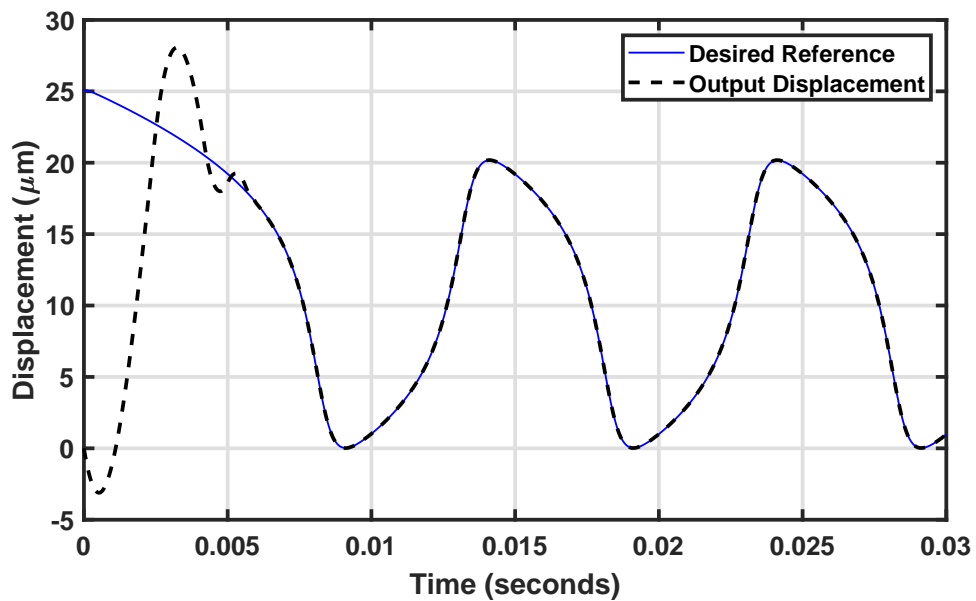
Figure 3.7: Experimental results of measured displacement on tracking a van der Pol reference with 100 Hz frequency using the inversion-free ACS.
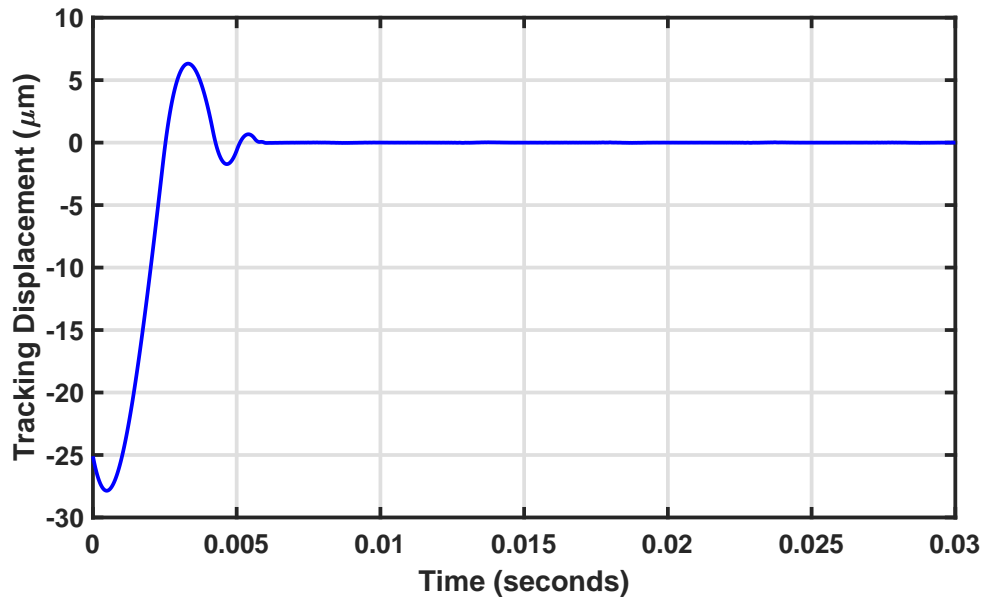
Figure 3.8: Experimental results of the tracking error with a van der Pol reference with 100 Hz frequency.
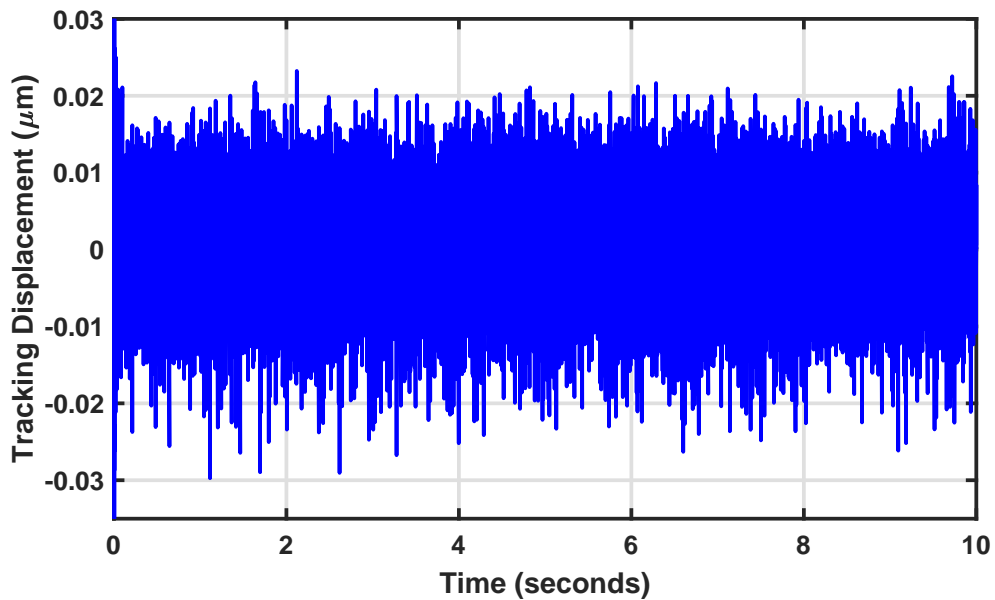
Figure 3.9: Experimental results of the tracking error with a 100 Hz van der Pol reference in the boundary-layer phase.
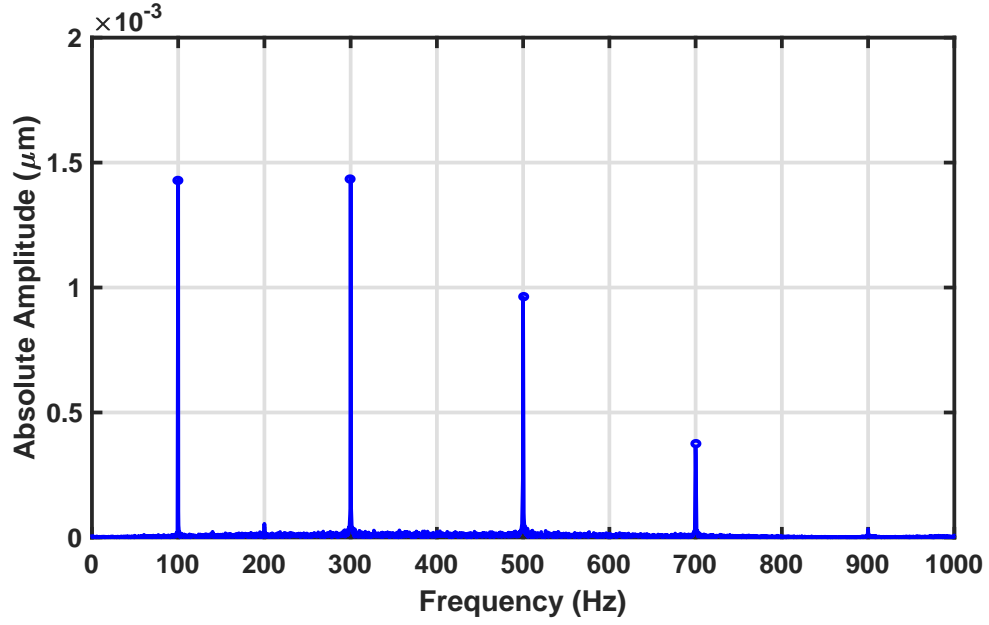
Figure 3.10: Tracking error signal frequency spectrum with a sawtooth reference with 100 Hz frequency in boundary-layer phase.
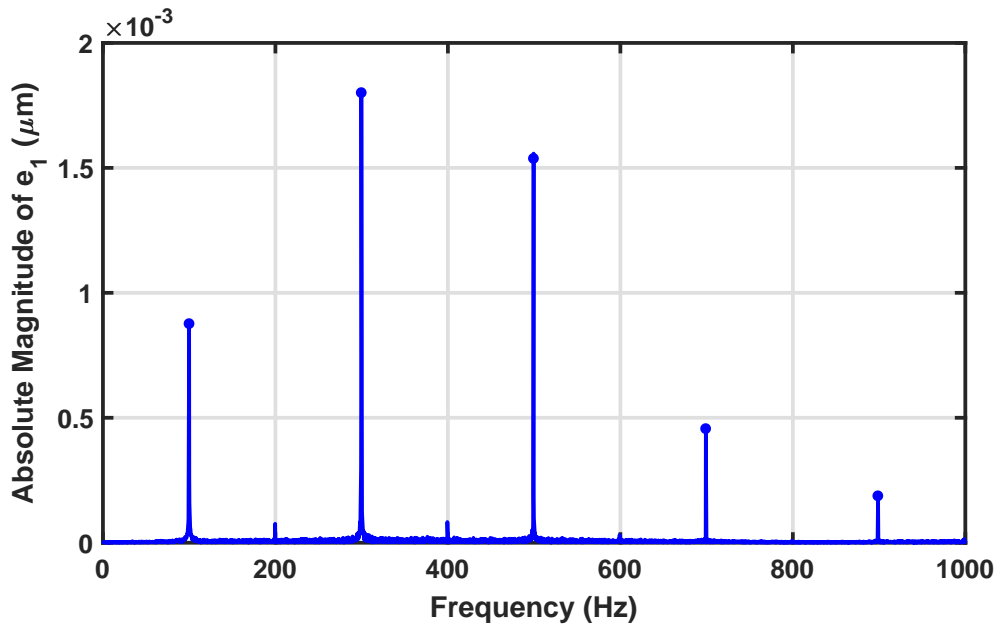
Figure 3.11: Tracking error signal frequency spectrum with a van der Pol reference with 100 Hz frequency in boundary-layer phase using the inversion-free ACS.

Chapter 4

Dynamic Inversion-based Hysteresis Compensation Using Extended High-gain Observer

4.1 Introduction

In this chapter, we consider the tracking problem for an uncertain nonlinear single-input-single-output system, preceded by an unknown hysteresis operator. With a mild assumption on the non-hysteretic component, the system preceded by hysteresis can be treated as an uncertain non-affine nonlinear system. We then use dynamic-inversion [71], to deal with the nonaffine nonlinearity as it computes the inverse in a fast time-scale compared to the plant dynamics. In order to implement the dynamic inversion algorithm, the knowledge of the right hand side of the last state derivative of the plant is required which includes the hysteretic part, and uncertainties. To overcome this, we use extended high-gain observers [72], to estimate the hysteretic part, system states, and uncertainties in the fastest time-scale. Therefore, the closed-loop system using the output feedback controller results in a three-time-scale structure, where the extended high-gain observer estimates unmeasured states, uncertainties and hysteretic perturbation in the fastest time-scale, the dynamic inversion is used in the intermediate time scale, while the plant dynamics evolves in the slowest

time scale.

The remainder of this chapter is organized as follows. In Section 4.2, we introduce the system class and assumptions regarding the hysteresis operator and the nonlinear plant. We provide Propositions 4.1 and 4.2, which are then used for the analysis of the closed-loop system. In Section 4.3 the state feedback controller design is first described, in preparation for the discussion of the output feedback controller. The analysis of the state feedback case determines the saturation level that will be used in output feedback to deal with the observer peaking. Moreover, the state feedback controller is designed first to shape the transient response of the closed-loop system. The transient response under output feedback is shaped by the performance recovery property, which is achieved by bringing the trajectories under output feedback arbitrarily close to the trajectories under state feedback for sufficiently small observer parameter. In Section 4.4, the output feedback control scheme is described and the resulting closed-loop system is analyzed utilizing the assumptions and propositions from Section 4.2 and the saturation level from Section 4.3. Finally, simulation results are presented in Section 4.5, followed by experimental validation and comparison results in Section 4.6.

4.2   Problem Formulation

We consider the tracking problem for a single-input-single-output system defined in the normal form, with a hysteretic operator at the input side:

$$\dot{\eta} = f_0(\eta, \xi, w), \tag{4.1a}$$

$$\dot{\xi} = A\xi + B[f(\eta, \xi, w) + \Upsilon(t)], \tag{4.1b}$$

$$\Upsilon(t) = \Gamma\left[u(\tau)|_{\tau=0}^{t}, H_0\right](t), \tag{4.1c}$$

$$y = \xi_1, \tag{4.1d}$$

where $A \in \mathbb{R}^{\rho \times \rho}$ and $B \in \mathbb{R}^{\rho \times 1}$ are defined as

$$
A = \begin{bmatrix} 0 & 1 & 0 & \dots & 0 \\ 0 & 0 & 1 & \dots & 0 \\ \vdots & \vdots & \ddots & \ddots & \vdots \\ 0 & 0 & \dots & 0 & 1 \\ 0 & 0 & \dots & \dots & 0 \end{bmatrix}, \quad B = \begin{bmatrix} 0 \\ 0 \\ \vdots \\ 0 \\ 1 \end{bmatrix},
$$

$\eta \in \mathbb{R}^{n-\rho}$, $\xi = \mathrm{col}(\xi_1, \dots, \xi_\rho) \in \mathbb{R}^\rho$ are the state variables, $u \in \mathbb{R}$ is the control input, and $y \in \mathbb{R}$ is the output of the system, $\Gamma[\cdot, \cdot]$ is a hysteresis operator, $\Upsilon \in \mathbb{R}$ is the output of the hysteresis operator, which depends on the history of the input $u(\tau)|_{\tau=0}^{t}$ and the initial internal state H_0 of the operator Γ, $w \in \mathbb{R}^l$ is an exogenous input and ρ is the relative degree of the system. The normal form is defined for $\eta \in D_\eta \subset \mathbb{R}^{n-\rho}$ and $\xi \in D_\xi \subset \mathbb{R}^\rho$ for some domains D_η and D_ξ. The system is required to satisfy the following assumptions.

Assumption 4.1. *For any given t, $w(t)$ and $\dot{w}(t)$ are bounded, and $w(t)$ belongs to a known compact set $W \subset \mathbb{R}^l$.*

Assumption 4.2. *The function f is continuously differentiable with locally Lipschitz derivatives and f_0 is locally Lipschitz for all $(\eta, \xi, w) \in D_\eta \times D_\xi \times W$.*

Assumption 4.3. *There exist a continuously differentiable function $V_0(\eta)$, class $\mathcal{K}_\infty$ functions Ψ_1, Ψ_2, and $\mathcal{K}$ function Ψ_3, such that*

$$
\Psi_1(||\eta||) \leq V_0(\eta) \leq \Psi_2(||\eta||)
$$

$$
\frac{\partial V_0}{\partial \eta} f_0(\eta, \xi, w) \leq 0, \text{ for } ||\eta|| \geq \Psi_3(||\xi|| + ||w||)
$$

for all $(\eta, \xi, w) \in D_\eta \times D_\xi \times W$.

Assumption 4.3 implies that the internal dynamics of the system is regionally input-to-state stable.

Assumption 4.4. *The hysteresis operator Γ can be decomposed as*

$$\Gamma \left[u(\tau)|_{\tau=0}^t, H_0 \right](t) = g(u(t)) + \tilde{\Gamma} \left[u(\tau)|_{\tau=0}^t, H_0 \right](t) \tag{4.3}$$

for some non-hysteretic function $g(\cdot)$ and remaining hysteretic term $\tilde{\Gamma}$, and

(i) $g(\cdot)$ is continuously differentiable and satisfies

$$\beta_1 \le \frac{\mathrm{d}g(u)}{\mathrm{d}u} \le \beta_2 \tag{4.4}$$

where β_1 and β_2 are positive constants with $\beta_2 \ge \beta_1$.

(ii) $\tilde{\Gamma}$ is a monotone hysteresis operator in the sense that

$$0 \le (u_1(t) - u_2(t))(\tilde{\Gamma}[u_1(\tau)|_{\tau=0}^t, H_0](t) - \tilde{\Gamma}[u_2(\tau)|_{\tau=0}^t, H_0](t)) \le k(u_1(t) - u_2(t))^2 \tag{4.5}$$

where $u_1(\tau)|_{\tau=0}^t$ and $u_2(\tau)|_{\tau=0}^t$ are both monotonically increasing (or decreasing) inputs with $u_1(0) = u_2(0)$, and k is a positive constant. In addition, $\tilde{\Gamma}[u(\tau)|_{\tau=0}^t, H_0](t)$ is piecewise continuously differentiable with respect to $u(t)$ for a monotonic function u; i.e., any segment of the hysteresis graph ($\tilde{\Gamma}[u, H_0]$ vs. u) has a piecewise continuous slope function.

Remark 4.1. *Assumption 4.4 is satisfied by a wide class of hysteresis operators, including the classical PI operator, the generalized PI operator, and the Preisach operator. For example, for a classical PI operator with $N+1$ plays, the hysteresis output is given by*

$$\Upsilon(t) = \theta_0 u(t) + \sum_{i=1}^N \theta_i \Gamma_{r_i} \left[u(\tau)|_{\tau=0}^t, H_0 \right](t) \tag{4.6}$$

where θ_i is the weight associated with play Γ_{ri} with threshold r_i, θ_0 is the weight associated with the play with threshold $r_i = 0$ (the memory-less term), and H_0 represents the vector of initial values of all plays. If $\theta_0 > 0$ and $\theta_i \geq 0$ for $i = 1, 2, \ldots, N$, the classical PI model satisfies all conditions in Assumption 4.4. Similarly, a generalized PI model satisfies Assumption 4.4 if the non-hysteretic component satisfies (4) and all generalized plays have non-negative weights.

Remark 4.2. *Assumption 4.4 is also satisfied by Preisach-like operators (where the basic building block is a variant of the Preisach hysteron), such as the Krasnosel'skii-Pokrovskii (KP) operator. This operator has been used for hysteresis modeling, e.g., shape memory alloy (SMA) actuators [23]. The output of a KP model is given by*

$$\Upsilon(t) = g(u) + \Gamma[u(\tau)_{\tau=0}^t, H_0](t)$$

where $g(u)$ satisfies (4) and $\Gamma[\cdot]$ consists of KP hysterons which are the same as that of a play operator, when it is unsaturated, namely, when its output is within the interval (-1, 1).

Proposition 4.1. *Consider a hysteresis operator Γ satisfying Assumption 4.4. Then, for a continuous monotonic input u,*

$$0 \leq \frac{\partial \, \tilde{\Gamma}[u(\tau)|_{\tau=0}^t, H_0](t)}{\partial u(t)} \leq k \tag{4.7}$$

and the derivative exists except possibly for a discrete number of points.

Proof: Without loss of generality, consider a continuous monotonically increasing u. Define u_1, such that $u_1(\tau) = u(\tau)$ for $\tau \in [0,t]$, and $u_1(\tau) = u(t) + \Delta_u(\tau)$ for $\tau > t$, where $\Delta_u(t) = 0$ and $\Delta_u(\tau)$ is a continuous, strictly increasing function for $\tau \geq t$. Define u_2 such that $u_2(\tau) = u(\tau)$ for $\tau \in [0,t]$, and $u_2(\tau) \equiv u(t)$, for $\tau > t$. Pick some $\tau = t_1 > t$. It can be easily verified that

$$\frac{\partial \tilde{\Gamma}[u(\tau)|_{\tau=0}^t, H_0](t)}{\partial u(t)} = \lim_{t_1 \to t} \frac{\Delta_\Gamma(t_1)}{\Delta_u(t_1)} \tag{4.8}$$

86

where

$$\Delta_\Gamma(t_1) \stackrel{\triangle}{=} \tilde{\Gamma}[u_1(\tau)|_{\tau=0}^{t_1}, H_0](t_1) - \tilde{\Gamma}[u_2(\tau)|_{\tau=0}^{t_1}, H_0](t_1) \tag{4.9}$$

Eq. (4.7) then follows by utilizing (5) in (4.8) and (4.9). And the derivative thus defined exists except possibly for a discrete number of points due to the piece-wise continuity of the derivative as assumed in Assumption 4.4. □

Remark 4.3. *From Assumption 4.4, for a monotonic input $u(t)$ we have the piece-wise continuity of the derivative of $\tilde{\Gamma}[u(\tau)|_{\tau=0}^{t}, H_0](t)$ with respect to $u(t)$. Therefore, for any compact time interval, there will be only a finite number of jumps of the derivative of $\tilde{\Gamma}[u(\tau)|_{\tau=0}^{t}, H_0](t)$. Moreover, these jumps will be bounded and this follows from (4.5).*

Remark 4.4. *The classical PI operator satisfies Proposition 4.1, with the hysteretic part given by*

$$\tilde{\Gamma}[u(\tau)|_{\tau=0}^{t}, H_0] = \sum_{i=1}^{N} \theta_i \Gamma_{r_i}\left[u(\tau)|_{\tau=0}^{t}, H_0\right](t)$$

from which we have

$$\frac{\partial \tilde{\Gamma}[u(\tau)|_{\tau=0}^{t}, H_0]}{\partial u(t)} = \sum_{i=1}^{N} \theta_i \frac{\partial}{\partial u(t)} \Gamma_{r_i}\left[u(\tau)|_{\tau=0}^{t}, H_0\right](t)$$

As illustrated in Fig. 4.1, $\frac{\partial}{\partial u(t)} \Gamma_{r_i}\left[u(\tau)|_{\tau=0}^{t}, H_0\right](t) = 0$ or 1 depending on whether $\Gamma_{r_i}\left[u(\tau)|_{\tau=0}^{t}, H_0\right](t)$ is in the play or linear region and is discontinuous only when the operator operates at the intersection of the play and linear regions. Therefore, it follows that

$$0 \leq \frac{\partial \tilde{\Gamma}[u(\tau)|_{\tau=0}^{t}, H_0]}{\partial u(t)} \leq \sum_{i=1}^{N} \theta_i$$
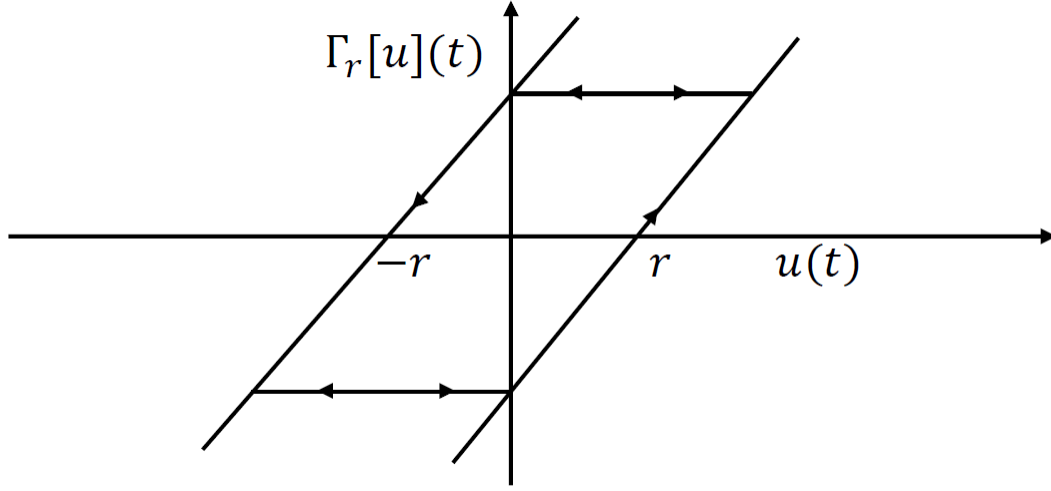
Figure 4.1: Illustration of a classical play operator.

Proposition 4.2. *Consider a hysteresis operator Γ that satisfies Assumption 4.4. Then,*

(i) Γ admits a unique (right) inverse, denoted as Γ^{-1}, in the sense that, $\Gamma \circ \Gamma^{-1} = I$ (identity), i.e., $\Gamma[\Gamma^{-1}[\Upsilon(\tau)|_{\tau=0}^t, H_0^-], H_0](t) = \Upsilon(t)$, for any continuous and monotone function Υ, where H_0^- is the corresponding initial condition of Γ^{-1}.

(ii) The inverse hysteresis operator Γ^{-1} satisfies

$$\frac{1}{\beta_2 + k} \leq \frac{\partial\, \Gamma^{-1}[\Upsilon(\tau)|_{\tau=0}^t, H_0^-](t)}{\partial \Upsilon(t)} \leq \frac{1}{\beta_1} \tag{4.10}$$

Proof: By differentiating $\Gamma[u(\tau)|_{\tau=0}^t, H_0](t)$ with respect to $u(t)$, we have

$$\frac{\partial \Gamma[u(\tau)|_{\tau=0}^t, H_0](t)}{\partial u(t)} = \frac{\partial g(u(t))}{\partial u(t)} + \frac{\partial \tilde{\Gamma}[u(\tau)|_{\tau=0}^t, H_0](t)}{\partial u(t)}$$

and from Eq. (4.4) and Proposition 4.1, we get

$$\beta_1 \leq \frac{\partial\, \Gamma[u(\tau)|_{\tau=0}^t, H_0](t)}{\partial u(t)} \leq \beta_2 + k \tag{4.11}$$

88

For part (i), the existence of a unique inverse is guaranteed by the property that the operator Γ, per Eq. (4.11), is strictly monotonically increasing; namely, the output is strictly increasing (resp., decreasing) with a strictly increasing (resp., decreasing) input.

For Part (ii), Eq. (4.11) shows that the slope of any segment on the hysteresis graph (Υ vs. u) for Γ is bounded between two positive constants, β_1 and $\beta_2 + k$. Since the graph of the inverse operator Γ^{-1} is obtained by swapping the horizontal axis and the vertical axis of the graph for the forward hysteresis operator Γ, one can immediately conclude that the slope of any segment of the inverse hysteresis graph (u vs. Υ) is the reciprocal of the slope of the corresponding segment on the forward hysteresis graph. Eq. (4.10) then follows from (4.11). $\square$

Remark 4.5. *By breaking Υ into piecewise monotone segments, one can easily see that Proposition 4.2 holds for any continuous function Υ.*

Remark 4.6. *Eq. (4.10) shows that the slope of any segment on the hysteresis graph (u vs. Υ) for Γ^{-1} is bounded between two positive constants, $1/(\beta_2 + k)$ and $1/\beta_1$. From Assumption 4.4, since any segment of the hysteresis graph ($\tilde{\Gamma}[u, H_0]$ vs. u) has a piece-wise continuous slope function for a monotonic input u, it follows that for a monotonic input $\Upsilon(t)$, we have the piece-wise continuity of the derivative of the inverse hysteresis operator. Therefore, for any compact time interval, there will be only a finite number of jumps of the derivative of the inverse hysteresis operator. Moreover, these jumps will be bounded and this follows from (4.10).*

Assumption 4.5. *The reference signal $r(t)$ and its derivatives up to $r^{(\rho+1)}(t)$ are bounded for all $t \geq 0$. Moreover, $\mathcal{R}(t) = col(r(t), r^{(1)}(t), \ldots, r^{(\rho-1)}(t)) \in D_\xi$ for all $t \geq 0$.*

The change of variables

$$e_1 = \xi_1 - r(t), \;\; e_2 = \xi_2 - r^{(1)}(t), \; \dots, \; e_\rho = \xi_\rho - r^{(\rho-1)}(t) \tag{4.12}$$

transforms the system (4.1.a-4.1.d) into the form

$$\dot{\eta} = f_0(\eta, e + \mathcal{R}, w), \tag{4.13a}$$

$$\dot{e} = Ae + B\left\{ F\left(\eta, e, \mathcal{R}, w, r^{(\rho)}\right) + \Gamma[u](t) \right\}, \tag{4.13b}$$

$$e_1 = y - r, \tag{4.13c}$$

where $F\left(\eta, e, \mathcal{R}, w, r^{(\rho)}\right) = f(\eta, e + \mathcal{R}, w) - r^{(\rho)}$ and $e = col(e_1, e_2, \dots, e_\rho)$. For ease of notation, we have dropped the initial condition from the hysteresis operator argument, and for simplicity, we write the hysteresis output as $\Gamma[u](t)$. Similarly, we drop t from the definition of the reference signal and its derivatives.

4.3 State Feedback Controller

Dynamic inversion is used for control of nonlinear non-affine-control systems [71]. It is useful for systems where the inverse of the input nonlinearity does not have a closed-form solution. In this chapter the controller u needs to be designed such that the closed-loop system behaves as

$$\dot{e} = (A - BK)e \tag{4.14}$$

where K is chosen such that the matrix $(A - BK)$ is Hurwitz. Let $V_e(e) = e^T Pe$, where P is the solution to the Lyapunov equation $P(A - BK) + (A - BK)^T P = -Q$, for some positive-definite

symmetric matrix Q. Let c be a positive constant and define $\Omega_c = \{e : V_e(e) \leq c\}$. Choose $c > 0$ such that for every $e \in \Omega_c$, $\xi = e + \mathcal{R} \in D_\xi$ and therefore $\{\xi : V_e(e) \leq c\} \subset D_\xi$. Next we define the set $\Omega_0 = \{\eta : V_0(\eta) \leq c_0\}$, which is compact and contained in D_η, where c_0 is chosen such that $c_0 \geq \Psi_2(\Psi_3(\kappa_1(c) + \kappa_2 + \kappa_3))$, where $\kappa_1(c) = \max_{e \in \Omega_c} ||e||$, $\kappa_2 = \max_{w \in W} ||w||$, and $\kappa_3 = \max_t ||\mathcal{R}(t)||$.

From Assumption 4.3, the set $\Omega_0 \times \Omega_c$ is positively invariant with respect to the system

$$\dot{\eta} = f_0(\eta, e + \mathcal{R}, w), \quad \dot{e} = (A - BK)e$$

because on the boundary $\{\eta : V_0(\eta) = c_0\}$

$$\Psi_2(||\eta||) \geq c_0 \geq \Psi_2(\Psi_3(\kappa_1(c) + \kappa_2 + \kappa_3))$$

$$\implies ||\eta|| \geq \Psi_3(\kappa_1(c) + \kappa_2 + \kappa_3)$$

$$\implies ||\eta|| \geq \Psi_3(||\xi|| + ||w||) \implies \dot{V}_0 \leq 0$$

and on the boundary $\{e : V_e(e) = c\}$, $\dot{V}_e < 0$.

In this section we design the state feedback controller and we assume that we have perfect knowledge of the function $f(\cdot)$, states (η, ξ), exogenous input w, the reference signal and its derivatives, and the hysteresis output $\Gamma[u](t)$. The dynamic inversion algorithm is then given by

$$\mu \dot{u} = -\left[F\left(\eta, e, \mathcal{R}, w, r^{(\rho)}\right) + \Gamma[u](t) + Ke \right] \tag{4.15}$$

where μ is a small positive constant. The quasi-steady state is obtained by setting $\mu = 0$,

$$f(\eta, e + \mathcal{R}, w) + \Gamma[u](t) - r^{(\rho)} = -Ke \tag{4.16}$$

From Assumption 4.5, $r^{(\rho)}$ and $r^{(\rho+1)}$ are bounded. Let $d_1 = \max\limits_t |r^{(\rho)}(t)|$ and $d_2 = \max\limits_t |r^{(\rho+1)}(t)|$.

Define the sets $R_0 = \{\mathcal{R} : ||\mathcal{R}|| \leq \kappa_3\}$, $R_1 = \{r^{(\rho)} : |r^{(\rho)}| \leq d_1\}$, and $R_2 = \{r^{(\rho+1)} : |r^{(\rho+1)}| \leq d_2\}$.

From Proposition 4.2, if $(\eta, e, \mathcal{R}, w, r^{(\rho)}) \in \Omega_0 \times \Omega_c \times R_0 \times W \times R_1$ for each $\tau \in [0, t]$, Eq. (16) has a unique solution given by

$$u^*(t) = \phi[\chi](t) \stackrel{\triangle}{=} \Gamma^{-1}\left[\chi(\tau)|^t_{\tau=0}\right](t)$$

where

$$\chi(\tau) = -f(\eta(\tau), e(\tau) + \mathcal{R}(\tau), w(\tau)) + r^{(\rho)}(\tau) - Ke(\tau),$$

and Γ^{-1} is the inverse of the hysteresis operator Γ. Furthermore, from Assumptions 4.1, 4.2, and 4.5, χ is continuously differentiable with respect to t.

The change of variables

$$z(t) = u(t) - \phi[\chi](t)$$

transforms system (4.13.b) and (4.15) into

$$\dot{e} = (A - BK)e + B\{\Gamma[z + \phi] - \Gamma[\phi]\}, \tag{4.17a}$$

$$\mu\dot{z} = -(\Gamma[z + \phi] - \Gamma[\phi]) - \mu\dot{\phi}, \tag{4.17b}$$

where

$$\dot{\phi} = \frac{\partial}{\partial\chi(t)}\left(\Gamma^{-1}\left[\chi(\tau)|^t_{\tau=0}\right]\right)\dot{\chi}(t).$$

Note that $\dot{\chi}(t)$ is bounded for all

$(\eta, e, \mathcal{R}, w, r^{(\rho)}, r^{(\rho+1)}) \in \Omega_0 \times \Omega_c \times R_0 \times W \times R_1 \times R_2$. From Proposition Proposition 4.2, it follows that $\frac{\partial}{\partial\chi(t)}\left(\Gamma^{-1}\left[\chi(\tau)|^t_{\tau=0}\right]\right)$ is bounded for all $(\eta, e, \mathcal{R}, w, r^{(\rho)}) \in \Omega_0 \times \Omega_c \times R_0 \times W \times$

R_1, from which we can conclude that $\dot{\phi}$ is bounded for all $(\eta, e, \mathcal{R}, w, r^{(\rho)}, r^{(\rho+1)}) \in \Omega_0 \times \Omega_c \times R_0 \times W \times R_1 \times R_2$.

The right-hand side of (4.17.b) has a finite number of jumps on any compact time interval and this follows from Proposition 4.2. The solution of (4.17.b) is therefore studied in the sense of Caratheodory solution [89], which is absolutely continuous curves which satisfies

$$z(t) = z(0) + \frac{1}{\mu} \int_0^t E(\tau) d\tau$$

where the integral is the Lebesgue integral and $E(\tau) = -\left(\Gamma[z(\tau) + \phi(\tau)] - \Gamma[\phi(\tau)]\right) - \mu \dot{\phi}(\tau)$.

Let $|u| \leq q_0$, where q_0 is a positive constant, and we define the compact set $\Omega_z = \{z : |z| \leq q\}$, where

$$q \geq q_0 + \max_{(\eta, e, \mathcal{R}, w, r^{(\rho)}) \in \Omega_0 \times \Omega_c \times R_0 \times W \times R_1} |\phi|.$$

Theorem 4.1. *Consider the closed-loop system formed of the plant (4.13) and the dynamic inversion algorithm (4.15). Suppose that Assumptions 4.1-4.5 are satisfied and $(\eta(0), e(0))$ belongs to a known compact subset in the interior of $\Omega_0 \times \Omega_c$, $|z(0)| < q$. Then there exists $\mu^* > 0$ such that for all $\mu \in (0, \mu^*)$, the trajectories of the closed-loop system are bounded for all $t \geq 0$, and*

$$\limsup_{t \to \infty} e(t) = O(\mu), \quad \limsup_{t \to \infty} z(t) = O(\mu). \tag{4.18}$$

Proof: Consider the Lyapunov functions $V_e = e^T P e$ and $V_z = \frac{1}{2} z^2$. Taking the time derivative of V_z along (4.17.b) yields

$$\mu \dot{V}_z = -z \left(\Gamma[z + \phi](t) - \Gamma[\phi](t) \right) - \mu z \dot{\phi}$$

The term $z\left(\Gamma[z+\phi](t) - \Gamma[\phi](t)\right)$ can be written as

$$z\left(\Gamma[z+\phi](t) - \Gamma[\phi](t)\right) = z\left[g(z+\phi) - g(\phi)\right] + z\left[\tilde{\Gamma}[z+\phi](t) - \tilde{\Gamma}[\phi](t)\right]$$

The term $z\left[g(z+\phi) - g(\phi)\right]$ can be written as

$$z\left[g(z+\phi) - g(\phi)\right] = (z+\phi-\phi)(g(z+\phi) - g(\phi)),$$

and from Eq. (4.4), using the mean value theorem [81], we have

$$\beta_1 z^2 \leq (z+\phi-\phi)\left[g(z+\phi) - g(\phi)\right] \leq \beta_2 z^2.$$

From Assumption 4.4, the hysteresis operator $\tilde{\Gamma}[(\cdot)]$ is monotone and

$$z\left[\tilde{\Gamma}[z+\phi](t) - \tilde{\Gamma}[\phi](t)\right] = (z+\phi-\phi)\left[\tilde{\Gamma}[z+\phi](t) - \tilde{\Gamma}[\phi](t)\right]$$

from which we have

$$z\left(\Gamma[z+\phi](t) - \Gamma[\phi](t)\right) \geq \beta_1 z^2$$

Over the compact set $\Omega_0 \times \Omega_c \times R_0 \times W \times R_1 \times R_2$, since $\dot{\phi}$ is bounded, we have $|\dot{\phi}| \leq b$, for some positive constant b independent of μ. Therefore, we have

$$\mu \dot{V}_z \leq -\beta_1 z^2 + \mu |z||\dot{\phi}|$$

$$\implies \dot{V}_z \leq -\frac{\beta_1}{2\mu} z^2, \quad \text{for } |z| \geq \frac{2\mu b}{\beta_1}$$

Take $b_1 = 2b/\beta_1$. There exists $\mu_1 > 0$, such that for all $\mu \in (0, \mu_1)$, the set $\{z : |z| \leq b_1\mu\}$ is

positively invariant, and for sufficiently small μ, the set $\{z : |z| \leq b_1\mu\}$ is in the interior of Ω_z.

Taking the time derivative of V_e along (4.17.a) yields

$$\dot{V}_e = -e^T Q e + 2e^T PB \left(\Gamma \left[z + \phi \right] (t) - \Gamma \left[\phi \right] (t) \right)$$

$$\leq -\lambda_{\min}(Q)||e||^2 + 2\tilde{k}||e|| \cdot ||PB|| \cdot |z|$$

where $\tilde{k} = k + \beta_2$ from (4.3), (4.4) and (4.5), $\lambda_{\max}(Q)$ and $\lambda_{\min}(Q)$ denote the maximum and minimum eigenvalues of the matrix Q, respectively. And for $z \in \{z : |z| \leq b_1\mu\}$, we have

$$\dot{V}_e \leq -\lambda_{\min}(Q)||e||^2 + 2\tilde{k}b_1\mu||PB|| \cdot ||e||$$

$$\leq -\frac{\lambda_{\min}(Q)}{2}||e||^2, \quad \text{for } ||e|| \geq \frac{4\tilde{k}b_1\mu||PB||}{\lambda_{\min}(Q)}$$

Take $b_2 = \dfrac{16\tilde{k}^2 b_1^2 ||PB||^2 \lambda_{\max}(P)}{(\lambda_{\min}(Q))^2}$, from which we have

$$\dot{V}_e \leq -\frac{\lambda_{\min}(Q)}{2}||e||^2, \quad \text{for } V_e \geq b_2\mu^2$$

Therefore, we can choose $\mu_2 > 0$ such that for all $\mu \in (0, \mu_2)$, the set $\{e : V_e \leq b_2\mu^2\}$ is positively invariant and for sufficiently small μ, the set $\{e : V_e \leq b_2\mu^2\}$ is in the interior of $\{e : V_e \leq c\}$, from which we can conclude that the set $\Omega_0 \times \Omega_c \times \Omega_z$ is positively invariant. Finally by taking $\mu^* = \min\{\mu_1, \mu_2\}$, (4.18) follows. $\qquad \square$

Remark 4.7. *Under Assumptions 4.1-4.3, the stability result will be regional. However, if all the assumptions hold globally, i.e. $D_\eta = \mathbb{R}^{n-\rho}$, $D_\xi = \mathbb{R}^\rho$, $W = \mathbb{R}^l$ and $\dot{\eta} = f_0(\eta, \xi, w)$ is input-to-state stable, then the constants c_0 and c, can be chosen arbitrarily large, and any compact set of*

$\mathbb{R}^{n-\rho} \times \mathbb{R}^\rho$ *can be put in the interior of* $\{\eta : V_0(\eta) \le c_0\} \times \{\xi : V_e(e) \le c\}$. *Then, in this case the stability result will be semi-global.*

4.4 Output Feedback Controller

The implementation of the dynamic inversion algorithm in the previous section requires the knowledge of the function $F(\eta, e, \mathcal{R}, w, r^{(\rho)})$ and the hysteresis output $\Gamma[u](t)$, which is typically not available for use in practice. Therefore, we propose an output feedback controller by combining an extended high-gain observer with the dynamic inversion algorithm to compensate for the hysteresis present in the system. High-gain observers are used to robustly estimate the states of a system while extended high-gain observers are used for estimating an unknown input to the system without requiring the input to be slowly varying [72]. Fig. 4.2 illustrates the proposed control approach.

The extended high-gain observer provides an estimate of the combined value at time t for the function F and the hysteresis output Γ, which is then used in the dynamic inversion algorithm. The output feedback controller has two parameters μ and ε, which are small and determine the time scales of the dynamic inversion algorithm and the observer, respectively. Typically the observer dynamics should be faster than the dynamic inversion, so that the estimates can converge to the true values rapidly, and the dynamic inversion should be faster than the plant dynamics so that the control input converges to the desired control quickly.

We set $\sigma(t) = F(\eta(t), e(t), \mathcal{R}, w(t), r^{(\rho)}(t)) + \Gamma[u](t)$. If σ and e were available for feedback, the dynamic inversion algorithm (4.15) would be given by

$$\mu \dot{u} = -[\sigma + Ke]$$
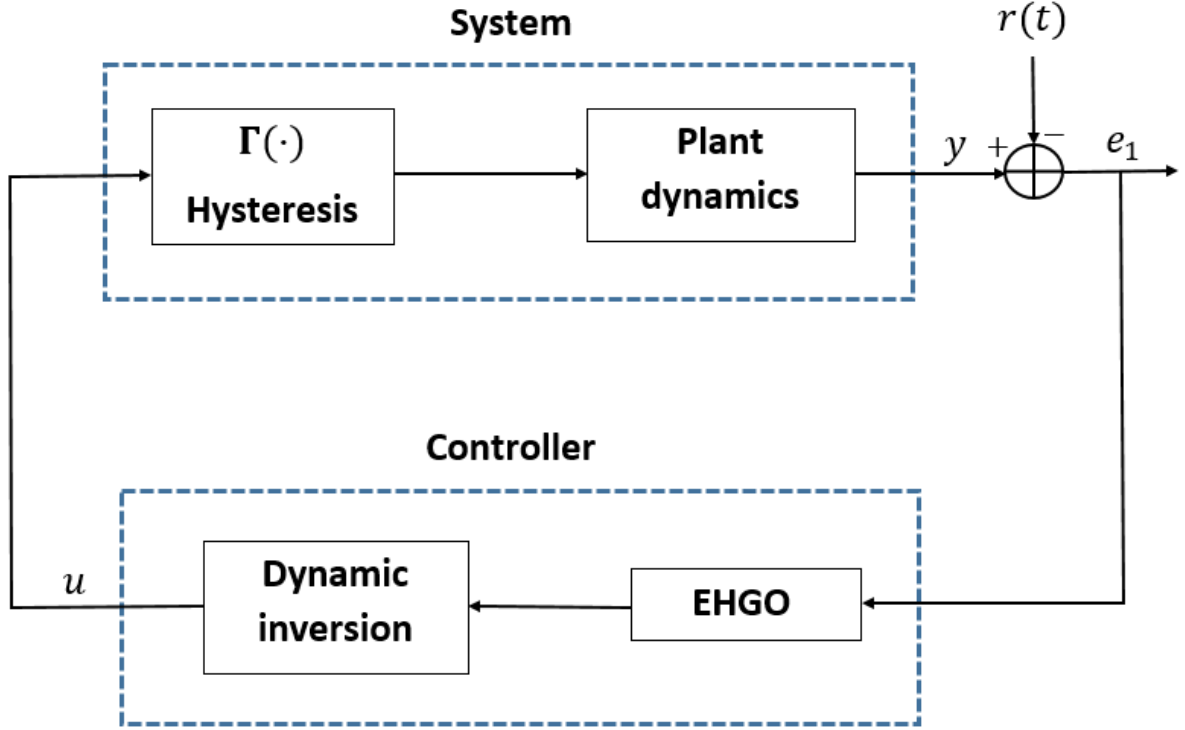
Figure 4.2: Block diagram illustrating the proposed approach. Here EHGO stands for extended high-gain observer.

Since σ and e are not available, we use an extended high-gain observer to get the estimates $(\hat{e}, \hat{\sigma})$ of (e, σ). The extended high-gain observer is constructed as

$$\dot{\hat{e}}_i = \hat{e}_{i+1} + \frac{\alpha_i}{\varepsilon^i}(e_1 - \hat{e}_1), \quad 1 \le i \le \rho - 1 \tag{4.19a}$$

$$\dot{\hat{e}}_\rho = \hat{\sigma} + \frac{\alpha_\rho}{\varepsilon^\rho}(e_1 - \hat{e}_1) \tag{4.19b}$$

$$\dot{\hat{\sigma}} = \frac{\alpha_{\rho+1}}{\varepsilon^{\rho+1}}(e_1 - \hat{e}_1) \tag{4.19c}$$

where α_1 to $\alpha_{\rho+1}$ are chosen such that the polynomial

$$s^{\rho+1} + \alpha_1 s^\rho + \ldots + \alpha_{\rho+1} \tag{4.20}$$

97

is Hurwitz, and $\varepsilon > 0$ is a small parameter. For sufficiently small ε, the estimation error decays to zero much faster than the system dynamics. High-gain observer suffers from the peaking phenomenon [82], where the estimation error peaks to the order of $O(1/\varepsilon^\rho)$ during the transient period and then it decays quickly to the order of $O(\varepsilon)$. In feedback control the peaking is overcome by designing the control to be a globally bounded function of the estimates $(\hat{e}, \hat{\sigma})$. Let

$$M > \max_{e \in \Omega_c} |Ke|,$$

$$N > \max_{\substack{(\eta, e, w) \in \Omega_0 \times \Omega_c \times W, \\ \mathcal{R} \in R_0, \, r^{(\rho)} \in R_1, \\ z \in \Omega_z}} |F(\eta, e, \mathcal{R}, w, r^{(\rho)}) + \Gamma[z + \phi]|.$$

The estimates are saturated as

$$(K\hat{e})_s = M\text{sat}\left(\frac{K\hat{e}}{M}\right), \quad \hat{\sigma}_s = N\text{sat}\left(\frac{\hat{\sigma}}{N}\right)$$

where $\text{sat}(y) = \min\{|y|, 1\}\,\text{sign}(y)$ for $y \in \mathbb{R}$. The dynamic inversion algorithm with the saturated estimates is given by

$$\mu\dot{u} = -[\hat{\sigma}_s + (K\hat{e})_s] \tag{4.21}$$

Theorem 4.2. *Consider the closed-loop system formed of the plant (4.13), the extended high-gain observer (4.19), and the dynamic inversion algorithm (4.21). Suppose that the Assumptions 4.1-4.5 are satisfied, α_1 to $\alpha_{\rho+1}$ are chosen such that the polynomial (4.20) is Hurwitz, $(\eta(0), e(0))$ belongs to a known compact subset in the interior of $\Omega_0 \times \Omega_c$, $|z(0)| < q$, and the initial states of the observer belong to a compact subset of $\mathbb{R}^{\rho+1}$. Then there exists $\lambda_1^* > 0$, such that for ε and μ with max $\{\mu, \varepsilon/\mu\} \leq \lambda_1^*$, the trajectories of the closed-loop system are bounded for all $t \geq 0$, and*

there exists $T^*(\lambda_1^*) > 0$ such that

$$\dot{e} = (A - BK)e + O(\lambda_1^*), \quad \forall\, t \geq T^*(\lambda_1^*). \tag{4.22}$$

Moreover given any $\Xi > 0$, there exists $\lambda_2^* > 0$, such that for ε and μ with $\max\{\mu, \varepsilon/\mu\} \leq \lambda_2^*$

$$\|e(t) - e_r(t)\| \leq \Xi, \quad \forall\, t \geq 0. \tag{4.23}$$

where $e_r(t)$ is the solution of the target system (4.14), with $e_r(0) = e(0)$.

Proof: Define the change of variables

$$\zeta_i = (e_i - \hat{e}_i)/\varepsilon^{\rho+1-i} \quad \text{for} \; 1 \leq i \leq \rho,$$

$$\zeta_{\rho+1} = \sigma - \hat{\sigma} = f(\eta, e + \mathcal{R}, w) + \Gamma[u](t) - r^{(\rho)} - \hat{\sigma}$$

The fast variable dynamics is given by

$$\varepsilon\dot{\zeta}_i = -\alpha_i\zeta_1 + \zeta_{i+1} \quad \text{for} \; 1 \leq i \leq \rho - 1, \tag{4.25a}$$

$$\varepsilon\dot{\zeta}_\rho = -\alpha_\rho\zeta_1 + \zeta_{\rho+1}, \tag{4.25b}$$

$$\varepsilon\dot{\zeta}_{\rho+1} = -\alpha_{\rho+1}\zeta_1 + \varepsilon\Delta_0 + (\varepsilon/\mu)\Delta_1, \tag{4.25c}$$

where

$$\Delta_0 = \frac{\partial\sigma}{\partial\eta}f_0 + \frac{\partial\sigma}{\partial e}\left[(A - BK)e + B\left(\Gamma[z + \phi](t) - \Gamma[\phi](t)\right)\right] + \frac{\partial\sigma}{\partial w}\dot{w} + \frac{\partial\sigma}{\partial\mathcal{R}}\dot{\mathcal{R}} - r^{(\rho+1)}$$

99

$$\Delta_1 = -\frac{\partial \sigma}{\partial u(t)} [\hat{\sigma}_s - \sigma + (K\hat{e})_s - Ke + \Gamma[z+\phi](t) - \Gamma[\phi](t)]$$

where the functions f_0, F are written without their arguments. Their complete forms are $f_0 = f_0(\eta, e + \mathcal{R}, w)$ and $F = F(\eta, e, \mathcal{R}, w, r^{(\rho)})$. The term $\dfrac{\partial \sigma}{\partial u(t)}$ can be written as

$$\frac{\partial \sigma}{\partial u(t)} = \frac{\partial \Gamma[u(\tau)|_{\tau=0}^t](t)}{\partial u(t)} = \frac{\partial g(u(t))}{\partial u(t)} + \frac{\partial \tilde{\Gamma}[u(\tau)|_{\tau=0}^t](t)}{\partial u(t)}$$

Using Proposition 4.1, for all $(\eta, e, w, \mathcal{R}, r^{(\rho)}, r^{(\rho+1)}, z) \in \Omega_0 \times \Omega_c \times W \times R_0 \times R_1 \times R_2 \times \Omega_z$, the term $\dfrac{\partial \sigma}{\partial u(t)}$ is bounded. The closed-loop system is represented by

$$\dot{\eta} = f_0(\eta, e + \mathcal{R}, w), \tag{4.26a}$$

$$\dot{e} = (A - BK)e + B[\Gamma[z+\phi](t) - \Gamma[\phi](t)], \tag{4.26b}$$

$$\mu\dot{z} = -(\Gamma[z+\phi](t) - \Gamma[\phi](t)) - \mu\dot{\phi} + \Delta_2, \tag{4.26c}$$

$$\varepsilon\dot{\zeta} = \Lambda\zeta + \varepsilon\bar{B}\Delta_0 + (\varepsilon/\mu)\bar{B}\Delta_1, \tag{4.26d}$$

where

$$\Delta_2 = -[\hat{\sigma}_s - \sigma + (K\hat{e})_s - Ke], \quad \zeta = \mathrm{col}(\zeta_1, \ldots, \zeta_{\rho+1}),$$

$$\Lambda = \begin{bmatrix} -\alpha_1 & 1 & 0 & \ldots & 0 \\ -\alpha_2 & 0 & 1 & \ldots & 0 \\ \vdots & \vdots & \ddots & \ddots & \vdots \\ -\alpha_\rho & 0 & \ldots & 0 & 1 \\ -\alpha_{\rho+1} & 0 & \ldots & \ldots & 0 \end{bmatrix}, \quad \bar{B} = \begin{bmatrix} 0 \\ 0 \\ \vdots \\ 0 \\ 1 \end{bmatrix}_{(\rho+1)\times 1}.$$

100

The solution of (4.26) is studied in the sense of Caratheodory solution. The matrix Λ is Hurwitz by construction. Since the initial states $(\eta(0), e(0), z(0))$ lie in the interior of $\Omega_0 \times \Omega_c \times \Omega_z$ and the right-hand-side functions of Eq. (4.26.a)-(4.26.c) are bounded uniformly in ε, there is time $\bar{T} > 0$ such that $(\eta(t), e(t), z(t)) \in \Omega_0 \times \Omega_c \times \Omega_z$ for all $t \in [0, \bar{T}]$. During this time period the terms Δ_0, Δ_1, Δ_2 are bounded by

$$|\Delta_0| \leq k_1, \;\; |\Delta_1| \leq k_2, \; |\Delta_2| \leq k_3$$

where k_1, k_2, k_3 are positive constants independent of μ and ε. This follows from the continuous differentiability of f, local Lipschitz property of f_0, boundedness of $\dfrac{\partial \sigma}{\partial u(t)}$, and global boundedness of $\hat{\sigma}_s$ and $(K\hat{e})_s$.

We define $\lambda = \max\left\{\dfrac{\varepsilon}{\mu}, \mu\right\}$ and show that there exist positive constants $\tilde{\lambda}_3$, γ_1, and γ_2, such that the set $\Omega_0 \times \Omega_c \times \{z : |z| \leq \gamma_1 \lambda\} \times \{\zeta : \zeta^T P_0 \zeta \leq \gamma_2 (\varepsilon/\mu)^2\}$ is positively invariant for all $\lambda \leq \tilde{\lambda}_3$, where $P_0 = P_0^T > 0$ is the solution to the Lyapunov equation $P_0 \Lambda + \Lambda^T P_0 = -I$. We construct the Lyapunov function $V_\zeta = \zeta^T P_0 \zeta$ and take its time derivative along Eq. (26d), which yields

$$\varepsilon \dot{V}_\zeta = -\zeta^T \zeta + 2\varepsilon \zeta^T P_0 \bar{B} \Delta_0 + 2(\varepsilon/\mu)\zeta^T P_0 \bar{B} \Delta_1$$

$$\varepsilon \dot{V}_\zeta \leq -||\zeta||^2 + 2k_1 \varepsilon ||P_0 \bar{B}|| \cdot ||\zeta|| + 2(\varepsilon/\mu)k_2 ||P_0 \bar{B}|| \cdot ||\zeta||$$

$$\leq -||\zeta||^2 + 2\varepsilon ||P_0 \bar{B}|| \left(k_1 + \frac{k_2}{\mu}\right) ||\zeta||$$

from which we have

$$\varepsilon \dot{V}_\zeta \leq -\frac{1}{2}||\zeta||^2, \;\; \text{for } ||\zeta|| \geq \frac{4\varepsilon}{\mu} ||P_0 \bar{B}||(k_1 + k_2)$$

101

By taking $\gamma_2 = 16||P_0\bar{B}||^2\lambda_{\max}(P_0)(k_1 + k_2)^2$, where $\lambda_{\max}(P_0)$ is the maximum eigenvalue of P_0, one gets

$$\varepsilon\dot{V}_\zeta \leq -\frac{1}{2}||\zeta||^2, \ \ \text{for} \ V_\zeta \geq \gamma_2(\varepsilon/\mu)^2$$

Therefore, on the boundary $\{\zeta : V_\zeta = \gamma_2(\varepsilon/\mu)^2\}$, we have $\dot{V}_\zeta < 0$. Following the high gain observer theory [73], one can show that initially $\zeta(0)$ could be outside the set $\{\zeta : V_\zeta \leq \gamma_2(\varepsilon/\mu)^2\}$, but it converges towards the set within time $T_1(\varepsilon)$, where $\lim_{\varepsilon \to 0} T_1(\varepsilon) = 0$. For sufficiently small ε, $T_1(\varepsilon) < (1/2)\bar{T}$. Therefore, $\zeta(t)$ enters the set $\{\zeta : \zeta^T P_0 \zeta \leq \gamma_2(\varepsilon/\mu)^2\}$, while $(\eta(t), e(t), z(t))$ remain in the interior of $\Omega_0 \times \Omega_c \times \Omega_z$. When $\zeta(t)$ enters the set $\{\zeta : \zeta^T P_0 \zeta \leq \gamma_2(\varepsilon/\mu)^2\}$ we have

$$K\hat{e} = Ke + O(\lambda), \ \ \hat{\sigma} = \sigma + O(\lambda)$$

Therefore, for sufficiently small λ, we have $K\hat{e} < M$ and $\hat{\sigma} < N$ which implies that the saturation in the estimates is no longer active, hence

$$K\hat{e}_s = K\hat{e}, \ \hat{\sigma}_s = \hat{\sigma}$$

Next we analyze the system (4.26.c) for $t \geq T_1(\varepsilon)$. Note that $z(t) \in \Omega_z$ during the time period $[0, T_1(\varepsilon)]$. We construct the Lyapunov function $V_z = \frac{1}{2}z^2$ and take its time derivative along Eq. (4.26.c), from which we have

$$\mu\dot{V}_z = -z\{\Gamma[z + \phi](t) - \Gamma[\phi](t)\} + z\Delta_2 - \mu z\dot{\phi}$$

The term Δ_2 after time $t \geq T_1(\varepsilon)$ is bounded by $||\Delta_2|| \leq k_4||\zeta||$, where k_4 is a positive constant

independent of λ, from which we have

$$\mu \dot{V}_z \leq -\beta_1 z^2 + \left[\frac{\varepsilon}{\mu} k_4 \sqrt{\frac{\gamma_2}{\lambda_{\min}(P_0)}} + \mu |\dot{\phi}| \right] |z|$$

$$\leq -\beta_1 z^2 + \lambda k_5 |z|$$

where $\lambda_{\min}(P_0)$ is the minimum eigenvalue of P_0 and k_5 is a positive constant independent of λ.

Therefore, we have

$$\mu \dot{V}_z \leq -\frac{\beta_1}{2} |z|^2, \quad \text{for } |z| \geq \frac{2k_5 \lambda}{\beta_1}$$

Taking $\gamma_1 = 2k_5 / \beta_1$ ensures that

$$\mu \dot{V}_z \leq -\frac{\beta_1}{2} |z|^2, \quad \text{for } |z| \geq \gamma_1 \lambda$$

Therefore, for all $\lambda \leq \tilde{\lambda}_1$, where $\tilde{\lambda}_1$ is a small positive constant chosen such that the set $\{z : |z| \leq \gamma_1 \lambda\}$ is in the interior of Ω_z. Similarly, following [73], one can show that initially $z(0)$ could be outside the set $\{z : |z| \leq \gamma_1 \lambda\}$, but it converges towards the set within time $T_2(\mu)$, where $\lim_{\mu \to 0} T_2(\mu) = 0$. For sufficiently small μ, the system trajectory enters the set $\Omega_0 \times \Omega_c \times \{z : |z| \leq \gamma_1 \lambda\} \times \{\zeta : \zeta^T P_0 \zeta \leq \gamma_2 (\varepsilon/\mu)^2\}$ for $t \geq T_1(\varepsilon) + T_2(\mu)$.

Next we analyze (4.26.b) for $t \geq T_1(\varepsilon) + T_2(\mu)$. Note that $(\eta(t), e(t)) \in \Omega_0 \times \Omega_c$ during the time period $[0, T_1(\varepsilon) + T_2(\mu)]$. Taking the time derivative of V_e along Eq. (4.26.b), which satisfies

$$\dot{V}_e = -e^T Q e + 2e^T P B \{\Gamma[z + \phi](t) - \Gamma[\phi](t)\}$$

$$\leq -\lambda_{\min}(Q) ||e||^2 + 2\tilde{k} ||e|| \cdot |z| \cdot ||PB||$$

$$\leq -\lambda_{\min}(Q) ||e||^2 + 2\lambda k_6 ||e||, \ \forall \ |z| \leq \gamma_1 \lambda$$

where $\tilde{k} = k + \beta_2$ using (3), (4), and (5), $k_6 = \gamma_1 k||PB||$ and $\lambda_{\min}(Q)$ is the minimum eigenvalue of Q, which implies

$$\dot{V}_e \leq -\frac{\lambda_{\min}(Q)}{2}||e||^2 \quad \text{for } ||e|| \geq \frac{4\lambda k_6}{\lambda_{\min}(Q)}$$

Therefore, for all $\lambda \leq \tilde{\lambda}_2$, where $\tilde{\lambda}_2$ is a small positive constant, $\dot{V}_e < 0$ on the boundary $\{e : V_e(e) = c\}$. Taking $\lambda \leq \tilde{\lambda}_3 = \min\{\tilde{\lambda}_1, \tilde{\lambda}_2\}$, ensures that the set $\Omega_0 \times \Omega_c \times \{z : |z| \leq \gamma_1 \lambda\} \times \{\zeta : \zeta^T P_0 \zeta \leq \gamma_2(\varepsilon/\mu)^2\}$ is positively invariant and enters it within time $T_1(\varepsilon) + T_2(\mu)$. Therefore, for $\lambda \leq \lambda_1^* = \min\{\tilde{\lambda}_1, \tilde{\lambda}_2, \tilde{\lambda}_3\}$, there is time $T^*(\lambda_1^*)$, such that for all $t \geq T^*(\lambda_1^*)$, (4.22) follows.

Next we show (4.23). Since the right-hand-side functions of Eq. (4.14) and Eq. (4.26.b) are bounded, uniformly in ε and μ, and $e(0) = e_r(0)$, it follows that

$$e(t) - e_r(t) = O(T_1(\varepsilon) + T_2(\mu)), \text{ for } 0 \leq t \leq T_1(\varepsilon) + T_2(\mu)$$

Hence, $e(T_1(\varepsilon) + T_2(\mu)) - e_r(T_1(\varepsilon) + T_2(\mu)) = O(T_1(\varepsilon) + T_2(\mu))$, and for $t \geq T_1(\varepsilon) + T_2(\mu)$, $e(t)$ satisfies

$$\dot{e} = (A - BK)e + O(\lambda).$$

Therefore, by continuous dependence of the solutions of differential equations and parameters [81, Theorem 9.1] and the exponential stability of the origin of $\dot{e} = (A - BK)e$, we conclude that

$$e(t) - e_r(t) = O(\lambda) + O(T_1(\varepsilon) + T_2(\mu)), \ t \geq 0$$

Hence, given $\Xi > 0$, there exists $\lambda_2^* > 0$, such that for all $\lambda \in (0, \lambda_2^*)$, (4.23) follows.

4.5 Simulation Results

In this section, a simulation study is conducted to examine the performance of the proposed controller and to highlight the impact of the dynamic inversion parameter μ and the high-gain observer parameter ε on the smallness of the tracking error. For simulation purposes, we consider the model for a piezo-actuated nanopositioner, which was identified experimentally and used for the controller design in [54]. Its worth mentioning that the same setup is used later for experimental verification of the proposed controller presented in next section. The model is composed of two cascaded blocks. The first block represents the input hysteresis nonlinearity, modeled by a Modified Prandtl-Ishlinskii (MPI) operator consisting of 8 play operators and 9 deadzone operators. The other block represents the vibrational dynamics, represented as a linear state-space system. The augmented system can be represented as

$$\dot{\xi} = A_\xi \xi + B_\xi \left[\Gamma_\xi \left[u; v_o \right] (t) + d_\xi (t) \right] \tag{4.27}$$

where $\xi \in \mathbb{R}^2$ represents the displacement and velocity of the nanopositioning stage, Γ_ξ is the MPI operator with v_o being its initial state, $d_\xi \in \mathbb{R}$ is the input disturbance, and the matrices

$$A_\xi = \begin{bmatrix} 0 & 1 \\ 1.795 \times 10^8 & 5696.88 \end{bmatrix} \text{ and } B_\xi = \begin{bmatrix} 0 \\ 1.063 \times 10^9 \end{bmatrix}$$

It should noted that the model (4.27) is a special case of the general model (4.1) in Section 4.2. Throughout the simulation studies, the observer parameters are taken as $\alpha_1 = 3$, $\alpha_2 = 3$, and $\alpha_3 = 1$, while the controller gain is taken as $K = \begin{bmatrix} 2 & 1 \end{bmatrix}$. Moreover, it was assumed that the nanopositioner is initially at a stationary state with position zero at the starting point. A sinusoidal reference is

Table 4.1: Simulation results: Mean and Max $|e(t)|\%$ in percent of the reference amplitude in the state feedback case.

μ	Mean $|e(t)|\%$	Max $|e(t)|\%$
0.1	0.0584	0.0956
0.01	0.0526	0.0895
0.001	0.0119	0.0219
0.0001	0.0012	0.0022

used with frequency of 100 Hz and amplitude of 10 μm. The input disturbance signal d_ξ consists of the 3rd, 5th, and 7th harmonics of the reference signal frequency with amplitudes equal to 1, 0.2, and 0.1, respectively.

Table 4.1 shows the simulation results for the state feedback case, where all system state variables and the hysteretic output are measured. Both the mean and maximum values of the tracking error, normalized by the amplitude of the reference signal (and thus expressed as %), are shown in Table 4.1, for a range of dynamic inversion parameter μ. As observed clearly, both the mean and maximum errors are reduced significantly when the value of the parameter μ is decreased.

Table 4.2 shows the simulation results for the output feedback case, where the value of the parameter μ is fixed at 0.1, while the extended high-gain observer parameter ε is chosen at a few different values as shown in the table. Note that both the mean and maximum tracking errors are reduced dramatically when the value of ε is reduced from 0.01 to 0.001. However, reducing the value of ε to lower values only results in slight decrease in the tracking errors, which inch towards the tracking error performance in the state-feedback case for $\mu = 0.1$.

The above simulation results support the major theoretical findings as summarized in both Theorem 4.1 and 4.2; in particular, the tracking error will be reduced with a decreasing μ under state feedback, and with a decreasing ratio of $\frac{\varepsilon}{\mu}$ under output feedback case, respectively.

Table 4.2: Simulation results: Mean and Max $|e(t)|\%$ in percent of the reference amplitude in the output feedback case with $\mu = 0.1$.

ε	Mean $|e(t)|\%$	Max $|e(t)|\%$
0.01	0.2202	0.4512
0.001	0.0609	0.0958
0.0001	0.0607	0.0954
0.00001	0.0602	0.0953

4.6 Experimental Results

To further verify the theoretical results, a series of tracking experiments are conducted on a commercial nanopositioner (Nano OP-65, from Mad City Labs). The piezo-actuated positioner has a built-in capacitive sensor that measures its displacement. The data acquisition and control are realized through dSPACE (DS1104) as shown in Fig. 2.5. Three types of reference signals are used in the experiments, including sinusoidal signals, sawtooth signals, and multi-harmonic signals. The observer and the controller parameters used in the experiments are $\alpha_1 = 3$, $\alpha_2 = 3$, $\alpha_3 = 1$, $\mu = 0.01$, $\varepsilon = 6.6667 \times 10^{-6}$, and $K = [2, 1.3398 \times 10^4]$. To mitigate the effect of noise amplification due to the use of high-gains in the observer, a low-pass filter with 1 KHz bandwidth is inserted at the measurement side.

4.6.1 Sinusoidal Reference Signals

In the experiments we have used four different sinusoidal signals with frequencies of 5, 25, 50, 100 Hz, respectively. The experimental results for the highest reference frequency, i.e., 100 Hz, are shown in Fig. 4.4. As can be seen in Fig. 4.4(a), the measured position output converges to the reference signal at roughly 0.009 seconds, which is shown more clearly in Fig. 4.4(b). Moreover, it can be seen in the magnified part of Fig. 4.4(b) that the tracking error at the steady state is within ± 0.055 μm. In Fig. 4.4(c), the frequency content of the tracking error signal $e_1(t)$ is shown. In

Table 4.3: Experimental results: Comparison of the Mean $|e(t)|\%$ in tracking a sinusoidal reference.

Frequency	EHGO-DI	SMC	SHSC	MHSC	PI
5 Hz	0.1343	0.1190	0.6490	0.2710	0.5141
25 Hz	0.1330	0.6200	0.7070	0.2680	0.5540
50 Hz	0.1371	0.6600	0.7700	0.2840	0.6286
100 Hz	0.2051	0.8300	0.8150	0.3520	0.8242

Table 4.4: Experimental results: Comparison of the Max $|e(t)|\%$ in tracking a sinusoidal reference.

Frequency	EHGO-DI	SMC	SHSC	MHSC	PI
5 Hz	0.2306	0.9500	1.7200	0.8990	2.3477
25 Hz	0.2765	1.7000	1.8500	0.8810	2.4854
50 Hz	0.3642	2.2500	1.9300	1.0100	3.0326
100 Hz	0.6666	2.7500	2.3800	1.5700	3.8560

addition to the fundamental frequency at 100 Hz, the third is also relatively pronounced. Note that most of the tracking error magnitude is due to first harmonic, which its absolute amplitude is less than 0.03 μm.

Tables 4.3 and 4.4 further provide a comparison of the tracking error performance between the proposed controller (EHGO-DI) and several competing controllers, including a sliding mode controller (SMC) with hysteresis inversion in [48], a single-harmonic servocompensator (SHSC) [5], a multiple-harmonic servocompensator (MHSC) [5], and a proportional integral controller implemented solely without using feedforward inversion, for the mean error and the maximum error, respectively. Note that hysteresis inversion is used in both SHSC and MHSC [5]. From both tables, it can be seen that, overall the proposed controller outperforms all the other approaches,

Table 4.5: Experimental results: Mean and Max $|e(t)|\%$ in percent of the reference amplitude for sawtooth and Multi-Harmonic references.

Frequency	sawtooth		Multi-Harmonic	
	Mean $|e(t)|\%$	Max $|e(t)|\%$	Mean $|e(t)|\%$	Max $|e(t)|\%$
5 Hz	0.1354	0.2355	0.1389	0.2440
25 Hz	0.1358	0.3422	0.1397	0.3063
50 Hz	0.1401	0.5388	0.1496	0.4671
100 Hz	0.1893	0.8905	0.2486	0.9744
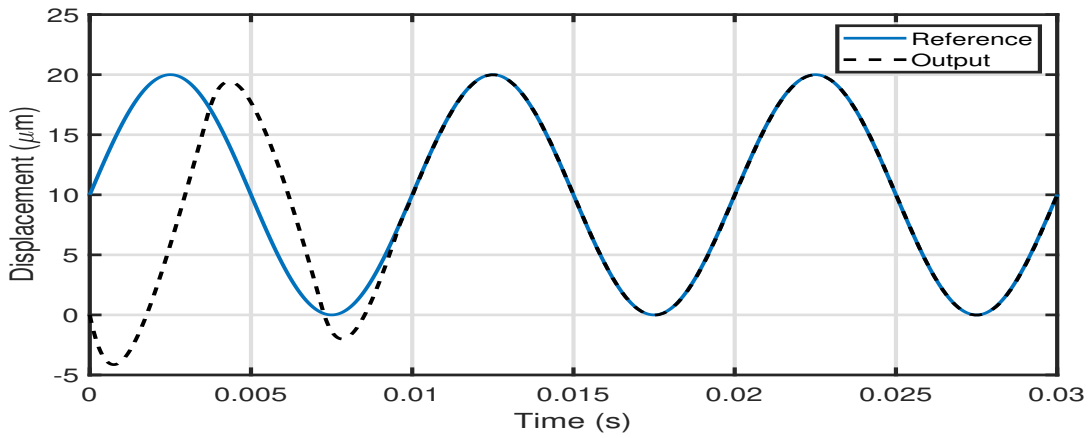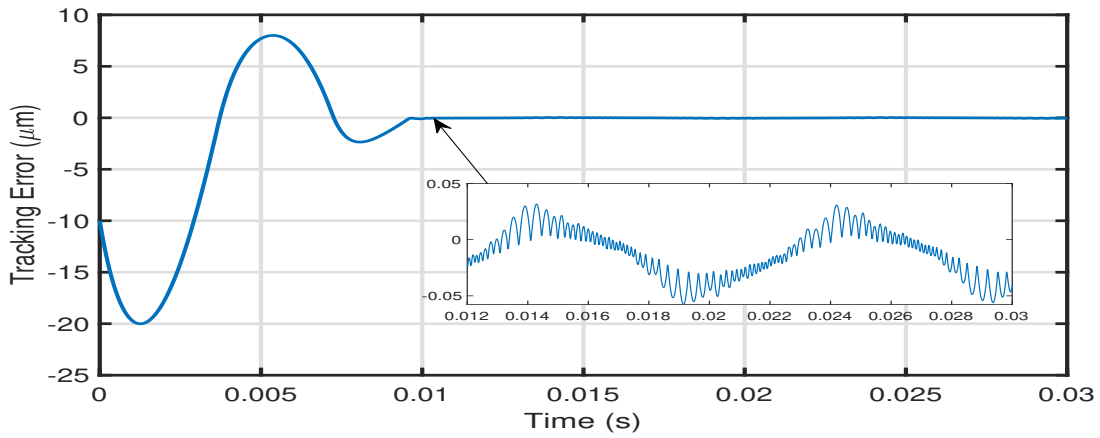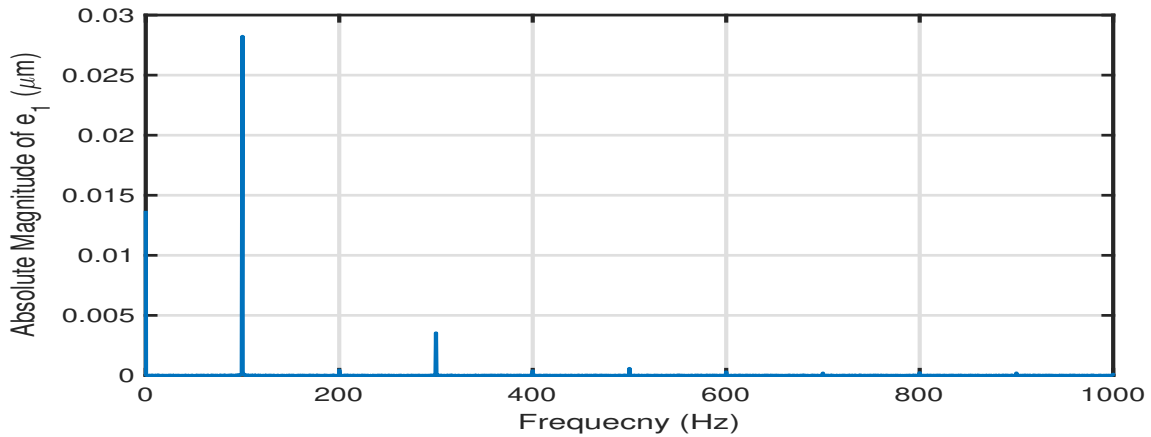
Figure 4.3: Experimental results on tracking a 100 Hz sinusoidal reference signal. (a) Positioner displacement; (b) tracking error; (c) frequency spectrum of the tracking error.

despite that it does not use hysteresis modeling and inversion as the other methods do. In Table 4.3, it can noticed that our proportional integral controller is comparable to the SHSC controller and it does slightly better than the SMC approach. However, the PI controller's maximum absolute error comes higher than all other approaches.

4.6.2   Sawtooth Reference Signals

The next set of experiments are implemented with sawtooth reference signals with frequencies of 5, 25, 50, and 100 Hz, respectively. To avoid impulsive behavior, a second-order linear filter is utilized to smooth out the signal edges. Fig. 4.5(a) and 4.5(b) show the time tr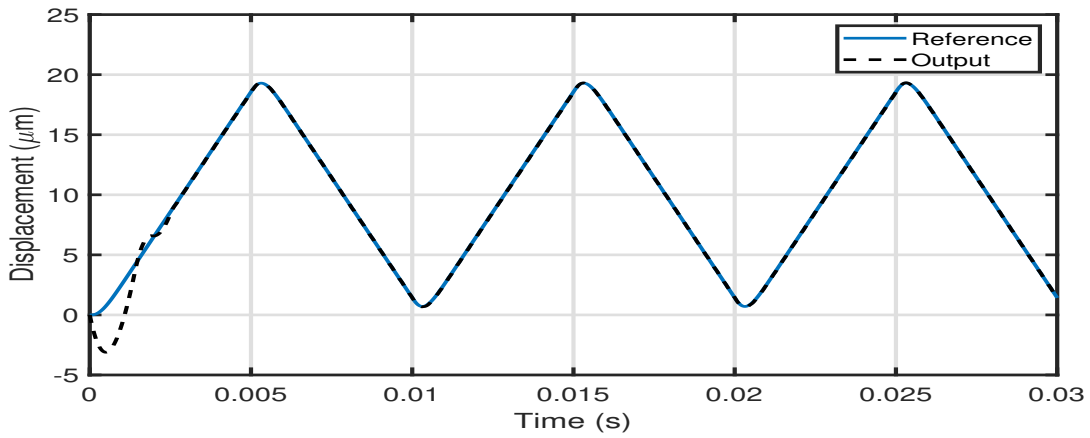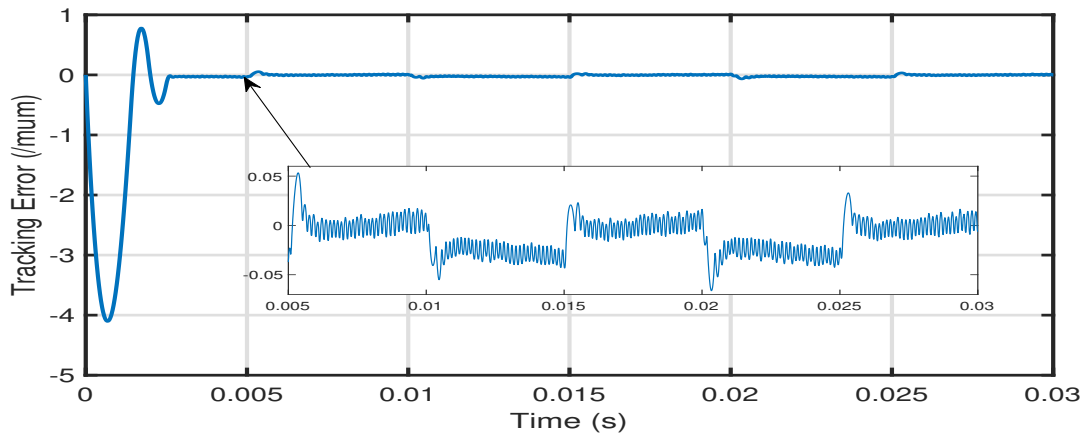ajectories of the positioner displacement and the tracking error for the 100 Hz case, where it can be seen that the displacement converges to the reference signal at roughly 0.003 seconds. Note that the tracking error is confined to around ±0.05 μm at the steady state. It can be observed in Fig. 4.5(c), that the error signal contains more harmonic terms than the case of tracking a sinusoidal reference. The first part of Table 4.5 shows the mean and maximum tracking errors over the considered range of frequencies. Notice that the growth of tracking error with the increase of frequency is largely consistent with the results in the sinusoidal case.

4.6.3   Multi-Harmonic Reference Signals

In the final set of experiments, the tracking of a multi-harmonic signal with first and second harmonics is implemented. Similar to the previous experiments, we consider a range of primary frequencies, $5, 25, 50, 100$ Hz. As seen from Fig. 4.6(a) and 4.6(b), the positioner output converges to the reference signal in roughly 0.006 seconds. The tracking error at the steady state is larger than the two previous cases (sinusoidal and sawtooth references). Fig. 4.6(c) also shows the amplitudes

(a)

(b)
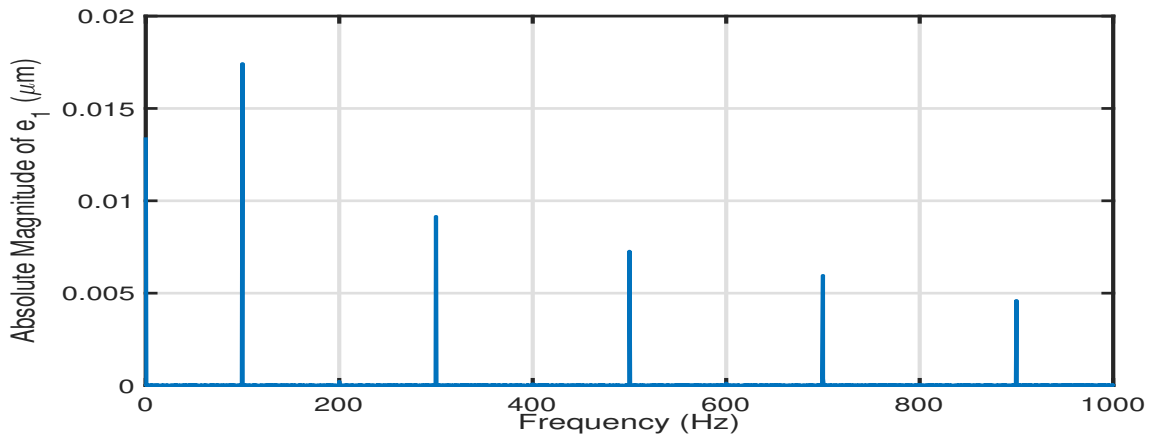
(c)

Figure 4.4: Experimental results on tracking a 100 Hz sawtooth reference signal. (a) Positioner displacement; (b) tracking error; (c) frequency spectrum of the tracking error.

111

of the 1st and 2nd harmonic components of the error. It can be noticed that the absolute amplitude of the 2nd harmonic is larger than the 1st one. The second half of Table 4.5 shows quantitative results on the tracking error for all frequencies. Overall the results are satisfactory; the tracking errors are slightly larger comparing to the smoothed sawtooth case. This can be attributed to the pronounced 2nd harmonic component in the reference signal.
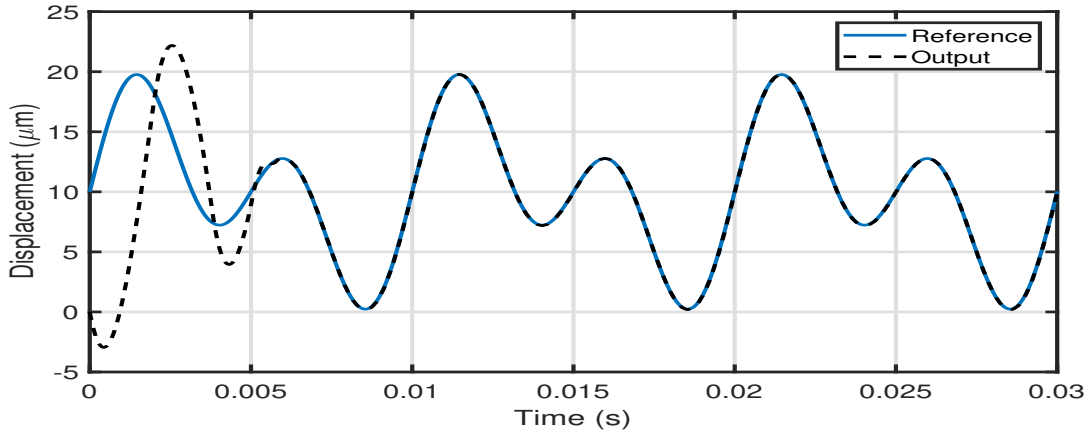
(a)
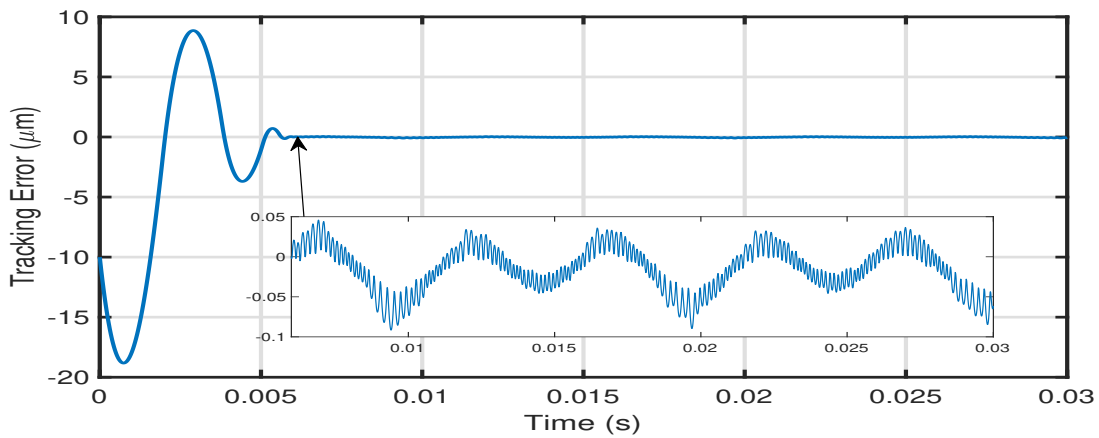
(b)
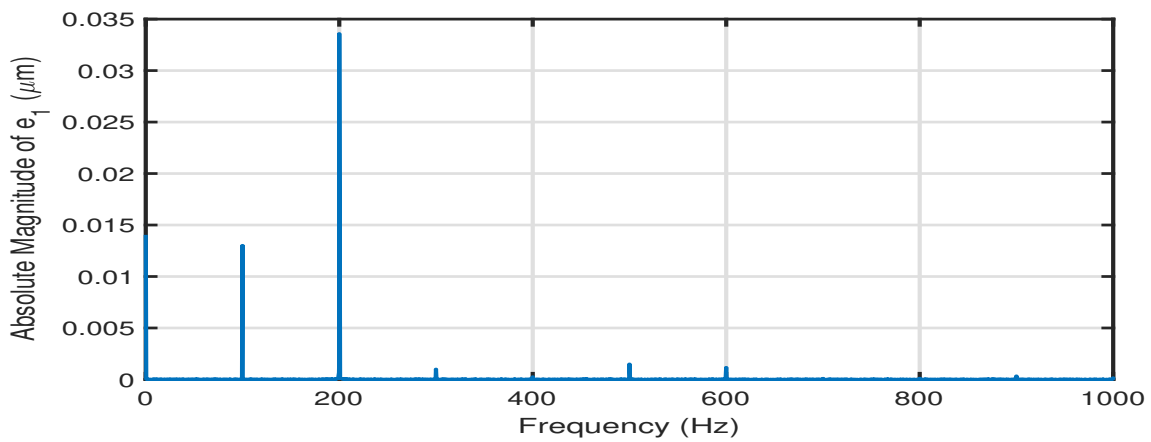
(c)

Figure 4.5: Experimental results on tracking a reference signal generated via the multi-harmonic signal with a primary frequency of 100 Hz. (a) Positioner displacement; (b) tracking error; (c) frequency spectrum of the tracking error.

Chapter 5

Conclusions and Future Work

5.1 Conclusions

5.1.1 Inversion-based ACS Approach

We first focused on designing an "inversion-based" adaptive conditional servocompensator closed-loop system for a class of hysteretic systems. Under this control law, the closed-loop system will have behavior over two different stages. The first one is a reaching phase, where the controller is a continuously-implemented sliding mode control law. In this stage, we have designed the control law to accommodate hysteric inversion error perturbations by deriving an analytical bound on the these perturbations. The switching part of the control law is designed using the analytical bound to reduce the conservativeness as compared to the case when a constant bound is used. The second stage starts when the sliding variable enters the boundary layer and stays therein forever. In this case, the adaptation law is activated "conditionally" to handle the residual hysteretic perturbations. Our stability analysis embodied in Theorem 2.1 and 2.2 establishes well-posedness and periodic stability for the closed-loop system. The theoretical framework used to prove the periodic stability is originally presented in [68]; however, new results were developed in this work since our closed-loop system does not fit the assumptions of [68] completely due to non-smooth terms in both the control and the adaptation laws. Next, we validated the inversion-based experimentally. The results confirmed its superiority as compared with other control algorithms implemented on the

same device.

5.1.2 Inversion-free ACS Approach

We next considered designing an "inversion-free" adaptive conditional servocompensator to mitigate the effect of hysteresis in systems preceded by an MPI operator. Under the assumption that only the weights of the operator are uncertain, we proved that the MPI operator can be represented in a semi-affine form. This transformation converts the MPI operator into a sum of a linear part, a hysteretic term modeled with a classical PI operator with nominal weights, and a hysteretic perturbation term. Then, we established that the hysteretic perturbation term obeys a linear growth bound, which is utilized in designing less conservative continuously-implemented sliding-mode control law as compared to the case when a general constant bound is used. Similar to the inversion-based control algorithm, the first part of the controller is a continuously-implemented sliding mode controller, where its switching part is designed with a variable-gain function utilizing a derived analytical bound on the hysteretic perturbation to reduce conservativeness.

Next, we introduced a low-pass filter technique to address a challenge in solving for the equivalent control term. The validity of the approach was justified by analysis. It should be noted that, the same issue appeared in the work of [40], where the authors approximated an integral term of the PI operator with a summation over a time interval divided by a number of time steps, but without incorporating the approximation error in the analysis. It is worth mentioning that both converting the system to the semi-affine form and designing the low-pass filter are crucial to producing a less conservative sliding mode control law, as they allow one to isolate the nominal hysteretic part from the hysteric perturbation terms. In particular, this makes it plausible to assume $\bar{K}_o < 1$. The second part of the control law is the adaptive conditional servomechanism, which is designed based on the assumption that the disturbance is generated by neutrally stable exogenous system. Due to this

approximation, an internal model perturbation term is generated to accommodate the residual error. Next we focused on conducting the stability analysis of the inversion-free closed-loop system without the requirement of the smallness of the hysteric perturbation, as required in the theoretical framework introduced in [68]. Then we proved the ultimate boundedness of the closed-loop systems' variables and the tracking error was shown to be bounded by a small bound.

We next demonstrated the efficacy of the inversion-free control algorithm through experimental study by implementing the proposed control algorithm on a commercial nanopositioner and compared its performance with other competing schemes. The proposed inversion-free method showed superior performance in tracking different types of periodic desired references.

5.1.3 Dynamic Inversion Based on Extended High-gain Observer Approach

Finally, we presented a novel hysteresis compensation algorithm using dynamic inversion and extended high-gain observer. While many of the state-of-the-art methods for hysteresis compensation require an explicit model of the hysteresis and the construction of (often times) computation-intensive inverse hysteresis model, the proposed approach does not require either. In addition, the controller is robust with respect to the system uncertainties and does not require the exact knowledge of the plant parameters. This is because such uncertainties can be combined with the hysteresis output in the signal σ, which is estimated by the extended high-gain observer. The mild assumption on the hysteresis nonlinearity is easily satisfied by popular hysteresis operators like the classical PI operator, the generalized PI operator and the Preisach operator. We extended the dynamic inversion theory to the case of hysteretic systems with rigorous analysis. Then we further validated the proposed approach with both simulation and extensive experimental evaluation.

5.2   Future Work Recommendations

There are still remaining ideas to be explored along the lines of the approaches introduced in this dissertation. One potential direction is to explore the inversion-based and the inversion-free approaches with different hysteresis models like the Preisach model, or the Krasnosel'skii-Pokrovskii model. One limitation of the proposed inversion-free control algorithm in Chapter 3 is the restrictive assumption that reduces the ability of the MPI operator to represent asymmetric hysteresis behavior. A potential future work is to try to relax that assumption, which will widen the scope of the proposed controller to more general applications that suffer from asymmetric hysteresis.

In both Chapters 2 and 3, we designed the output feedback inversion-based and inversion-free control algorithms using standard high-gain observers [81] to reconstruct the unmeasured states. However, one challenge in numerical implementation of the observer is that the observer gain is $O\left(\frac{1}{\varepsilon^n}\right)$, where n is the system model order. During the peaking (transient) phase, the observer internal states are $\mathcal{O}\left(\frac{1}{\varepsilon^{n-1}}\right)$. One recommended future research is to consider the cascade high-gain observer scheme, which was introduced in [90] by Khalil in 2017. The cascade high-gain observer is designed by cascading lower-dimensional observers with saturation functions inserted in between them. One advantage of following such approach is that the observer gain in the cascade observer is are limited to be $\mathcal{O}\left(\frac{1}{\varepsilon}\right)$ and the observer internal states peak will be $\mathcal{O}\left(\frac{1}{\varepsilon}\right)$ also during the transient period.

Another suggested approach is motivated by the work of Astolfi et al. [91]. In their work, they also proposed a low-power cascade high-gain observer that preserves the main feature of standard high-gain observers in terms of arbitrarily fast convergence of the estimation error to zero, while overcoming their main drawbacks, namely the "peaking phenomenon" during the transient and the numerical implementation issue deriving from the high-gain parameter that is powered up to the

order of the system. The proposed cascade observer has superior features in terms of sensitivity of the estimation error to high-frequency measurement noise when compared with standard high-gain observers. The main difference of cascade observer structure of the work of [91] as compared to Khalil's cascade observer [90] is that first one is built using second-order observers, while the later is built using first-order observers. It is worth mentioning that in Khalil's cascade observer [90], the effect of measurement noise on a feedback control system is comparable to its effect on a system that uses the standard observer.

Another recommendation is to consider robust design of nonlinear internal models without adaptation proposed by Isidori et al. in 2012 [92]. Unlike the approaches used in Chapters 2 and 3, which rely on conventional adaptation schemes to estimate the frequency of the exogenous signals, their proposed approach utilizes regression-like arguments to derive a nonlinear internal model that is able to offset the presence of an unknown number of harmonic exogenous inputs of uncertain amplitude, phase and frequency. However, one challenge that should be resolved is that the work in [92] does not consider the hysteretic disturbances in the system. Therefore, further efforts should be spent to extend this approach to include hysteretic perturbations.

APPENDICES

A.1 Proof of Theorem 2.1

Define the following integration operator:

$$\mathcal{X}(t) := \mathcal{C}[\mathcal{X}](t)$$
$$= \mathcal{X}^o + \int_0^t \mathcal{F}_{cl}\left(s, \mathcal{X}, \mathcal{W}_{inv}[u_{in}; W_{in}(0)](s)\right) ds \tag{A.1}$$

where $\mathcal{X}^o = \mathcal{X}(0)$ and the mapping $\mathcal{C}[\mathcal{X}](t) : \Omega_{\mathcal{X}} \times \Omega_{\mathcal{H}} \to \Omega_{\mathcal{X}} \times \Omega_{\mathcal{H}}$. Due to the equivalence of

solutions of both (2.48), and (A.1), we will continue the proof using (A.1). Let us define a closed

set $\mathcal{S} \subset [0,t] \times \mathcal{R}^{rc} \times \mathbb{W}_t^{1,1}$,

$$\mathcal{S} := \{t \in [0, t_c], \ \mathcal{X} \in \Omega_{\mathcal{X}}, \ and \ W_{in} \in \Omega_{\mathcal{H}}\}$$

where $t_c > 0$ will be calculated shortly. The first step in order to establish that $\mathcal{C}[\mathcal{X}](t)$ is a con-

traction over $\mathcal{S}$ is to show that $\mathcal{C}[\mathcal{X}](t)$ maps $\mathcal{S}$ into itself. To do this, we rewrite (A.1) by adding

and subtracting the term $\mathcal{F}_{cl}\left(s, \mathcal{X}^o, \mathcal{W}_{inv}[u_{in}^o; W_{in}(0)](s)\right)$ inside the integral,

$$\mathcal{C}[\mathcal{X}](t) - \mathcal{X}^o = \int_0^t \Big[\mathcal{F}_{cl}\left(s, \mathcal{X}, \mathcal{W}_{inv}[u_{in}; W_{in}(0)](s)\right)$$
$$+ \mathcal{F}_{cl}\left(s, \mathcal{X}^o, \mathcal{W}_{inv}[u_{in}^o; W_{in}(0)](s)\right) \tag{A.2}$$
$$- \mathcal{F}_{cl}\left(s, \mathcal{X}^o, \mathcal{W}_{inv}[u_{in}^o; W_{in}(0)](s)\right) \Big] ds$$

where u_{in}^o is the control input evaluated at $t = 0$. From the local Lipschitz continuity properties

of the function $\mathcal{F}_{cl}(\cdot)$, the function $\mathcal{F}_{cl}\left(t, \mathcal{X}, \mathcal{W}_{inv}[u_{in}^o; W_{in}(0)](t)\right)$ is bounded over the interval

$t \in [0, t_u]$, and for all $\mathcal{X}, W_{in} \in S$, where the final value of t_c will be picked later no greater than t_u.

Hence, define

$$b_f \stackrel{\triangle}{=} \max_{\substack{t \in [0,t_u] \\ \mathcal{X}, W_{in} \in \mathcal{S}}} \| \mathcal{F}_{cl} \left(t, \mathcal{X}^o, \mathcal{W}_{inv}[u_{in}^o; W_{in}(0)](t) \right) \|_1$$

From the Lipschitz properties of the function $\mathcal{F}_{cl}(\cdot)$ and in light of the definition of the standard norm (2.13), we can show that the first two terms of the integrand in (A.2) satisfy the following inequality:

$$\| \mathcal{F}_{cl} \left(s, \mathcal{X}, \mathcal{W}_{inv}[u_{in}; W_{in}(0)](s) \right) - \mathcal{F}_{cl} \left(s, \mathcal{X}^o, \mathcal{W}_{inv}[u_{in}^o; W_{in}(0)](s) \right) \|_1 \leq$$

$$L_{x_1} \| \mathcal{X} - \mathcal{X}^o \|_{\mathbb{W}_t^{1,1}} + L_{h_1} \| \mathcal{W}_{inv}[u_{in}; W_{in}(0)](s) - \mathcal{W}_{inv}[u_{in}^o; W_{in}(0)](s) \|_{\mathbb{W}_t^{1,1}} \tag{A.3}$$

where L_{x_1} and L_{h_1} are the corresponding Lipschitz constants dependent on $\mathcal{X}^o$, $r_{\mathcal{X}}$, and $r_{\mathcal{H}}$. By using the Lipschitz property of the MPI operator $\mathcal{W}_{inv}[\cdot]$, proven in Proposition 2.1, we have

$$\| \mathcal{W}_{inv}[u_{in}; W_{in}(0)](s) - \mathcal{W}_{inv}[u_{in}^o; W_{in}(0)](s) \|_{\mathbb{W}_t^{1,1}} \leq L_{h_2} \| u_{in} - u_{in}^o \|_{\mathbb{W}_t^{1,1}}$$

Let $u_{in}(t) = \alpha_{in}(.)$, where $\alpha_{in}(.)$ is a piecewise continuous function in t, then inside the set $\mathcal{S}$, we can derive

$$\| u_{in} - u_{in}^o \|_{\mathbb{W}_t^{1,1}} = \int_0^t \| u_{in}'(s) - u_{in}^{o\prime}(s) \|_1 \mathrm{d}s \leq \int_0^t \left\| \frac{\partial \alpha_{in}(\mathcal{X})}{\partial \mathcal{X}} \mathcal{X}' \right\|_1$$

$$\leq \int_0^t \left\| \frac{\partial \alpha_{in}(\mathcal{X})}{\partial \mathcal{X}} \right\|_1 \| \mathcal{X}' \|_1 \leq \int_0^t c_1 \| \mathcal{X}'(s) \|_1 \mathrm{d}s \tag{A.4}$$

$$\leq c_1 r_{\mathcal{X}}$$

where

$$c_1 = \max_{\mathcal{X} \in \mathcal{S}} \left\| \frac{\partial \alpha_{in}(\mathcal{X})}{\partial \mathcal{X}} \right\|_1 \tag{A.5}$$

Notice that the norm $\| \cdot \|_1$ in (A.5) is an induced norm. Now taking the 1-norm of both sides of (A.2), and utilizing the local Lipschitz properties of $\mathcal{F}_{cl}(\cdot)$ along with inequalities (A.3)- (A.4),

we get

$$\|\mathcal{C}[\mathcal{X}](t) - \mathcal{X}^o\|_1 \le \|\mathcal{C}[\mathcal{X}](t) - \mathcal{X}^o\|_{\mathbb{W}_t 1,1} \le \int_0^t \left[L_{x_1} \|\mathcal{X}(s) - \mathcal{X}^o(s)\|_{\mathbb{W}_t 1,1} \right.$$

$$\left. + L_{h_1} \|\mathcal{W}_{inv}[u_{in}; W_{in}(0)](s) - \mathcal{W}_{inv}[u_{in}^o; W_{in}(0)](s)\|_{\mathbb{W}_t 1,1} + b_f \right] ds \le t_c b_q \tag{A.6}$$

where $b_q = L_{x_1} r_{\mathcal{X}} + L_{h_1} L_{h_2} c_1 r_{\mathcal{X}} + b_f$. From the above inequality, we have established the boundedness of the function $\mathcal{F}_{cl}(s, \mathcal{X}, \mathcal{W}_{inv}[u_{in}; W_{in}(0)](s))$. Hence, by choosing $t_c \le \frac{r_{\mathcal{X}}}{b_q}$, we can ensure that $\mathcal{C}[\mathcal{X}](t) : \mathcal{S} \to \mathcal{S}$.

The next step is to show that the mapping $\mathcal{C}[\mathcal{X}](t)$, with careful selection of t_c, is a contraction mapping over $\mathcal{S}$. Let $\mathcal{X}_1$ and $\mathcal{X}_2 \in \mathcal{S}$, and consider the norm

$$\|\mathcal{C}[\mathcal{X}_1](t) - \mathcal{C}[\mathcal{X}_2](t)\|_1 = \int_0^t \left\| \mathcal{F}_{cl}\left(s, \mathcal{X}_1, \mathcal{W}_{inv}[u_{in}^1; W_{in}(0)](s)\right) \right.$$

$$\left. - \mathcal{F}_{cl}\left(s, \mathcal{X}_2, \mathcal{W}_{inv}[u_{in}^2; W_{in}(0)](s)\right) \right\|_1 ds \le \int_0^t \left[L_{x_1} \|\mathcal{X}_1(s) - \mathcal{X}_2(s)\|_{\mathbb{W}_t 1,1} \right.$$

$$\left. + L_{h_1} \|\mathcal{W}_{inv}[u_{in}^1; W_{in}(0)](s) - \mathcal{W}_{inv}[u_{in}^2; W_{in}(0)](s)\|_{\mathbb{W}_t 1,1} \right] ds$$

$$\le t_c \left[L_{x_1} \|\mathcal{X}_1(s) - \mathcal{X}_2(s)\|_{\mathbb{W}_t 1,1} + L_{h_1} L_{h_2} \|u_{in}^1 - u_{in}^2\|_{\mathbb{W}_t 1,1} \right] \tag{A.7}$$

Similar to the steps that lead to (A.4), we have

$$\|u_{in}^1(s) - u_{in}^2(s)\|_{\mathbb{W}_t 1,1} = \int_0^t \|u_{in}^{1\prime}(s) - u_{in}^{2\prime}(s)\|_1 ds$$

$$\le \int_0^t \left[\| \frac{\partial \alpha_{in}(\mathcal{X}_1(s))}{\partial \mathcal{X}} \mathcal{X}_1'(s) - \frac{\partial \alpha_{in}(\mathcal{X}_2(s))}{\partial \mathcal{X}} \mathcal{X}_2'(s) \|_1 ds \right. \tag{A.8}$$

By adding and subtracting the term $\left(\frac{\partial \alpha_{in}(\mathcal{X}_1(s))}{\partial \mathcal{X}} \mathcal{X}_2'(s) \right)$, inside the norm of the above integral,

122

we have

$$\|u_{in}^1(s) - u_{in}^2(s)\|_{\mathbb{W}_t^{1,1}} \leq \int_0^t \left\| \frac{\partial \alpha_{in}(\mathcal{X}(s))}{\partial \mathcal{X}} \left[\mathcal{X}_1'(S) - \mathcal{X}_2'(S)\right] \right.$$

$$\left. - \left[\frac{\partial \alpha_{in}(\mathcal{X}_1(s))}{\partial \mathcal{X}} - \frac{\partial \alpha_{in}(\mathcal{X}_2(s))}{\partial \mathcal{X}}\right] \mathcal{X}_2'(s) \right\|_1 ds \leq \int_0^t \left[c_1 \|\mathcal{X}_1'(s) - \mathcal{X}_2'(s)\|_{\mathbb{W}_t^{1,1}} \right.$$

$$\left. + L_{\alpha_{in}} \|\mathcal{X}_2\|_{\mathbb{W}_t^{1,1}} \max_{\mathcal{X} \in \mathcal{S}} \|\mathcal{X}_1(s) - \mathcal{X}_2\|_{\mathbb{W}_t^{1,1}} \right] ds \leq b_\rho \|\mathcal{X}_1(s) - \mathcal{X}_2\|_{\mathbb{W}_t^{1,1}} \quad \text{(A.9)}$$

where $b_\rho = c_1 + c_2 L_{\alpha_{in}}$, $c_2 = \max_{\mathcal{X} \in S} \|\mathcal{X}_2\|_{\mathbb{W}_t^{1,1}}$, and $L_{\alpha_{in}}$ is the the local Lipschitz constant of the function $\frac{\partial \alpha_{in}}{\partial \mathcal{X}}$, which is dependent on the constants $r_\mathcal{X}$ and t_c. By combining inequalities (A.8) and (A.9), with inequality (A.7), we get

$$\|\mathcal{C}[\mathcal{X}_1](t) - \mathcal{C}[\mathcal{X}_2](t)\|_{\mathbb{W}_t^{1,1}} \leq t_c \rho_\mathcal{X} \|\mathcal{X}_1(t) - \mathcal{X}_2(t)\|_{\mathbb{W}_t^{1,1}} \quad \text{(A.10)}$$

where $\rho_\mathcal{X} = L_{x_1} + L_{h_1} L_{h_2} b_\rho$. Therefore, by taking $t_c \leq \frac{\rho_c}{\rho_\mathcal{X}}$, for any $0 \leq \rho_c \leq 1$, we have

$$\|\mathcal{C}[\mathcal{X}_1](t) - \mathcal{C}[\mathcal{X}_2](t)\|_{\mathbb{W}_t^{1,1}} \leq \rho_c \|\mathcal{X}_1(t) - \mathcal{X}_2(t)\|_{\mathbb{W}_t^{1,1}}$$

which implies that $\mathcal{C}[\mathcal{X}](t)$ is a contraction mapping over the set $\mathcal{S}$. Combining all the previous analysis, and by using the contraction mapping Theorem (B.1) of [81], we conclude that if

$$t_c \leq \min\{t_u, \frac{r_\mathcal{X}}{b_q}, \frac{\rho_c}{\rho_\mathcal{X}}\}$$

then there is a unique solution $\mathcal{X}(t) \in \mathcal{S}$ that satisfies (A.1), for all $t \leq t_c$. With that, we have established the uniqueness of the solution of (A.1) in the set $\mathcal{S}$. We need to show the uniqueness of the solution in $\mathbb{W}_t^{1,1}$. We can prove that by showing that for any $\mathcal{X}_o \in \Omega_\mathcal{X}$, the solution cannot

leave the set $\Omega_\mathcal{X}$. To see this, let the time t_p be such that the solution $\mathcal{X}(t_p)$ leaves the boundary of the set $\Omega_\mathcal{X}$. By following similar steps that led to (A.6), we get

$$r_\mathcal{X} = \|\mathcal{X}(t_p) - \mathcal{X}_o\|_1 \leq t_p b_q \Rightarrow t_p \geq \frac{r_\mathcal{X}}{b_q} \Rightarrow t_p \geq t_c$$

which means that $\mathcal{X}(t)$ cannot leave the set $\Omega_\mathcal{X}$ for all time $t \leq t_c$, and this implies that any solution $\mathcal{X}(t) \in \mathbb{W}_t^{1,1}$ lies in $\mathcal{S}$, from which the uniqueness of the solution is established in the space $\mathbb{W}_t^{1,1}$. ∎

A.2 Proof of Theorem 3.1

The proof is done in three steps.

Step 1: By using the appropriate Lyapunov functions of the last 5 variables of the closed-loop system (3.42), we show that there exist $\rho_\varphi > 0$, $\tau_1^* > 0$, $\mu_1^*(\tau) > 0$, and $\varepsilon_1^*(\tau, \mu) > 0$ such that for each $\tau \in (0, \tau_1^*]$, $\mu \in (0, \mu_1^*]$, and $\varepsilon \in (0, \varepsilon_1^*]$, the compact set $\Upsilon_{r,c,\varepsilon} = \Sigma_r \times \Omega_c \times \Psi_\varepsilon$ is positively-invariant. This is done by showing that the time-derivatives of the Lyapunov functions are negative on the boundaries of this set.

To achieve this step, first by using the following inequality

$$\dot{V}_\eta \leq -\|\eta\|^2 + 2\mu \|\eta\| \|P_\eta B_\eta\|$$

it can be shown that for the set Ω_η with $\rho_\eta = 4\|P_\eta B_\eta\|^2 \lambda_{max}(P_\eta)$, $\dot{V}_\eta \leq 0$ on the boundary $V_\eta = \rho_\eta \mu^2$. Inside Ω_η, we have $\|\eta\| \leq \mu \bar{\rho}_\eta$, where $\bar{\rho}_\eta = \sqrt{\rho_\eta / \lambda_{min}(P_\eta)}$. Because of the parameter projection, we have $\|\hat{K}_\eta\| \leq b_{max} = \max_{\eta \in \Omega_\eta}(b_i + \delta), 1 \leq i \leq \iota$. Therefore, inside the set

124

$\Omega_\eta \times \{|s| \leq c\}$, we have the inequality

$$\dot{V}_\zeta \leq -\|\zeta\|^2 + 2\|\zeta\|\|P_\zeta B_\zeta\| \left(c + \mu \bar{\rho}_\eta . b_{max}\right)$$

if $\mu \leq c/\left(\bar{\rho}_\eta . b_{max}\right)$, then we have

$$\dot{V}_\zeta \leq -\|\zeta\|^2 + 4\|\zeta\|\|P_\zeta B_\zeta\|c$$

Let $\Omega_\zeta = \{V_\zeta \leq \rho_\zeta c^2\}$, where $\left(\rho_\zeta = 16\|P_\zeta B_\zeta\|^2 \lambda_{max}\left(P_\zeta\right)\right)$. The above inequality shows that $\dot{V}_\zeta \leq 0$ on the boundary $V_\zeta = \rho_\zeta c^2$. Inside the set $\Omega_\eta \times \Omega_\zeta \times \{|s| \leq c\}$, we have $\|\zeta\| \leq c\bar{\rho}_\zeta$, where $\bar{\rho}_\zeta = \sqrt{\rho_\zeta/\lambda_{min}\left(P_\zeta\right)}$. Hence, by using

$$e = \bar{K}_\zeta \zeta + B_\varphi \left(s - \hat{K}_\eta \eta\right)$$

where

$$\bar{K}_\zeta = \begin{bmatrix} I \\ -K_\zeta \end{bmatrix}, \quad K_\zeta = \begin{bmatrix} k_1 & k_2 & \dots & k_{n-1} \end{bmatrix}$$

it can be verified, if $\mu \leq c/\left(\bar{\rho}_\eta . b_{max}\right)$, then $\|e\| \leq \rho_e c$, where $\rho_e = \left(\bar{\rho}_\zeta + 2\right)$. The time-derivative of the Lyapunov function V_φ is given by

$$\varepsilon \dot{V}_\varphi = -\varphi^T \varphi + 2\varepsilon \varphi^T P_\varphi B_\varphi \left[-b_d \tilde{z}_h - \Delta_e + (e)\Delta_2\right.$$

$$\left. - b_h . \psi\left(\eta, \hat{e}, z_h, \mu\right) + \psi_z\left(\cdot\right)\right]$$

The function $\psi\left(\eta, \hat{e}, z_h, \mu\right)$ is globally bounded in $\hat{\zeta}$ for all $\left(\eta, \zeta, s, \tilde{z}_h\right) \in \Omega_\eta \times \Omega_\zeta \times \{|s| \leq c\} \times \Sigma_r$. Then there exists a positive constant l_φ such that $|-b_d \tilde{z}_h - \Delta_e + (e)\Delta_2 - b_h . \psi\left(\eta, \hat{e}, z_h, \mu\right) +$

$\psi_z(\cdot)| \le l_\varphi$. Therefore, the time-derivative of V_φ satisfies the following inequality

$$\varepsilon \dot{V}_\varphi \le -\|\varphi\|^2 + 2\varepsilon \|P_\varphi B_\varphi\| l_\varphi . \|\varphi\| \le -\frac{1}{2}\|\varphi\|^2 \tag{A.11}$$

$\forall \|\varphi\| \ge 4\varepsilon \|P_\varphi B_\varphi\| l_\varphi$. It follows that the above inequality is satisfied for all $V_\varphi \ge \rho_\varphi \varepsilon^2$, and $\dot{V}_\varphi \le 0$

on the boundary $V_\varphi = \rho_\varphi \varepsilon^2$, where $\rho_\varphi = 16 \left(\|P_\varphi B_\varphi\| l_\varphi\right)^2 \lambda_{max}(P_\varphi)$.

Consider the filter dynamics equation. Inside the set $\{\Omega_\eta \times \Omega_\zeta \times \{|s| \le c\} \times \Sigma_r \times \Psi_\varepsilon\}$, the term

$\Delta_q(\cdot)$ will be bounded due to boundedness of the state variables in the domain of interest. There-

fore, we have

$$|\dot{u}_{eq}| \le k_{eq} \quad \text{and} \quad |\frac{\partial Q_{h-o}}{\partial u}| \le k_q$$

where k_{eq} and k_q are positive constants, independent of τ. Moreover, it can be established that

$$|\dot{\beta}_s(t, \hat{e}, z_h)| \le \frac{K_o}{\Theta_d^N \theta_{ho}^N (1 - \bar{K}_o)}$$

In addition, due to the Lipschitz properties of the term ψ_q in its arguments and since $\|\varphi\| \le \bar{\rho}_\varphi \varepsilon$

(where $\bar{\rho}_\varphi = \sqrt{\rho_\varphi / \lambda_{min}(P_\varphi)}$), one has

$$|\psi_q| \le l_q \|\zeta - \hat{\zeta}\| \le l_q \|\varphi\| \le l_q \bar{\rho}_\varphi \varepsilon \tag{A.12}$$

for some positive constant l_q independent of τ. Therefore, if $\varepsilon \le \frac{k_z}{l_q \bar{\rho}_\varphi}$, where

$$k_z = k_q k_{eq} \left(1 + \frac{K_o}{\Theta_d^N \theta_{ho}^N (1 - \bar{K}_o)}\right)$$

then, the time-derivative of V_q satisfies the following inequality;

$$\tau \dot{V}_q \leq -|\tilde{z}_h|^2 + \tau \left(k_z + l_q \bar{\rho}_\varphi \varepsilon\right)|\tilde{z}_h| \leq -\frac{1}{2}|\tilde{z}_h|^2 \tag{A.13}$$

for all $|\tilde{z}_h| \geq 4\tau k_z$. This implies that the $\dot{V}_q$ is negative on the boundary of the set Σ_τ, where $\rho_q = 4k_z^2$. Consider now the surface dynamics $\dot{s}$. Obtain the time-derivative of the V_s and add and subtract the terms $b_h.\psi(\eta, e, z_h, \mu)$ and $(\beta_s(t, \hat{e}, z_h).\text{sat}(s/\mu))$ inside the brackets. Then it can be shown, by utilizing the Lipschitz properties of the these terms, that if ε is small enough, we have

$$|\psi(\eta, e, z_h, \mu) - \psi(\eta, \hat{e}, z_h, \mu)| \leq \left(l_\beta + l_s/\mu\right)\|\zeta - \hat{\zeta}\| \leq \left(l_\beta + l_s/\mu\right)\|\varphi\| \tag{A.14}$$

Similar to inequality (A.12), we can show that

$$|\psi_z| \leq l_z\|\zeta - \hat{\zeta}\| \leq l_z\|\varphi\| \leq l_z\bar{\rho}_\varphi \varepsilon$$

where l_z is a positive constant and independent of τ and ε. Inside the set $\{\Omega_\eta \times \Omega_\zeta \times \Psi_\tau \times \Psi_\varepsilon\}$, consider the term $\Delta_1(\cdot)$. Since $\|\eta\| \leq \mu\bar{\rho}_\eta$ and because of the parameter projection used in the adaptation law, we can conclude that $\|\dot{\hat{\lambda}}_\eta\| \leq \beta_{smax}$ and $\|v\| \leq \mu\bar{\rho}_\eta$, where $\beta_{smax} = \max_{\{t \geq 0\}}(|\beta_s(t, \hat{e}, z_h)|)$. Consequently, we can show $|\Delta_1(\cdot)| \leq \mu\rho_\Delta$, where $\rho_\Delta = \bar{\rho}_\eta(b_{max} + \beta_{smax}) + b_{max} + \|B_\eta\|$. By using $\|\varphi\| \leq \bar{\rho}_\varphi \varepsilon$, and inequalities (A.12), (A.14), utilizing the inequality $|\Delta_1(\cdot)| \leq \mu\rho_\Delta$, and the switching gain function (3.43), the time derivative of the surface s will satisfy the following inequality

$$\dot{V}_s \leq b.|s|\left(-\bar{\gamma}_o + \frac{\tau k_{zz}}{b} + \frac{\mu\rho_\Delta}{b}\right.$$
$$\left.+ \varepsilon.\left(\Theta_d^N.\theta_{h_0}^N\left(l_\beta + l_s/\mu\right)\bar{\rho}_\varphi + l_z\bar{\rho}_\varphi/b\right)\right)$$

127

where $\bar{\gamma}_o = \gamma_o \Theta_d^N \theta_{h_0}^N (1 - \bar{K}_o)$. If

$$\tau \leq \frac{\bar{\gamma}_o.b}{3k_{zz}}, \quad \mu \leq \frac{\bar{\gamma}_o.b}{3.\rho_\Delta}$$

and

$$\varepsilon \leq \frac{\bar{\gamma}_o.b}{3.\left(\Theta_d^N.\theta_{h_0}^N \left(l_\beta + l_s/\mu\right)\bar{\rho}_\varphi + l_z\bar{\rho}_\varphi/b\right)}$$

we can show $\dot{V}_s \leq -b.\bar{\gamma}_o.|s|$, which proves that $\dot{V}_s \leq 0$ on the boundary $|s| = c$. The above analysis shows that the set $\Upsilon_{r,c,\varepsilon}$ is positively-invariant and by choosing c and r large enough, we can include any compact set of (ζ, s) in the interior of $\Upsilon_{r,c,\varepsilon}$. This completes the proof of the first step.

Step 2: Let a, b, r_1, and r_2 be positive constants such that $a < b < c$ and $r_1 < r_2 < r$. Show that for any bounded $\hat{e}(0)$ and for any $(\eta(0), \zeta(0), s(0)) \in \Omega_a$ and $\tilde{z}_h(0,0,0) \in \Sigma_{r_1}$, where Ω_a and Σ_{r_1} are compact sets in the interior of the compact sets Ω_b and Σ_{r_2}, respectively, and there exists $\varepsilon_2^*(\tau, \mu) > 0$ such that for every $\varepsilon \in (0, \varepsilon_2^*]$ the trajectory enters the set Υ_{b,r_2} in finite time. Then show that for any $(\eta(0), \zeta(0), s(0)) \in \Omega_b$ and $\tilde{z}_h(0,0,0) \in \Sigma_{r_2}$, there exists $\tau_2^* > 0$ such that for every $\tau_2 \in (0, \tau_2^*]$ and for every $\varepsilon \in (0, \varepsilon_2^*]$ the trajectory enters the set $\Upsilon_{c,r}$ in finite time.

Since for $(\eta, \zeta, s) \in \Omega_\eta \times \Omega_b$ and $\tilde{z}_h \in \Sigma_{r_2}$, the term $\text{sat}\left(\left(\frac{s - N(\varepsilon)\varphi}{\mu}\right)\right)$ is globally-bounded uniformly in $\hat{\zeta}$, it follows that the right-hand side of the slow dynamics of the closed-loop system (3.42) is globally-bounded uniformly in ε. Consequently, there exists a time T_o, independent of ε, such that for all $(\eta, \zeta, s) \in \Omega_b$ and $\tilde{z}_h \in \Sigma_{r_2}$ for $0 \leq t \leq T_o$, using the inequality (A.11), we can show that

$$\dot{V}_\varphi \leq -\frac{1}{2\varepsilon\lambda_{max}(P_\varphi)}V_\varphi$$

The above inequality shows that for any bounded $\hat{e}(0)$, there exists a time $T_1(\varepsilon) < T_o$, where $\lim_{\varepsilon \to 0} T_1(\varepsilon) = 0$, during which φ enters Σ_ε in finite time. Therefore, choosing ε small enough to

make $(T_1(\varepsilon) < T_o)$ guarantees that the trajectories will enter Υ_{b,r_2} in finite time. Consider the shifted filter dynamics, due to the boundedness of the term Δ_q, then there exists a time $T_f > T_o$, independent of τ and ε, such that for all $(\eta, \zeta, s) \in \Omega_c$ and $\tilde{z}_h \in \Sigma_r$, for $0 \le t \le T_f$, we can show using inequality (A.13) that

$$\dot{V}_q \le -\frac{1}{\tau} V_q$$

Therefore, there exists a time $T_2(\tau) < T_f$, where $\lim_{\tau \to 0} T_2(\tau) = 0$. During the interval $(0, T_2]$, $\tilde{z}_h$ enters the set Σ_τ in finite time. Consequently, choosing τ small enough to make $(T_2(\tau) \le T_f)$ will ensure that all the trajectories enter to the set $\Upsilon_{c,r}$ in finite time. This completes the second step of the proof.

Step 3: Show that there exists $\varepsilon_3^*(\tau, \mu) > 0$, such that for all $\varepsilon \in (0, \varepsilon_3^*]$, such that for every trajectory in $\Upsilon_{r,c,\varepsilon}$ enters a small positively-invariant set $\Upsilon_{\tau,\mu,\varepsilon} = \Psi_\tau \times \Omega_\mu \times \Psi_\varepsilon$, which vanishes to the origin as τ, μ and ε tend to zero.

To prove this statement, similar arguments used to show that $\Upsilon_{r,c,\varepsilon}$ is positively-invariant can be repeated to show that any trajectories started inside $\Upsilon_{r,c,\varepsilon}$ will enter a positively-invariant set $\Upsilon_{\tau,\mu,\varepsilon}$ and stay therein for all the future time. With this step, the proof is concluded. $\square$

A.3   Proof of Theorem 3.2

Consider the following composite Lyapunov Function candidate;

$$V_a = \vartheta^T P_\eta \vartheta + \kappa_\zeta \zeta^T P_\zeta \zeta + \frac{1}{2.b_h} s_c^2 + \frac{1}{2} \tilde{z}_h^2 + \left(\frac{\mu}{2.\gamma}\right) \tilde{\lambda}^T \tilde{\lambda} \tag{A.15}$$

Consider each term of (A.15) separately. Due to the Lipschitz properties of the functions b_ϑ, b_{sc}, F_ϑ, F_{sc}, F_λ, ψ_z, and ψ_q and due to the boundedness of the terms Δ_ϑ, Δ_{sc}, Δ_q, and $\tilde{\chi}$ as indicated

in remark (3.1) above, the time-derivative of V_a satisfies the following inequality

$$\dot{V}_a \leq -X^T Q_a X + \frac{c_4}{\mu} \|\vartheta\|.\|\varphi\| + \left(c_{11} + \frac{c_{12}}{\mu}\right).|s_c|.\|\varphi\|$$

$$+ \frac{c_{13}}{\tau}|\tilde{z}_h|.\|\varphi\| - \frac{\beta_s\left(t, \hat{e}, z_h\right).s_c.\tilde{\lambda}_\eta^T v}{\mu} + \frac{\mu}{\gamma}\lambda_\eta^T \dot{\tilde{\lambda}}_\eta \qquad (A.16)$$

$$+ \delta_\vartheta.\|\vartheta\| + \delta_{sc}.|s_c| + \delta_z.|\tilde{z}_h|$$

where $\delta_\vartheta = 2 * \|P_\eta\|.\delta_{\vartheta_o}$, $\delta_{sc} = \frac{1}{b_h}.\delta_{sc_o}$, the matrix

$$Q_a = \begin{bmatrix} 1 & -c_1 & -c_2 & -(c_3 + c_8) \\ -c_1 & \kappa_\zeta & 0 & -\left(c_9 + \kappa_\zeta c_5\right) \\ -c_2 & 0 & \frac{1}{\tau} & -c_{10} \\ -(c_3 + c_8) & -\left(c_9 + \kappa_\zeta c_5\right) & -c_{10} & \left(\frac{c_6}{\mu} - c_7\right) \end{bmatrix}$$

and the composite vector $X = \begin{bmatrix} \|\vartheta\| & \|\zeta\| & \|\tilde{z}_h\| & |S_c| \end{bmatrix}^T$. The constants c_i, $1 \leq i \leq 13$ are positive and independent of τ and μ. In order to make the matrix Q_a positive definite, choose κ_ζ large enough to make the 2×2 principal minor positive, and then choose τ small enough to make the 3×3 principal minor positive, then choose μ small enough to make the determinant of the matrix Q_a positive. The detailed derivation of inequality (A.16) is presented in Appendix A.4. By applying the adaptation rule under output-feedback (the last equation of the closed-loop dynamics (3.46)), and considering the case when $\bar{v}$ is not fully persistently exciting, we use Lemma 3.1 along with the change of coordinates (3.44). Therefore, the inequality (A.16) can be rewritten as

$$\dot{V}_a \leq -\alpha_1 \|X\|^2 + \alpha_2 \|X\|.\|\varphi\| + \alpha_3 \|\tilde{\lambda}_{\eta a}\|.\|\varphi\|$$

$$+ \left(\delta_\vartheta + \delta_{sc} + \delta_z\right).\|X\|$$

where α_1, α_2, and α_3 are positive constants. α_2 is dependent on τ, μ, and $\|\tilde{\lambda}_{\eta_b}\|$, while α_3 is dependent on μ only, and $\tilde{\lambda}_{\eta_a}$ $\tilde{\lambda}_{\eta_b}$ are the adapted parameters corresponding to the excited and non-excited modes, respectively. Next, consider the subsystem formed of the $\dot{s}_c$ and $\dot{\tilde{\lambda}}_{\eta_a}$ equations, which is found to be

$$\begin{bmatrix} \dot{s}_c \\ \dot{\tilde{\lambda}}_{\eta_a} \end{bmatrix} = \begin{bmatrix} -\frac{b_h}{\mu}\beta_s\left(t,\hat{e},\tilde{z}_h\right) & -\frac{b_h}{\mu}\beta_s\left(t,\hat{e},\tilde{z}_h\right)\bar{v}_a^T \\ \gamma\frac{b_h}{\mu}\beta_s\left(t,\hat{e},\tilde{z}_h\right)\bar{v}_a^T & 0 \end{bmatrix} \begin{bmatrix} s_c \\ \tilde{\lambda}_{\eta_a} \end{bmatrix} \\ + \begin{bmatrix} g_1\left(\cdot\right) \\ g_2\left(\cdot\right) \end{bmatrix}$$

(A.17)

where

$$g_1\left(\cdot\right) = -b_h\beta_s\left(t,\hat{e},\tilde{z}_h\right)\tilde{\lambda}_{\eta_a}^T\left[\vartheta_a - B_{\eta_a}\varsigma\right]$$
$$- b_h\beta_s\left(t,\hat{e},\tilde{z}_h\right)\tilde{\lambda}_{\eta_b}^T\left[\vartheta_b - B_{\eta_b}\varsigma\right]$$
$$+ F_{sc}\left(\vartheta,\zeta,\tilde{z}_h,s_c\right) + b_{sc}\left(\varphi\right)/\mu + \Delta_{sc}\left(\bar{\eta},\zeta,z_h,\bar{\chi},\tilde{\chi},\mu\right)$$
$$+ \psi_z\left(\cdot\right)$$
$$g_2\left(\cdot\right) = -\gamma\frac{b_h}{\mu}\beta_s\left(t,\hat{e},\tilde{z}_h\right)\bar{v}_a^T.s_c + \beta_s\left(t,\hat{e},\tilde{z}_h\right)N_a.Hv\left[s_c\right.$$
$$\left. - N\left(\varepsilon\right)\varphi\right]/\mu^2$$

Notice here that $\|\tilde{\lambda}_{\eta_b}\|$ is treated as a bounded time-varying disturbance due to the smooth projection. Therefore, the functions $g_1\left(\cdot\right)$ and $g_2\left(\cdot\right)$ in (A.17) vanish at $\vartheta = 0$, $\zeta = 0$, $s_c = 0$, $\varphi = 0$, $\tilde{\lambda}_{\eta_a} = 0$, $\tilde{\chi} = 0$ regardless of the value of $\|\tilde{\lambda}_{\eta_b}\|$. Therefore, according to Section 13.4 of [93], the origin of the homogeneous part of (A.17) has an exponentially stable equilibrium point at $s_c = 0$, $\tilde{\lambda}_{\eta_a} = 0$. By using the converse Lyapunov function (Theorem 4.14 of [81]), there is a Lyapunov

function V_b whose time-derivative along the system (A.17) satisfies the following inequality

$$\dot{V}_b \leq -\alpha_4|s_c|^2 - \alpha_5\|\tilde{\lambda}_{\eta a}\|^2 + \alpha_6\|X\|^2 + \alpha_7\|X\|\|\varphi\|$$
$$+ \alpha_8\|X\|\|\tilde{\lambda}_{\eta a}\| + \alpha_9\|\tilde{\lambda}_{\eta a}\|\|\varphi\| + \alpha_{10}\delta_{sc}\|X\|$$

where the positive constants α_i, $4 \leq i \leq 10$, may depend on μ but are independent of ε. Consider now the estimation error dynamics ($\dot{\varphi}$ equation). It can be shown that the time-derivative of the Lyapunov function V_φ satisfies the following inequality;

$$\dot{V}_\varphi \leq -\frac{1}{\varepsilon}\|\varphi\|^2 + \alpha_{11}\|\varphi\|^2 + \alpha_{12}\|\tilde{\lambda}_{\eta a}\|\|\varphi\| + \alpha_{13}\|X\|\|\varphi\| + \alpha_{14}\delta_{sc}\|\varphi\|$$

where α_i, $11 \leq i \leq 14$, are positive constants and are independent of ε. Finally, consider the composite Lyapunov function candidate for the closed-loop system: $V_{cl} = \kappa V_a + V_b + V_\varphi$, where κ is a positive constant. It can be shown that the time-derivative of V_{cl} satisfies the following inequality;

$$\dot{V}_{cl} \leq -Y^T Q_{cl} Y + \delta_\chi \|Y\| \tag{A.18}$$

where $Y = \begin{bmatrix} \|X\| & \|\tilde{\lambda}_{\eta a}\| & \|\varphi\| \end{bmatrix}^T$ and the matrix

$$Q_{cl} = \begin{bmatrix} \kappa\alpha_1 - \alpha_{15} & -\alpha_8 & -(\kappa\alpha_2 + \alpha_{16}) \\ -\alpha_8 & \alpha_5 & -(\kappa\alpha_3 + \alpha_{17}) \\ -(\kappa\alpha_2 + \alpha_{16}) & -(\kappa\alpha_3 + \alpha_{17}) & \left(\frac{1}{\varepsilon} - \alpha_{11}\right) \end{bmatrix}$$

where $\alpha_{15} = \alpha_6 - \alpha_4$, $\alpha_{16} = \alpha_7 + \alpha_{13}$, and $\alpha_{17} = \alpha_9 + \alpha_{12}$. In order to make the matrix Q_{cl} positive definite, choose κ large enough to make the 2×2 principal minor positive, then choose ε small enough to make Q_{cl} positive definite. If the second term of inequality (A.18) vanishes, by

Theorem 8.4 of [81], we can show that $\lim\limits_{t\to\infty} \|Y\| = 0$. Accordingly, we can show that $\lim\limits_{t\to\infty} \|e\| = 0$.

Also under persistency of excitation condition and by Lemma 3.1 we have $\lim\limits_{t\to\infty} \tilde{\lambda}_\eta = \tilde{\lambda}_{\eta a} = 0$. If the second term does not vanish, the above inequality can be rewritten in the following way;

$$\dot{V}_{cl} \leq -\theta_1 V_{cl} + \delta_\chi \theta_2 \sqrt{V_{cl}}$$

for some positive constants θ_1 and θ_2. Let $W = \sqrt{V}$, then the above inequality will became

$$\dot{W} \leq -\theta_3 W + \theta_4 \delta_\chi$$

where θ_3 and θ_4 are positive constants. This inequality shows that the trajectory will converge exponentially to a positively invariant set, in which all the variables are ultimately bounded by a constant depends on μ in finite time, by which the proof is completed. $\qquad \square$

A.4 Derivation of Inequality (A.16)

To construct the quadratic form of inequality (A.16), we need to obtain the time-derivative of each term of the composite Lyapunov function (A.15). Consider the first term, let $V_\vartheta = \vartheta^T P_\eta \vartheta$, then the time-derivative of V_ϑ is

$$\begin{aligned}
\dot{V}_\vartheta = -\vartheta^T \vartheta + 2\vartheta^T P_\eta \cdot \Big[& F_\vartheta\left(\zeta, \tilde{z}_h, s_c\right) + b_\vartheta\left(\varphi\right)/\mu \\
& + \Delta_\vartheta\left(\bar{\eta}, \zeta, z_h, \bar{\chi}, \tilde{\chi}, \mu\right) \Big]
\end{aligned} \tag{A.19}$$

By looking inside the brackets, consider first the function $F(\cdot)$. By adding and subtracting appropriate terms and after rearranging we obtain

$$F_\vartheta(\zeta, \tilde{z}_h, s_c) = F_\vartheta(\zeta, \tilde{z}_h, s_c) - F_\vartheta(0, \tilde{z}_h, s_c)$$

$$+ F_\vartheta(0, \tilde{z}_h, s_c) - F_\vartheta(0, 0, s_c)$$

$$+ F_\vartheta(0, 0, s_c) - F_\vartheta(0, 0, 0)$$

$$+ F_\vartheta(0, 0, 0)$$

Based on the local Lipschitz properties of the function F_ϑ, the following inequality yields

$$|F_\vartheta(\zeta, \tilde{z}_h, s_c)| \leq l_{f_1} \|\zeta\| + l_{f_2} |\tilde{z}_h| + l_{f_3} |s_c|$$

where l_{f_1}, l_{f_2}, and l_{f_3} are positive constants. The other functions b_ϑ, b_{sc}, F_{sc}, and F_λ will be treated similarly to obtain their bounds. For the second term inside the bracket, we can show that

$$|b_\vartheta(\varphi)/\mu| \leq \frac{l_{f_4}}{\mu} \|\varphi\|$$

Based on inequalities (3.47-3.48) in remark (3.1) and from equation (A.19), we can show that

$$\dot{V}_\vartheta \leq -\|\vartheta\|^2 + c_1 \|\vartheta\| . \|\zeta\| + c_2 \|\vartheta\| . |\tilde{z}_h| + c_3 \|\vartheta\| . |s_c| + \frac{c_4}{\mu} \|\vartheta\| . \|\varphi\| + \delta_\vartheta \|\vartheta\| \qquad \text{(A.20)}$$

where $c_1 = 2l_{f_1} . \|P_\eta\|$, $c_2 = 2l_{f_2} . \|P_\eta\|$, $c_3 = 2l_{f_3} . \|P_\eta\|$, $c_4 = 2l_{f_4} . \|P_\eta\|$, and $\delta_\vartheta = 2\delta_{\vartheta_o} . \|P_\eta\|$. Consider the second term of (A.15). Let $V_{\zeta\zeta} = \kappa_\zeta \zeta^T P_\zeta \zeta$, then its time-derivative is

$$\dot{V}_{\zeta\zeta} = \kappa_\zeta \left[-\zeta^T \zeta + 2\zeta^T . P_\zeta B_\zeta s_c \right]$$

It can be easily seen that $\dot{V}_{\zeta\zeta}$ satisfies

$$|\dot{V}_{\zeta\zeta}| \leq -\kappa_\zeta \|\zeta\|^2 + \kappa_\zeta c_5 \|\zeta\|.|s_c| \tag{A.21}$$

where $c_5 = 2\|P_\zeta B_\zeta\|$. Now, consider the third term of (A.15) and let $V_{sc} = \frac{1}{2.b_h} s_c^2$. Then taking the time-derivative will result in

$$\begin{aligned}
\dot{V}_{sc} = &-\beta_s(t, \hat{e}, z_h) s_c^2/\mu - \beta_s(t, \hat{e}, z_h).s_c \tilde{\lambda}_\eta^T v/\mu \\
&+ F_{sc}(\vartheta, \zeta, \tilde{z}_h, s_c).s_c/b_h + b_{sc}(\varphi).s_c/(\mu b_h) \\
&+ \Delta_{sc}(\bar{\eta}, \zeta, z_h, \bar{\chi}, \tilde{\chi}, \mu).s_c/b_h + \psi_z(\cdot).s_c/b_h
\end{aligned} \tag{A.22}$$

Since the functions F_{sc} and b_{sc} are locally Lipschitz, we can derive the following two inequalities accordingly;

$$|F_{sc}(\vartheta, \zeta, \tilde{z}_h, s_c)/b_h| \leq l_{s_1}\|\vartheta\| + l_{s_2}\|\zeta\| + l_{s_3}|\tilde{z}_h| + l_{s_4}|s_c||b_{sc}(\varphi)/(\mu b_h)| \leq \frac{l_{s_5}}{\mu} \tag{A.23}$$

where $l_{s_i}, 1 \leq i \leq 5$ are positive constants. By using the inequalities provided in remark (3.1), and inequality (A.23), we can show that the time-derivative of V_s (A.22) satisfies the following inequality

$$\begin{aligned}
\dot{V}_{sc} \leq &-\left(\frac{c_6}{\mu} - c_7\right).|s_c|^2 + c_8|s_c|.\|\vartheta\| + c_9|s_c|.\|\zeta\| + c_{10}|s_c|.|\tilde{z}_h| + \left(c_{11} + \frac{c_{12}}{\mu}\right)|s_c|.\|\varphi\| \\
&+ \delta_{sc}|s_c| - \frac{\beta_s(t, \hat{e}, \tilde{z}_h) s_c.\tilde{\lambda}_\eta^T v}{\mu}
\end{aligned}$$

$$\tag{A.24}$$

where $c_6 = \bar{\beta}_{smax}$, $c_7 = l_{s_4}$, $c_8 = l_{s_1}$, $c_9 = l_{s_2}$, $c_{10} = l_{s_3}$, $c_{11} = \bar{l}_z$, $c_{12} = l_{s_5}$, and $\delta_{sc} = \frac{1}{b_h} . \delta_{sco}$.

Finally, consider the forth term of (A.15), and let $V_{zz} = \frac{1}{2}\tilde{z}_h^2$. Then the time-derivative of V_{zz} is

$$\dot{V}_{zz} = -\frac{\tilde{z}_h^2}{\tau} - \Delta_q(\cdot)\tilde{z}_h + \frac{\psi_q(\cdot)\tilde{z}_h}{\tau}$$

By utilizing the inequalities provided in remark (3.1), we can obtain

$$\dot{V}_{zz} \leq -\frac{1}{\tau}|z_h|^2 + \frac{c_{13}}{\tau}|\tilde{z}_h| . \|\varphi\| + \delta_z|\tilde{z}_h| \tag{A.25}$$

where $c_{13} = \bar{l}_q$. By combining the inequalities (A.20), (A.21), (A.24), and (A.25) and obtaining the derivative of the fifth term of the equation (A.15) with respect to time, we can derive inequality (A.16).

BIBLIOGRAPHY

BIBLIOGRAPHY

[1] G. Song, Jinqiang Zhao, Xiaoqin Zhou, and J. A. De Abreu-Garcia, "Tracking control of a piezoceramic actuator with hysteresis compensation using inverse preisach model," *IEEE/ASME Transactions on Mechatronics*, vol. 10, no. 2, pp. 198–209, 2005.

[2] M. Rakotondrabe, *Smart Materials-Based Actuators at The Micro/Nano-Scale: Characterization, Control and Applications*. NewYork: Springer-Verlag, 2013.

[3] J. Hou, L. Liu, Z. Wang, Z. Wang, N. Xi, Y. Wang, C. Wu, Z. Dong, and S. Yuan, "Afm-based robotic nano-hand for stable manipulation at nanoscale," *IEEE Transactions on Automation Science and Engineering*, vol. 10, no. 2, pp. 285–295, 2013.

[4] T. Tuma, A. Sebastian, J. Lygeros, and A. Pantazi, "The four pillars of nanopositioning for scanning probe microscopy: The position sensor, the scanning device, the feedback controller, and the reference trajectory," *IEEE Control Systems Magazine*, vol. 33, no. 6, pp. 68–85, 2013.

[5] A. Esbrook, X. Tan, and H. K. Khalil, "Control of systems with hysteresis via servocompensation and its application to nanopositioning," *IEEE Transactions on Control Systems Technology*, vol. 21, no. 3, pp. 725–738, May 2013.

[6] U. Bhagat, B. Shirinzadeh, Y. Tian, and D. Zhang, "Experimental analysis of laser interferometry-based robust motion tracking control of a flexure-based mechanism," *IEEE Transactions on Automation Science and Engineering*, vol. 10, no. 2, pp. 267–275, 2013.

[7] L.-J. Lai, G.-Y. Gu, and L.-M. Zhu, "Design and control of a decoupled two degree of freedom translational parallel micro-positioning stage," *Review of Scientific Instruments*, vol. 83, pp. 1 – 17, 2012.

[8] Y. Tian, D. Zhang, and B. Shirinzadeh, "Dynamic modelling of a flexure-based mechanism for ultra-precision grinding operation," *Precision Engineering*, vol. 35, no. 4, pp. 554 – 565, 2011.

[9] B. A. Gozen and O. B. Ozdoganlar, "Design and evaluation of a mechanical nanomanufacturing system for nanomilling," *Precision Engineering*, vol. 36, no. 1, pp. 19 – 30, 2012.

[10] L.-J. Lai, H. Zhou, Y.-J. Du, J. Zhang, J.-C. Jia, L.-M. Jiang, L.-M. Zhu, Z.-W. Tian, Z.-Q. Tian, and D.-P. Zhan, "High precision electrochemical micromachining based on confined etchant layer technique," *Electrochemistry Communications*, vol. 28, pp. 135 – 138, 2013.

[11] A. A. Tseng, "Advancements and challenges in development of atomic force microscopy for nanofabrication," *Nano Today*, vol. 6, no. 5, pp. 493 – 509, 2011.

[12] I. Casuso, J. Khao, M. Chami, P. Paul-Gilloteaux, M. Husain, J.-P. Duneau, H. Stahlberg, J. N. Sturgis, and S. Scheuring, "Characterization of the motion of membrane proteins using high-speed atomic force microscopy," *Nature Nanotechnology*, vol. 7, p. 525–529, 2012.

[13] D. J. Müller, M. Krieg, D. Alsteens, and Y. F. Dufrêne, "New frontiers in atomic force microscopy: analyzing interactions from single-molecules to cells," *Current Opinion in Biotechnology*, vol. 20, no. 1, pp. 4 – 13, 2009, analytical biotechnology.

[14] M. Brokate and J. Sprekels, *Hysteresis and Phase Transitions*. New York: Springer-Verlag, 1996.

[15] G. Tao and P. V. Kokotovic, "Adaptive control of plants with unknown hysteresis," *IEEE Transactions on Automatic Control*, vol. 40, no. 2, pp. 200–212, Feb 1995.

[16] J. Lee, M. Jin, N. Kashiri, D. G. Caldwell, and N. G. Tsagarakis, "Inversion-free force tracking control of piezoelectric actuators using fast finite-time integral terminal sliding-mode," *Mechatronics*, vol. 57, pp. 39 – 50, 2019.

[17] F. Ikhouane, V. Mañosa, and J. Rodellar, "Dynamic properties of the hysteretic Bouc-Wen model," *Systems Control Letters*, vol. 56, no. 3, pp. 197 – 205, 2007.

[18] R. Ouyang and B. Jayawardhana, "Absolute stability analysis of linear systems with duhem hysteresis operator," *Automatica*, vol. 50, no. 7, pp. 1860 – 1866, 2014.

[19] J. Oh and D. S. Bernstein, "Semilinear Duhem model for rate-independent and rate-dependent hysteresis," *IEEE Transactions on Automatic Control*, vol. 50, no. 5, pp. 631–645, 2005.

[20] Y. Liu, H. Liu, H. Wu, and D. Zou, "Modelling and compensation of hysteresis in piezoelectric actuators based on maxwell approach," *Electronics Letters*, vol. 52, no. 3, pp. 188–190, 2016.

[21] D. Lederer, H. Igarashi, A. Kost, and T. Honma, "On the parameter identification and application of the Jiles-Atherton hysteresis model for numerical modelling of measured characteristics," *IEEE Transactions on Magnetics*, vol. 35, no. 3, pp. 1211–1214, May 1999.

[22] M. A. Krasnosel'skii and A. V. Pokrovskii, *Systems with Hysteresis.* Springer Verlag, 1989.

[23] G. V. Webb, D. C. Lagoudas, and A. J. Kurdila, "Hysteresis modeling of sma actuators for control applications," *Journal of Intelligent Material Systems and Structures*, vol. 9, no. 6, pp. 432–448, 1998.

[24] A. Visintin, *Differential Models of Hysteresis.* Berlin: Springer, 1994.

[25] X. Tan and J. S. Baras, "Modeling and control of hysteresis in magnetostrictive actuators," *Automatica*, vol. 40, no. 9, pp. 1469–1480, 2004.

[26] M. Al Janaideh, S. Rakheja, and C.-Y. Su, "A generalized Prandtl–Ishlinskii model for characterizing the hysteresis and saturation nonlinearities of smart actuators," *Smart Materials and Structures*, vol. 18, no. 4, p. 045001, 2009.

[27] M. A. Janaideh, S. Rakheja, and C.-Y. Su, "A generalized Prandtl-Ishlinskii model for characterizing the hysteresis and saturation nonlinearities of smart actuators," *Smart Materials and Structures*, vol. 18, no. 4, pp. 1–9, 2009.

[28] I. D. Mayergoyz, *Mathematical Models of Hysteresis and Their Applications.* New York, NY: Elsevier, 2003.

[29] O. Aljanaideh, M. A. Janaideh, and M. Rakotondrabe, "Inversion-free feedforward dynamic compensation of hysteresis nonlinearities in piezoelectric micro/nano-positioning actuators," in *2015 IEEE International Conference on Robotics and Automation (ICRA)*, May 2015, pp. 2673–2678.

[30] M. Al Janaideh and P. Krejčí, "Inverse rate-dependent prandtl–ishlinskii model for feedforward compensation of hysteresis in a piezomicropositioning actuator," *IEEE/ASME Transactions on Mechatronics*, vol. 18, no. 5, pp. 1498–1507, Oct 2013.

[31] P. Krejci and K. Kuhnen, "Inverse control of systems with hysteresis and creep," *IEE Proceedings - Control Theory and Applications*, vol. 148, no. 3, pp. 185–192, 2001.

[32] K. Kuhnen, "Modeling, identification and compensation of complex hysteretic nonlinearities - a modified Prandtl-Ishlinskii approach," *European Journal of Control*, vol. 9, no. 4, pp. 407–418, 2003.

[33] M. A. Janaideh and P. Krejčí, "Prandtl–Ishlinskii hysteresis models for complex time dependent hysteresis nonlinearities," *Physica B: Condensed Matter*, vol. 407, no. 9, pp. 1365

– 1367, 2012, 8th International Symposium on Hysteresis Modeling and Micromagnetics (HMM 2011).

[34] M. A. Janaideh, S. Rakheja, J. Mao, and C. Su, "Inverse generalized asymmetric Prandtl-Ishlinskii model for compensation of hysteresis nonlinearities in smart actuators," in *2009 International Conference on Networking, Sensing and Control*, March 2009, pp. 834–839.

[35] Q. Xu and K. K. Tan, "Feedforward control based on inverse hysteresis models," in *Advanced Control of Piezoelectric Micro-/Nano-Positioning Systems*.   Springer, 2016, pp. 23–55.

[36] Z. Li, J. Shan, and U. Gabbert, "Inverse compensation of hysteresis using Krasnoselskii-Pokrovskii model," *IEEE/ASME Transactions on Mechatronics*, vol. 23, no. 2, pp. 966–971, April 2018.

[37] M. A. Janaideh, M. Rakotondrabe, I. Al-Darabsah, and O. Aljanaideh, "Internal model-based feedback control design for inversion-free feedforward rate-dependent hysteresis compensation of piezoelectric cantilever actuator," *Control Engineering Practice*, vol. 72, pp. 29 – 41, 2018.

[38] K. Kuhnen, "Modeling, identification and compensation of complex hysteretic nonlinearities: A modified Prandtl-Ishlinskii approach," *European Journal of Control*, vol. 9, no. 4, pp. 407 – 418, 2003.

[39] M. A. Janaideh, S. Rakheja, and C. Y. Su, "An analytical generalized Prandtl–Ishlinskii model inversion for hysteresis compensation in micropositioning control," *IEEE/ASME Transactions on Mechatronics*, vol. 16, no. 4, pp. 734–744, Aug 2011.

[40] Q. Wang and C.-Y. Su, "Robust adaptive control of a class of nonlinear systems including actuator hysteresis with Prandtl-Ishlinskii presentations," *Automatica*, vol. 42, no. 5, pp. 859 – 867, 2006.

[41] M. Edardar, X. Tan, and H. K. Khalil, "Tracking error analysis for feedback systems with hysteresis inversion and fast linear dynamics," *Journal of Dynamic Systems, Measurement, and Control*, vol. 136, no. 4, pp. 041 010–1–041 010–12, July 2014.

[42] G. Schitter, A. Stemmer, and F. Allgower, "Robust 2 dof-control of a piezoelectric tube scanner for high speed atomic force microscopy," in *American Control Conference, 2003. Proceedings of the 2003*, vol. 5, June 2003, pp. 3720–3725 vol.5.

[43] S. Bashash and N. Jalili, "Robust adaptive control of coupled parallel piezo-flexural nanopositioning stages," *IEEE/ASME Transactions on mechatronics*, vol. 14, no. 1, pp. 11–20, 2009.

[44] C. Li and Y. Tan, "Adaptive output feedback control of systems preceded by the Preisach-type hysteresis," *IEEE Transactions on Systems, Man, and Cybernetics*, vol. 35, pp. 130–135, 2005.

[45] X. Tan and H. K. Khalil, "Two-time-scale averaging of systems involving operators and its application to adaptive control of hysteretic systems," in *2009 American Control Conference*, June 2009, pp. 4476–4481.

[46] S. Liu, C. Su, and Z. Li, "Robust adaptive inverse control of a class of nonlinear systems with Prandtl-Ishlinskii hysteresis model," *IEEE Transactions on Automatic Control*, vol. 59, no. 8, pp. 2170–2175, Aug 2014.

[47] L. Ryba, J. Dokoupil, A. Voda, and G. Besançon, "Adaptive hysteresis compensation on an experimental nanopositioning platform," *International Journal of Control*, vol. 90, no. 4, pp. 765–778, 2017.

[48] M. Edardar, X. Tan, and H. K. Khalil, "Design and analysis of sliding mode controller under approximate hysteresis compensation," *IEEE Transactions on Control Systems Technology*, vol. 23, no. 2, pp. 598–608, March 2015.

[49] Y. Cao and X. B. Chen, "Integrated inversion-feedforward and pid-based-sliding-mode-control for piezoelectric actuators," in *2012 American Control Conference (ACC)*, 2012, pp. 869–874.

[50] J. A. McMahan and R. C. Smith, "Sliding mode control based on an inverse compensator design for hysteretic smart systems," in *2012 IEEE 51st IEEE Conference on Decision and Control (CDC)*, 2012, pp. 985–990.

[51] M. Al Janaideh, M. Rakotondrabe, and O. Aljanaideh, "Further results on hysteresis compensation of smart micropositioning systems with the inverse prandtl–ishlinskii compensator," *IEEE Transactions on Control Systems Technology*, vol. 24, no. 2, pp. 428–439, 2016.

[52] A. Isidori and C. I. Byrnes, "Output regulation of nonlinear systems," *IEEE Transactions on Automatic Control*, vol. 35, no. 2, pp. 131–140, Feb 1990.

[53] A. Serrani, A. Isidori, and L. Marconi, "Semi-global nonlinear output regulation with adaptive internal model," *IEEE Transactions on Automatic Control*, vol. 46, no. 8, pp. 1178–1194, Aug 2001.

[54] A. Esbrook, X. Tan, and H. K. Khalil, "A robust adaptive servocompensator for nanopositioning control," in *49th IEEE Conference on Decision and Control (CDC)*, Dec 2010, pp. 3688–3693.

[55] ——, "An indirect adaptive servocompensator for signals of unknown frequencies with application to nanopositioning," *Automatica*, vol. 49, no. 7, pp. 2006 – 2016, 2013. [Online]. Available: http://www.sciencedirect.com/science/article/pii/S0005109813001854

[56] Y. Yan, H. Wang, and Q. Zou, "A decoupled inversion-based iterative control approach to multi-axis precision positioning: 3d nanopositioning example," *Automatica*, vol. 48, no. 1, pp. 167 – 176, 2012.

[57] Z. Wang and Q. Zou, "A modeling-free differential-inversion-based iterative control approach to simultaneous hysteresis-dynamics compensation: High-speed large-range motion tracking example," in *2015 American Control Conference (ACC)*, 2015, pp. 3558–3563.

[58] H. Ghafarirad, S. M. Rezaei, A. Abdullah, M. Zareinejad, and M. Saadat, "Observer-based sliding mode control with adaptive perturbation estimation for micropositioning actuators," *Precision Engineering*, vol. 35, no. 2, pp. 271 – 281, 2011.

[59] Z. Qiao, M. Gan, and C. Wang, "Sliding mode control using linear extended state observer(leso) and hysteresis compensator based on bouc-wen model in sinusoidal position control of a piezoelectric actuator," in *Proceedings of the 33rd Chinese Control Conference*, 2014, pp. 3840–3845.

[60] R. Xu and M. Zhou, "Integral sliding mode tracking control of piezoelectric positioning platform with compensating hysteresis-observer," in *2017 International Conference on Advanced Mechatronic Systems (ICAMechS)*, 2017, pp. 472–476.

[61] R. Xu, X. Zhang, H. Guo, and M. Zhou, "Sliding mode tracking control with perturbation estimation for hysteresis nonlinearity of piezo-actuated stages," *IEEE Access*, vol. 6, pp. 30 617–30 629, 2018.

[62] X. Chen, T. Hisayama, and C. Su, "Adaptive control for uncertain continuous-time systems using implicit inversion of prandtl-ishlinskii hysteresis representation," *IEEE Transactions on Automatic Control*, vol. 55, no. 10, pp. 2357–2363, 2010.

[63] M. A. Janaideh and D. S. Bernstein, "Inversion-free adaptive control of uncertain systems with shape-memory-alloy actuation," in *2013 American Control Conference*, June 2013, pp. 3579–3584.

[64] A. Esbrook, X. Tan, and H. K. Khalil, "Inversion-free stabilization and regulation of systems with hysteresis via integral action," *Automatica*, vol. 50, no. 4, pp. 1017 – 1025, 2014.

[65] J. Chen, B. Ren, and Q. C. Zhong, "Hysteresis compensation in piezoelectric actuator positioning control based on the uncertainty and disturbance estimator," in *2015 American Control Conference (ACC)*, July 2015, pp. 2537–2542.

[66] J. Yi, S. Chang, and Y. Shen, "Disturbance-observer-based hysteresis compensation for piezoelectric actuators," *IEEE/ASME Transactions on Mechatronics*, vol. 14, no. 4, pp. 456–464, 2009.

[67] F. J. Goforth and Z. Gao, "An active disturbance rejection control solution for hysteresis compensation," in *2008 American Control Conference*. IEEE, 2008, pp. 2202–2208.

[68] M. Brokate and A. Pokrovskiı, "Asymptotically stable oscillations in systems with hysteresis nonlinearities," *Journal of Differential Equations*, vol. 150, no. 1, pp. 98 – 123, 1998.

[69] D. Chowdhury, Y. K. Al-Nadawi, and X. Tan, "Dynamic inversion-based hysteresis compensation using extended high-gain observer," *Under Review in Automatica*, forthcoming.

[70] R. Li and H. K. Khalil, "Nonlinear output regulation with adaptive conditional servocompensator," *Automatica*, vol. 48, no. 10, pp. 2550–2559, 2012.

[71] N. Hovakimyan, E. Lavretsky, and A. Sasane, "Dynamic inversion for nonaffine-in-control systems via time-scale separation. Part I," *Journal of Dynamical and Control Systems*, vol. 13, no. 4, pp. 451–465, 2007.

[72] L. B. Freidovich and H. K. Khalil, "Performance recovery of feedback-linearization-based designs," *IEEE Transactions on Automatic Control*, vol. 53, no. 10, pp. 2324–2334, 2008.

[73] J. Lee, R. Mukherjee, and H. K. Khalil, "Output feedback performance recovery in the presence of uncertainties," *Systems & Control Letters*, vol. 90, pp. 31–37, 2016.

[74] X. Chen, T. Hisayama, and C.-Y. Su, "Adaptive control for uncertain continuous-time systems using implicit inversion of Prandtl-Ishlinskii hysteresis representation," *IEEE Transactions on Automatic Control*, vol. 55, no. 10, pp. 2357–2363, 2010.

[75] "Pseudo-inverse-based adaptive control for uncertain discrete time systems preceded by hysteresis," *Automatica*, vol. 45, no. 2, pp. 469 – 476, 2009.

[76] M. A. Janaideh and A. M. Boker, "Modeling and output-feedback control of systems with netushil rate-dependent hysteresis nonlinearties," in *2018 IEEE Conference on Decision and Control (CDC)*, 2018, pp. 6912–6917.

[77] R. V. Iyer and X. Tan, "Control of hysteretic systems through inverse compensation," *IEEE Control Systems Magazine*, vol. 29, no. 1, pp. 83–99, 2009.

[78] M. A. Janaideh, S. Rakheja, and C.-Y. Su, "A generalized prandtl–ishlinskii model for characterizing the hysteresis and saturation nonlinearities of smart actuators," *Smart Materials and Structures*, vol. 18, no. 4, p. 045001, mar 2009. [Online]. Available: https://doi.org/10.1088%2F0964-1726%2F18%2F4%2F045001

[79] K. Kuhnen and H. Janocha, "Adaptive inverse control of piezoelectric actuators with hysteresis operators," in *1999 European Control Conference (ECC)*, 1999, pp. 791–796.

[80] P. Krejcí and K. Kuhnen, "Existence, uniqueness and l∞-stability of the Prandtl-Ishlinskii hysteresis and creep compensator," *Eur. J. Control*, vol. 14, no. 5, pp. 409–417, 2008.

[81] H. K. Khalil, *Nonlinear Systems*, 3rd ed.   Upper Saddle River, New Jersey: Prentice Hall, 2002.

[82] H. Khalil, *High-Gain Observers in Nonlinear Feedback Control*.   Philadelphia, PA: Society for Industrial and Applied Mathematics, 2017.

[83] F. Esfandiarie and H. K. Khalil, "Output feedback stabilization of fully linearizable systems," *International Journal of Control*, vol. 56, no. 5, pp. 1007–1037, 1992.

[84] V. Nikiforov, "Adaptive non-linear tracking with complete compensation of unknown disturbances," *European Journal of Control*, vol. 4, no. 2, pp. 132 – 139, 1998.

[85] Y. K. Al-Nadawi, X. Tan, and H. K. Khalil, "Inversion-free hysteresis compensation via adaptive conditional servomechanism with application to nanopositioning control," *IEEE Transactions on Control Systems Technology*, pp. 1–14, 2020.

[86] Y. K. Al-Nadawi, X. Tan, and H. K. Khalil, "An adaptive conditional servocompensator design for nanopositioning control," in *56th IEEE Annual Conference on Decision and Control, CDC 2017, Melbourne, Australia, December 12-15, 2017*, 2017, pp. 885–890.

[87] Y. Li and Z. Lin, *Stability and Performance of Control Systems with Actuator Saturation*. USA: Springer, 2018.

[88] C. Edwards and S. K. Spurgeon, *Sliding Mode Control Theory And Applications*, 1st ed. London, UK: Taylor & Francis, 1998.

[89] J. Cortes, "Discontinuous dynamical systems," *IEEE Control systems magazine*, vol. 28, no. 3, pp. 36–73, 2008.

[90] H. K. Khalil, "Cascade high-gain observers in output feedback control," *Automatica*, vol. 80, pp. 110–118, 2017. [Online]. Available: https://www.sciencedirect.com/science/article/pii/S000510981730105X

[91] D. Astolfi, L. Marconi, L. Praly, and A. R. Teel, "Low-power peaking-free high-gain observers," *Automatica*, vol. 98, pp. 169–179, 2018. [Online]. Available: https://www.sciencedirect.com/science/article/pii/S0005109818304345

[92] A. Isidori, L. Marconi, and L. Praly, "Robust design of nonlinear internal models without adaptation," *Automatica*, vol. 48, no. 10, pp. 2409–2419, 2012. [Online]. Available: https://www.sciencedirect.com/science/article/pii/S0005109812003421

[93] H. K. Khalil, *Nonlinear Systems*, 2nd ed.   Upper Saddle River, New Jersey: Prentice Hall, 1996.